INVESTIGATION OF ION CAPTURE IN AN ELECTRON BEAM ION TRAP CHARGE-BREEDER FOR RARE ISOTOPES

By

Kritsada Kittimanapun

A DISSERTATION

Submitted to
Michigan State University
in partial fulfillment of the requirements
for the degree of

Physics - Doctor of Philosophy

2014

ABSTRACT

INVESTIGATION OF ION CAPTURE IN AN ELECTRON BEAM ION TRAP CHARGE-BREEDER FOR RARE ISOTOPES

By

Kritsada Kittimanapun

Charge breeding of rare isotope ions has become an important ingredient for providing reaccelerated rare isotope beams for science. At the National Superconducting Cyclotron Laboratory (NSCL), a reaccelerator, ReA, has been built that employs an advanced Electron Beam Ion Trap (EBIT) as a charge breeder. ReA will provide rare-isotope beams with energies of a few hundred keV/u up to tens of MeV/u to enable the study of properties of rare isotopes via low energy Coulomb excitation and transfer reactions, and to investigate nuclear reactions important for nuclear astrophysics. ReA consists of an EBIT charge breeder, a charge-over-mass selector, a room temperature radio-frequency quadrupole accelerator, and a superconducting radio-frequency linear accelerator. The EBIT charge breeder features a high-current electron gun, a long trap structure, and a hybrid superconducting magnet to reach both high acceptance for injected low-charge ions as well as high-electron beam current densities for fast charge breeding.

In this work, continuous ion injection and capture in the EBIT have been investigated with a dedicated Monte-Carlo simulation code and in experimental studies. The Monte-Carlo code NEBIT considers the electron-impact ionization cross sections, space charge due to the electron beam current, ion dynamics, electric field from electrodes, and magnetic field from the superconducting magnet. Experiments were performed to study the capture efficiency as a function of injected ion beam current, electron beam current, trap size, and trap potential depth. The charge state evolution of trapped ions was studied, providing

information about the effective current density of the electron beam inside the EBIT. An attempt was made to measure the effective space-charge potential of the electron beam by studying the dynamics of a beam injected and reflected inside the trap.

For my family.

ACKNOWLEDGMENTS

First of all, I would like to thank my supervisor, Georg Bollen, who kindly accepted me as one of his student and pushed me hard. In addition, Stefan Schwarz primarily advised and taught me several things: technical laboratory work, computer programming, attitudes toward solving problems, etc. He was always available whenever I had questions. Discussion with Alain Lapierre was very useful. From his experience, he provided me valuable guidance which is important to my career. I would like to thank Oliver Kester for introducing me to the EBIT charge breeder and giving suggestions during the early stage of my research. Daniela Leitner also deserves recognition for her critical comments to my research and being one of the committee members. I would like to thank Norman Birge and Vladimir Zelevinsky for serving guidance committee members as well. Thank to Thomas Baumann, another EBIT group member, for useful suggestion and thesis proofreading.

Good friends are worth being mentioned. I would like to thank Adam Fritsch for proofreading this thesis and sharing many non-physics experiences. Big thank to Kiseok Chang for encouraging conversation and help once we were in the same research group. I would like to thank Thai community for a warm welcome since my first day in MSU and giving me a chance to be a president of the Thai Student Association. Running the organization is always a great experience.

Last but not least, I would like to thank my parents for supports on what I have been doing. My wife, Moui, is always beside and encourages me to overcome every problem I encountered. My daughters, Zoey and Sonia, are such beautiful ones who light me up and make me completely understand how great being a father. Without my lovely family members, I cannot imagine my life would be. Thank you.

TABLE OF CONTENTS

LIST OF TABLES

LIST OF FIGURES

Chapter 1

Introduction

The National Superconducting Cyclotron Laboratory (NSCL) has been successfully providing rare isotope beams produced by the projectile fragmentation method for nuclear science. Figure 1.1 shows a schematic of the NSCL facility. A high energy stable beam delivered by two coupled cyclotrons with an energy of > 80 MeV/u impinges on a production target. Rare isotopes are produced by fragmentation or in-flight fission. The reaction products are separated by the A1900 fragment separator and delivered to experimental areas.

These fast rare isotope beams have been used for a successful science program, including nuclear structure studies via intermediate energy Coulomb excitations, finding the limits of nuclear stability, or investigating the equation of state of nuclear matter. However, in order to increase scientific knowledge of rare isotopes, it is advantageous to offer those over a large energy range.

Rare isotope beams at very low energy, "stopped beams" enable precision experiments with traps and lasers. NSCL was the first facility to stop fast beams in a gas cell [1] and extract them as low-energy beams for enabling Penning trap mass measurements with the Low Energy Beam and Ion Trap (LEBIT) facility [2]. Laser spectroscopy has recently been added with the BEam COoler and LAser spectroscopy (BECOLA) station [3].

In addition to providing fast and stopped beams there is a variety of experiments that needs beams in the energy range from a couple of hundreds keV/u up to a few tens of

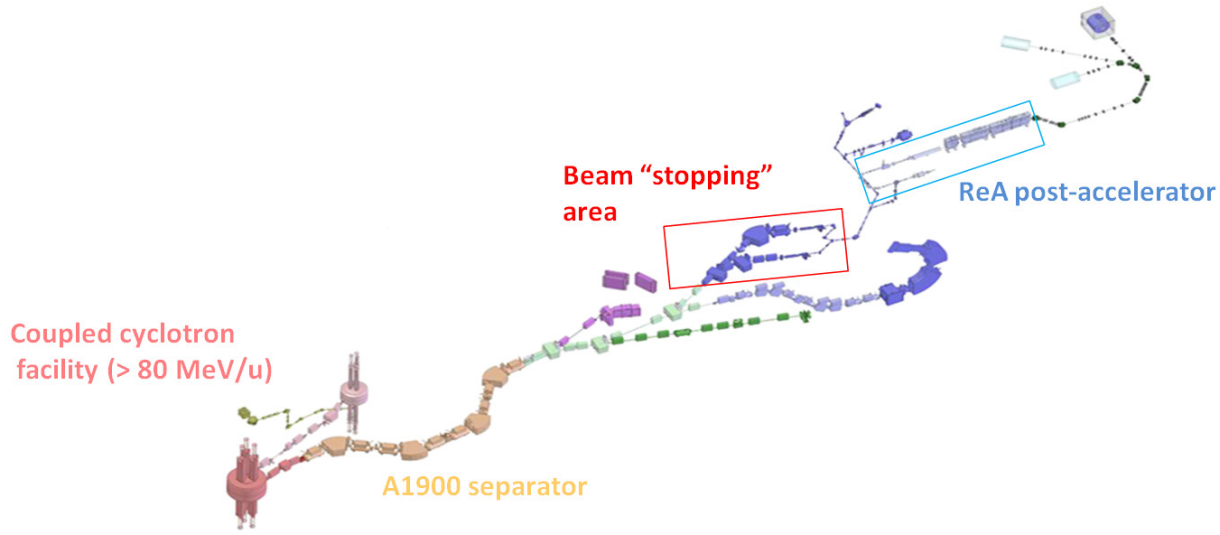

Figure 1.1 The NSCL Coupled Cyclotron Facility. High energy rare isotope beams produced in flight and separated by the A1900 separator are delivered to different experimental stations. Low-energy beams are produced by gas stopping and provided for "stopped beam" experiments or for reacceleration with ReA.

MeV/u for nuclear astrophysics and nuclear structure studies. With the realization of ReA, a reaccelerator of the available stopped beams, NSCL will be the first to provide rare isotope beams in this energy range that have been produced in-flight.

In order to make best use of the rare isotopes produced it is important that a reaccelerator scheme is chosen that provides high efficiency. The approach taken was to build a reaccelerator that combines an advanced Electron Beam Ion Trap (EBIT) as a charge breeder with a modern Superconducting Radio-Frequency (SRF) linac. The NSCL reaccelerator (ReA) is designed to achieve high efficiency for all elements available at the NSCL, for high beam rate capability and high beam quality, and for providing a variable time structure of the beam.

1.1 NSCL's Reaccelerator ReA

ReA benefits from using a scheme of reaccelerated highly charged ions (HCIs) instead of singly charged ions (SCIs) which makes the reaccelerator compact and reduces cost. The concept of ReA is shown in Figure 1.2.

Cooled SCIs from the gas stopper are selected by a mass separator and transported to a charge breeder. The EBIT-type charge breeder converts the rare isotope beam from a 1^+ to a Q^+ charge state. The EBIT floats on a high voltage platform so that the SCIs delivered from the gas stopper at an energy of up to 60 keV can be slowed down prior to be captured in the trap. Once charge-bred, the highly charged ions are extracted toward an achromatic charge-over-mass (Q/A) separator where the undesired background of HCIs from the EBIT is suppressed. The beam is then reaccelerated with a linear accelerator consisting of a Multi-Harmonic Buncher (MHB), a Radio Frequency Quadrupole (RFQ) accelerator and SRF cavities. The MHB in front of the RFQ is used for acceptance matching. The first cryomodule after the RFQ houses a rebuncher. The second and third cryomodules have cavities optimized for a beam with $\beta = v/c = 0.041$ and $\beta = 0.085$, respectively, where v is the ion velocity and c is the speed of light. The beam energy is expected to be 0.3 - 3 MeV/u for ^{238}U (q/m = 0.25) and 0.3 - 6 MeV/u for light elements (q/m = 0.5).

1.2 Highly charged ions for reacceleration of rare isotope beams

Different methods have been considered for providing higher charge states to ease the reacceleration of rare isotope beams: using a foil or gas target as a stripper, using an Electron Cyclotron Resonance (ECR) source as a charge breeder, or using an Electron

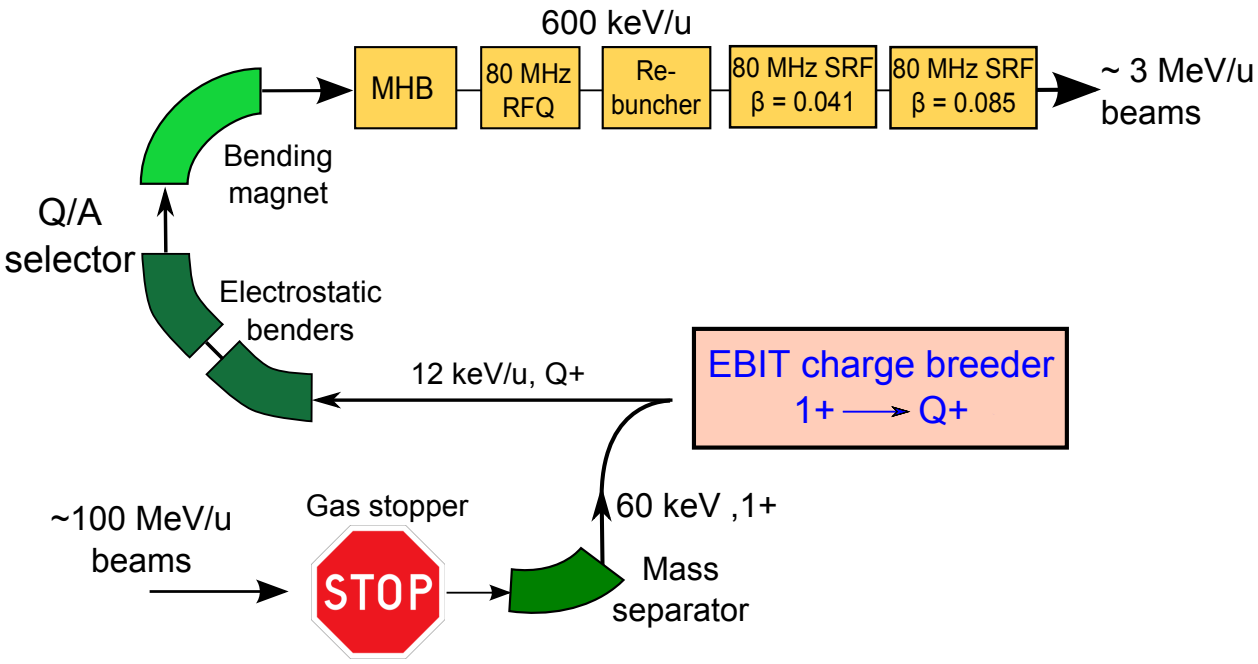

Figure 1.2 ReA concept. Fast ions are decelerated by a gas stopper and extracted as a very low-energy beam. This beam is transported to the EBIT for charge breeding, extracted with multiply higher charge states, separated by a Q/A selector, and accelerated through an RFQ and SRF cryomodules.

Beam Ion Source/Trap (EBIS/T) as a charge breeder.

The traditional stripping method is for example employed at ISAC at TRIUMF. Passing accelerated ions through a gas jet or a foil removes electrons and increases the ion's charge state. Such a scheme is costly because pre-acceleration of SCIs to energies of 100 keV/u is needed before passing through a gas jet or foils. In addition, the longitudinal and transverse emittance after stripping increases [4] and the stripping efficiency is not very high [5].

ECR Ion Sources (ECRIS) are used or were tested as possible charge state boosters at many facilities, for example, SPIRAL at GANIL [6], TRIUMF [7], ISOLDE [8], KEK-JAERI [9], and CARIBU at ANL [10]. ECRIS employs electron cyclotron resonance heating to transfer energy into the plasma electrons, that ionize gas into plasma confined by a strong magnetic field. The SCIs are continuously introduced into the hot plasma with high electron density.

The ECR-type PHOENIX source has demonstrated using the ECRIS method to charge breed Pb^{+} into Pb^{25+} with an efficiency of up to 7% [11]. A major disadvantage of operating ECRIS as a charge breeder is a very low beam purity. The working pressure is around $10^{-8} - 10^{-6}$ mbar and causes the extracted HCIs to contain a significant portion of residual gas.

The potential of EBIS/T as charge breeders has been recognized after the successful demonstration at REX-ISOLDE at CERN [12]. EBIS/T charge breeders are under development not only at NSCL [13], but also at ATLAS/ANL and planned for ISAC at TRIUMF.

The Electron Beam Ion Source (EBIS) and the EBIT use the same principle to create HCIs. The main differences between them are the trap size and the electron beam current

density. A typical EBIS has a large trapping region and is surrounded by a solenoid while an EBIT has a shorter trap in a strong magnetic field created by Helmholtz coils. Due to the large trap, the EBIS has large capacity to contain HCIs. On the other hand, the EBIT can provide short breeding times which result from having a strong magnetic field and high electron beam current density.

In an EBIS or EBIT, singly charged or neutral particles are bombarded by a nearly mono-energetic electron beam and become highly charged through electron impact ionization. In EBIS/T devices, one can manipulate the charge state distribution during the charge breeding process by adjusting the electron beam energy and breeding time. A narrow charge state distribution is reached by selecting the electron beam energy to be slightly below an ionizing threshold at atomic shell closures, the so-called closed shell breeding technique, but the charge breeding time is then longer. The charge capacity of the EBIS/T is determined by the electron beam current and energy and the trap size. For example, 2×10^{11} positive charges can be stored in a trap of 0.8 meter long with a 2.5 A electron beam current and an electron beam energy of 11 keV. The operation of EBIS/T is very flexible because it can run in both pulsed and continuous modes with both injection and extraction processes. Because the device is operated under ultra high vacuum of 10^{-11} to 10^{-9} Torr, the beam contamination is low.

Since the acceptance of an EBIS/T is generally small and determined by the size of the electron beam, ion beam cooling can be necessary before transporting SCIs into the EBIS/T. The energy spread of the extracted HCI beam depends on the space-charge potential, charge states of HCIs, extraction voltage, etc. An achromatic separator may be required to select a HCI beam with a certain range of energy spread [14]. The closed shell charge breeding

technique is successfully utilized to narrow charge state distributions and increase charge breeding efficiency. A charge breeding efficiency of 23% of $^{23}Na^{9+}$ has been reported with REX-EBIS at ISOLDE/CERN [12].

1.3 History and applications of EBIS/T

The earliest application of an electron beam compressed by a magnetic field originated in 1929 by Bleakney when he measured the ionization potential of highly charged mercury [15]. In 1968, P. A. Redhead investigated the electron impact ionization process by trapping mercury ions with the electron beam and electrostatic potential [16]. Similar in principle to an ion trap, the EBIS was invented by E. Donets *et al.* and results were discussed in a conference at Saclay in 1969 [17]. In 1989, the Sandia Super-EBIS achieved producing U^{82+} at an energy below 1 keV/Q in order to study interactions between low-energy HCIs [18].

Sharing the same principle of operation with the EBIS, the EBIT developed by M. A. Levine *et al.* [19] was built with a short trapping region and used a pair of Helmholtz coils for generating the magnetic field. Since the EBIT is primarily used for atomic spectroscopy, an open access at the center of the Helmholtz coils allows to observe X-ray emissions.

The EBIS/T base device has been used in several applications [20]. The EBITs at LLNL [21], NIST [22], and MPIK in Heidelberg [23] are dedicated to atomic physics and spectroscopy. The commercial compact Dresden EBIT is used to study the interaction between HCIs and material surfaces [24, 25]. The RHIC-EBIS at BNL is employed to produce a highly charged beam for a pre-injector of the accelerator [26, 27]. Rare isotope beam facilities, such as the REXEBIS at ISOLDE-CERN [28], NSCL EBIT [29, 30], and

CARIBU EBIS at Argonne [31, 32] are devoted to post acceleration while the TITAN EBIT at TRIUMF [33] and the MATS EBIT at FAIR [34] charge breed rare isotopes for mass measurements.

1.4 Charge breeding requirements for reaccelerated beams

The overall efficiency of the EBIT which is determined by the injection and extraction efficiencies, the transport efficiency, the charge breeding efficiency, and the capture efficiency, is given by where $\epsilon_{\text{tot}}, \epsilon_{\text{inj}}, \epsilon_{\text{ext}}, \epsilon_{\text{trans}}$, ϵ_{CB}, and ϵ_{cap} are total, injection, extraction, transport, charge breeding, and capture efficiencies, respectively. The injection, extraction, and transport efficiencies are obtained by optimizing beam transport optics and injecting a SCI beam with small emittance. The SCI beam has to be well focused while entering the trapping region. With the limited yield of the rare isotopes, the highest injection and transport efficiencies are required to ensure that the isotope beam travels into the trap and is not lost during beam transport.

The charge breeding efficiency determines how efficient the EBIT can charge breed ions into a single charge state. Due to the distribution of HCIs, the breeding efficiency is normally limited to between 20% to 40% [12]. However, the closed shell breeding technique has proven to overcome this limitation. A charge breeding efficiency of 90% was experimentally reached [35].

The capture efficiency is a crucial parameter for charge breeding rare isotope beams. The singly charged beam has to overlap well with the electron beam in order that SCIs are efficiently captured. The maximum efficiency is not easily obtained since the electron beam size is generally smaller than 100 μm and several parameters are involved for the

optimization.

1.5 Thesis overview

To investigate ion capture inside the NSCL EBIT and to maximize the efficiency of the EBIT through experiments and a dedicated simulation code, the objectives of the work were

- Optimization of the 60 keV beam transport into the EBIT trap by using SIMION
- Development of a simulation code to investigate ion injection and the capture process
- Observation of the charge state evolution of the externally injected beam from a test ion source
- Measurements to investigate the capture efficiency of the NSCL EBIT and compare these experimental data with simulation results.

The thesis is outlined as follows. Physics of an EBIT and its application as a charge breeder are shown in Chapter and Chapter , respectively. The characteristics of the NSCL EBIT charge breeder are described in Chapter . Chapter contains information about the simulation performed to investigate the capture efficiency. The measurements, results, and discussion of the experiments required for the investigation of the capture efficiency are presented in Chapter . A conclusion and an outlook are described in Chapter .

Chapter 2

Physics of an Electron Beam Ion Source/Trap

In order to investigate the capture efficiency of an EBIT, it is important to understand how the EBIT functions and what physical phenomena occur inside. There are several processes involved and those are discussed in the following sections.

2.1 Electron beam ion source/trap principle

The main components of the EBIS/T are illustrated in Figure 2.1. The EBIS/T primarily consists of the electron beam, cylindrical trap electrodes, and a magnetic field. The mono-energetic electron beam drives the charge breeding process by successive electron impact ionization. The electron beam also creates the space-charge potential to radially confine ions. The electron beam is generated at a cathode, travels through the trap, and is absorbed by an electron collector. The strong magnetic field from a superconducting magnet compresses the electron beam to high current density for fast charge breeding. While being exposed to the high density electron beam, ions are axially trapped and charge bred in the region between two potential barriers: an inner barrier and an outer barrier. The terms of the inner and the outer barriers used throughout the thesis refer to the barriers close to the

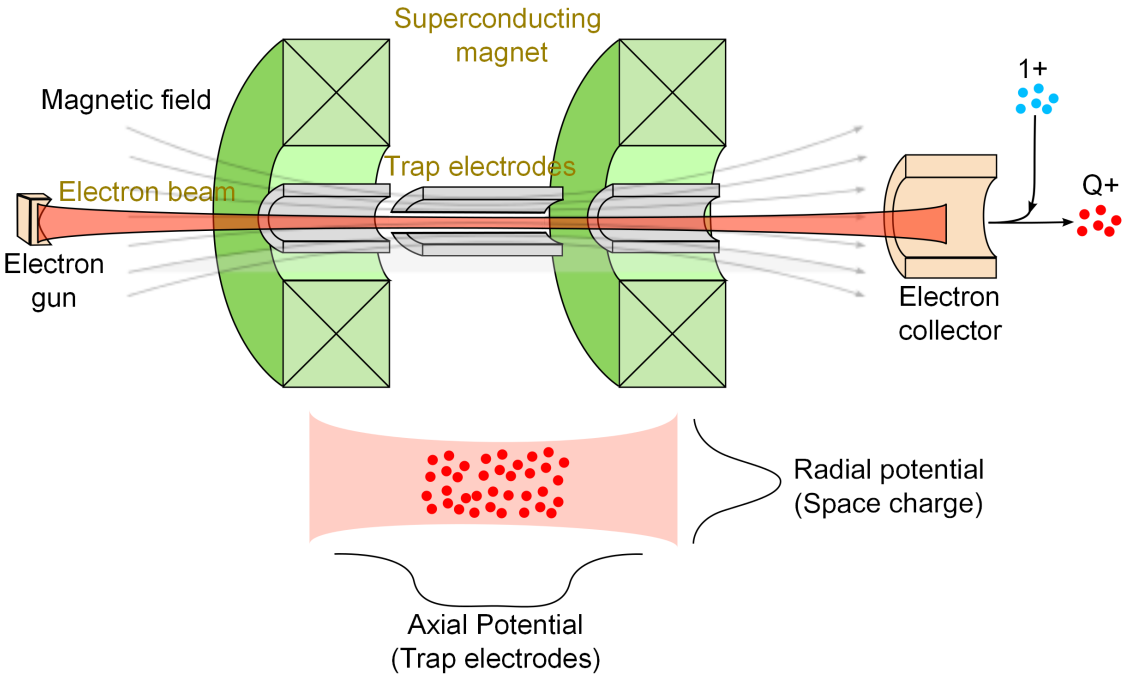

Figure 2.1 EBIT principle. The major components are an electron beam, a magnetic field, and trap electrodes. Singly charged ions are injected and highly charged ions are ejected through a collector.

electron gun and the collector, respectively. Both barriers are formed by applying different voltages to trap electrodes. After charge breeding for a certain amount of time, the HCIs are extracted toward and through the collector by lowering the outer barrier voltage.

Singly charged ions can be externally injected through the collector to the EBIS/T trapping region. Depending on the application, neutral gas can be introduced into the EBIS/T via a radial open gap. Unless specified otherwise, from now on, the term "EBIT" will be used for both the EBIS and the EBIT for simplicity.

2.2 Electron beam and space-charge potential

The maximum compression of the electron beam can be obtained when the conditions of the ideal Brillouin flow are satisfied. The electrons are generated from the cathode which

has zero temperature and situates in the magnetic field free region. The Brillouin radius r_b is,

$$r_b = \frac{1}{B}\sqrt{\frac{I_e}{\pi\epsilon_0}}\left(\frac{2m_e^3}{E_e e^2}\right)^{1/4}, \tag{2.1}$$

where I_e is the electron beam current, E_e is the electron beam energy, B is the magnetic field, m_e is the electron mass, e is the elementary charge, and ϵ_0 is the vacuum permittivity. Practically, it is impossible to have a zero temperature at the cathode. By including the finite temperature at the cathode, the electron beam radius is well predicted by the Herrmann theory [36]. The Herrmann radius r_h defines a boundary where 80% of the electron beam passes through and is given by

$$r_h = r_b\sqrt{\frac{1}{2}+\frac{1}{2}\sqrt{1+4\left(\frac{8kT_c r_c^2 m_e}{e^2 r_b^4 B^2}+\frac{B_c^2 r_c^4}{B^2 r_b^4}\right)}}, \tag{2.2}$$

where k is the Boltzmann constant, T_c is the cathode temperature, r_c is the cathode radius, and B_c is the magnetic field at the cathode. Maximum electron beam compression is obtained if $B_c = 0$. This is the reason why the electron gun is designed to cancel the field at the cathode as much as possible. For the NSCL EBIT, the electron beam radius is 80 μm, with $I_e = 150$ mA, $E_e = 19.5$ keV, $B = 2$ T, $B_c = 10$ G, $r_c = 3.175$ mm, and $T_c = 1400$ K. It is obvious from the equation that the magnetic field plays a major role in determining the electron beam size. By increasing the magnetic field inside the trap, the electron beam radius becomes smaller and the beam density larger.

The distribution of the electron beam density is studied with two different approaches: a homogeneous and a Gaussian profile. Both approaches can provide analytical solutions of space-charge potential and a comparison between the space-charge potential solved by both

distributions is discussed in Ref. [37, 38]. However, the former approach is more suitable to the simulation because it is easier to acquire the analytical solution of the electric field along the electron beam axis. Due to this advantage, the homogeneous electron density is employed. The electron beam density is assumed to be uniform up to the Herrmann radius, beyond which it vanishes.

The space-charge potential ϕ_{SC} is straightforwardly computed by solving the Poisson's equation with the homogeneous density and given by

$$\phi_{SC}(r) = \frac{Q_e}{2\pi\epsilon_0} \begin{cases} \left[\frac{1}{2}\left(1 - \frac{r^2}{r_h^2}\right) + \ln\frac{r_T}{r_h}\right] & : \ 0 < r < r_h \\ \ln\frac{r_T}{r} & : \ r_h < r < r_T, \end{cases} \tag{2.3}$$

where Q_e is the total charge per unit length equivalent to the ratio between the electron beam current and the electron velocity (I/v_e) and r_T is the drift tube radius. The depth of the radial potential is

$$\phi_{SC}(0) = \frac{Q_e}{2\pi\epsilon_0}\left(\frac{1}{2} + \ln\frac{r_T}{r_h}\right). \tag{2.4}$$

With a 2 T magnetic field, a 0.135 A and 19.5 keV electron beam from a 3.175 mm cathode, and a trap electrode radius of 5 mm, the central space-charge potential is -115 V.

During the electron beam propagates, the electron beam energy is affected by the potential created by itself and can be corrected in a "self-consistent" way. The correction can be solved by an iterative or an analytical method. The latter approach will be employed in

the simulation. Starting from the iterative method, the correction is

$$\begin{aligned} E_1 &= E_0 + \phi_{0,sc}(0) \\ &= E_0 + \frac{C}{\sqrt{E_0}} \\ E_2 &= E_0 + \frac{C}{\sqrt{E_1}} \\ &\vdots \quad \vdots \quad \vdots \\ E_n &= E_0 + \frac{C}{\sqrt{E_{n-1}}}, \end{aligned} \tag{2.5}$$

where $C = C(I,\, r_T,\, r_h)$ is from Eq. 2.4 in which Q_e is replaced by $I\sqrt{m_e/2E_0}$ and $\sqrt{1/E_0}$ is neglected. Subscripts indicate the order of the correction. If the iteration converges, then for large n, $E_n = E_{n-1}$ leading to

$$E_n = E_0 + \frac{C}{\sqrt{E_n}}. \tag{2.6}$$

The equation is rearranged as

$$E_n^3 - 2E_n^2 E_0 + E_n E_0^2 = C^2 \tag{2.7}$$

which can be solved analytically. If the electron beam energy satisfies the condition $E_0 > 3|C|^{2/3}/2^{2/3}$, the real solution is obtained and given by

$$E_n = E_0 - E_0\frac{\arccos(\delta)}{3\sqrt{3}} - E_0\frac{\arccos^2(\delta)}{54}, \tag{2.8}$$

where $\delta = 1 - 27C^2/2E_0^3$. For example, results of the electron beam energy with correction

and the space-charge potential which are computed based on the NSCL EBIT geometry are displayed in Figure 2.2. With an electron beam current of 2.4 A, a magnetic field of 6 Tesla, and $E_0 = 12.5$ keV at the trapping region, the difference in potential calculated with and without correction is 0.75 kV.

2.3 Ion motion

Ion motion in a combined electric and magnetic field is simply described by the Lorentz equation,

$$m\mathbf{a} = q\left(\mathbf{E} + \mathbf{v} \times \mathbf{B}\right). \tag{2.9}$$

where m, q, $\mathbf{a}$, $\mathbf{v}$ are ion mass, charge, acceleration, and velocity, respectively, and $\mathbf{E}$ and $\mathbf{B}$ are the electric and the magnetic field. The effect of the space-charge field and the magnetic field on ion motion is discussed in the following. Due to the axial symmetry, only the axial and radial components contributed by space-charge are considered as

$$\mathbf{E} = \mathbf{E}_r + \mathbf{E}_z = -\nabla_r \phi_{sc} - \nabla_z \phi_{sc}. \tag{2.10}$$

Assuming the magnetic field inside the trap is along the axis, then $\mathbf{B} = B_z \mathbf{e_Z} = B$. At small radii, the radial magnetic field component is approximately given by $B_r = -\frac{1}{2} r \frac{dB_z}{dz}$. The equations of motion including the space-charge field are, inside the electron beam $\left(r \leq r_h\right)$,

$$\begin{aligned} \ddot{x} &= \frac{q}{m}\frac{Qe}{2\pi\epsilon_0}\frac{1}{r_h^2}x + \frac{q}{m}B\dot{y} \\ \ddot{y} &= \frac{q}{m}\frac{Qe}{2\pi\epsilon_0}\frac{1}{r_h^2}y - \frac{q}{m}B\dot{x} \end{aligned} \tag{2.11}$$

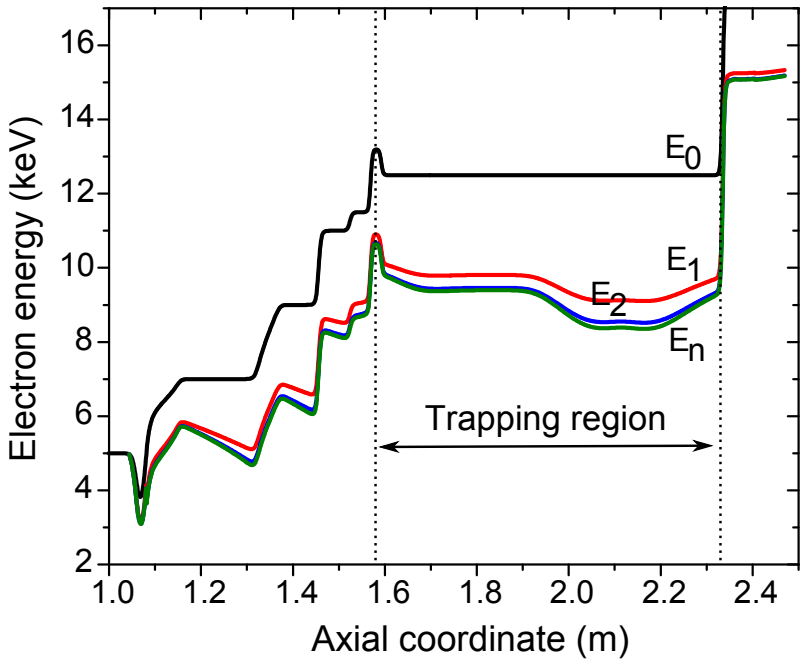

(a)

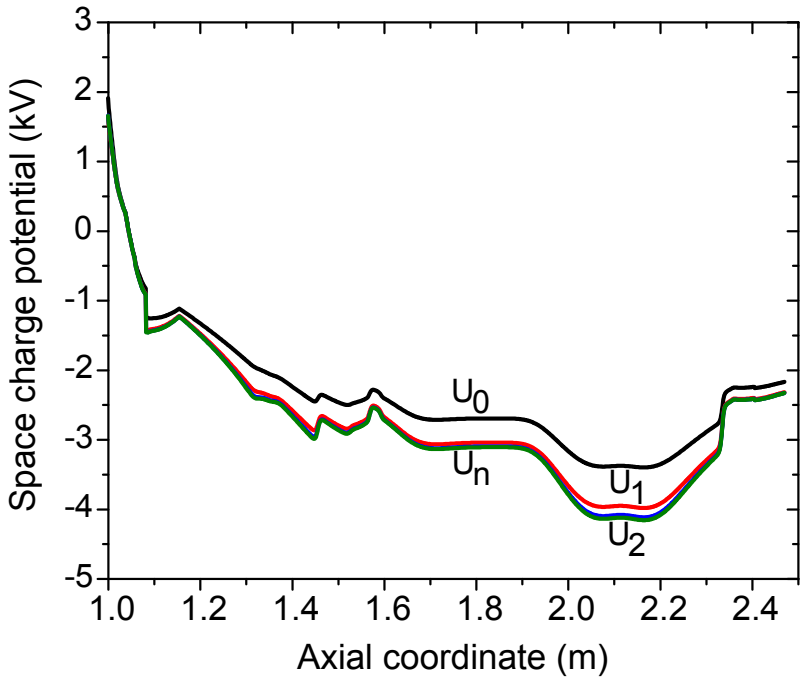

(b)

Figure 2.2 Electron beam energy with correction (a) and space-charge potential (b) for the first (black), the second (red), the third (blue), and the n-th order (green) corrections calculated for the NSCL EBIT geometry (see text for details).

$$\ddot{z} = \frac{q}{m}\frac{Q_e}{2\pi\epsilon_0}\left\{v_z\frac{\partial v_z}{\partial z}\left[\frac{1}{2}\left(1-\frac{r^2}{r_h^2}\right)+\ln\left(\frac{r_T}{r_h}\right)\right]-\frac{1}{r_T}\frac{\partial r_T}{\partial z}+\frac{1}{r_T}\frac{\partial r_h}{\partial z}\left(1-\frac{r^2}{r_h^2}\right)\right\}$$

and outside the electron beam $\left(r_h < r < r_T\right)$,

$$\begin{aligned}\ddot{x} &= \frac{q}{m}\frac{Q_e}{2\pi\epsilon_0}\frac{x}{x^2+y^2}+\frac{q}{m}B\dot{y}\\ \ddot{y} &= \frac{q}{m}\frac{Q_e}{2\pi\epsilon_0}\frac{y}{x^2+y^2}-\frac{q}{m}B\dot{x}\end{aligned} \tag{2.12}$$

$$\ddot{z} = \frac{q}{m}\frac{Q_e}{2\pi\epsilon_0}\left[v_z\frac{\partial v_z}{\partial z}\ln\left(\frac{r_T}{r_h}\right)-\frac{1}{r_T}\frac{\partial r_T}{\partial z}\right].$$

We can see that the axial acceleration is determined by the tube radius, the Herrmann radius, their changes along the axis, and the change of the ion energy along the axis. In the NEBIT code, which will be discussed in Chapter , these equations are numerically solved for the ion motion at each time step and the derivatives of r_h and r_T with respect to the axial coordinate are calculated by the two-point backward-difference formula [39].

2.4 Ion processes

In the EBIT, ions can undergo many processes. The main processes involving charge state changes are electron impact ionization (EI), radiative recombination (RR), and charge exchange (CX). There are also processes contributing to ion dynamics: ion heating by the electron beam and by ion-ion energy exchange. Details of these processes are described in Ref. [37]. Figure 2.3 illustrates the charge state evolution of an argon ion. The vertical axis represents the ionization energy for the different charge states. The inset illustrates charge state development and an ion escape from the trap.

The total cross section of the RR process, which is obtained from Kim and Pratt [40],

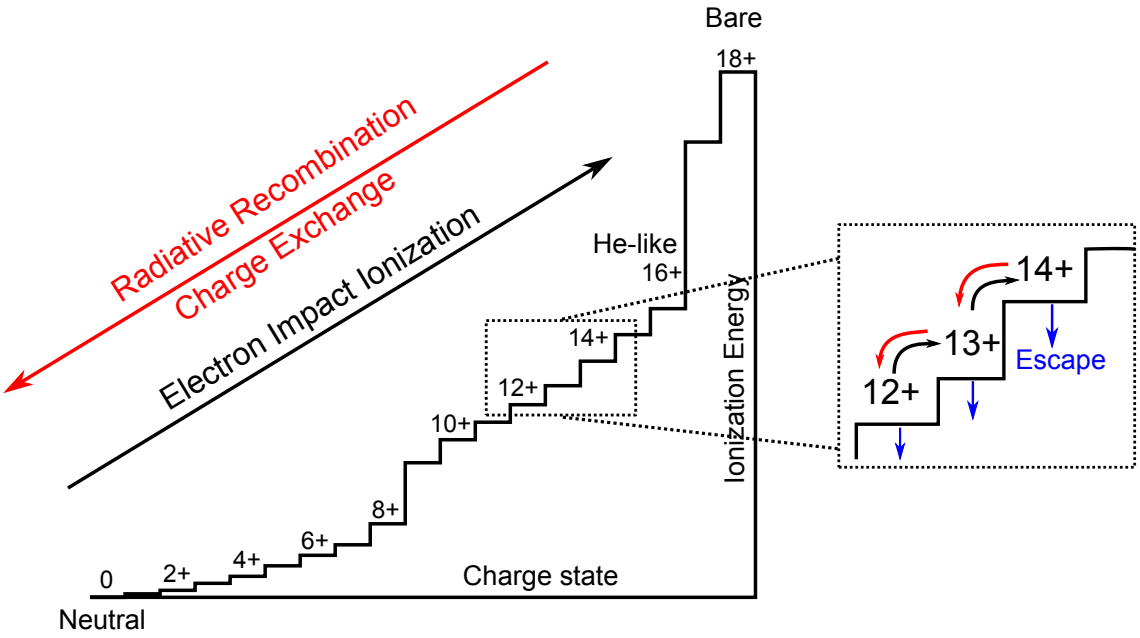

Figure 2.3 Schematic showing the atomic processes of an argon gas in the EBIT.

scales with Z_{eff}^2/K where K is the incident electron kinetic energy and Z_{eff} is the average of the ion's atomic number and charge state. The discussion in Ref. [37] shows a comparison between the RR and the EI cross sections of various krypton charges for a 20 keV electron beam. At low charge states ($< 10+$), the RR cross section is smaller than the EI cross section by a factor of 10^5. The RR process starts to dominate at Kr^{35+} where the RR and EI cross sections are comparable. The total cross section of the CX process between ions and residual gas can be calculated by the Müller and Salzborn formula [41]. With a pressure inside the EBIT of 10^{-11} Torr and 20 ms of charge breeding time, the probability for the CX process to occur is $< 0.02\%$ and negligible [42].

In Ref. [38], the ion heating by the electron beam and the ion-ion energy exchange are calculated for Kr^{34+} and Kr^{30+}, respectively. The heating requires about 1 ms for the Kr^{34+} to reach the maximum confinement energy and causes the ion to escape from the trap. The momentum exchange of ion-ion collision of Kr^{30+} also needs approximately 1 ms

to be Boltzmann distributed. Given these time scales, it is reasonable to exclude these two interactions in ion capture simulations.

The EI process is the most important process to produce HCIs. It is simply explained by removing an electron orbiting an ion with $Z+$ charge state by a high-energy electron and the charge state of the ion changing to $(Z+1)+$. The reaction can be written as

$$A^{Z+} + e \rightarrow A^{(Z+1)+} + 2e. \tag{2.13}$$

The cross section of the reaction can be parametrized by W. Lotz's semi-empirical formula [43],

$$\sigma_{EI}\left(E_e\right) = \sum_{j=1}^{n} a_j q_j \frac{\ln\left(E_e/I_j\right)}{E_e I_j}\left\{1 - b_i \exp\left[-c_j\left(E_e/I_j - 1\right)\right]\right\}, \tag{2.14}$$

where a_j, b_j, c_j are free parameters specific to each ion and charge state, I_j is the ionization energy, q_j is the number of electrons in the jth subshell, E_e is the electron energy, and n is the number of subshells in the atom which meets the condition $E_e > I_j$. The maximum cross section is approximately 2 - 3 times the ionization threshold energy. As an example, for an electron beam energy of 1 keV, the cross section of K^{39} for 2+ to 3+ charge state change is 3.2×10^{-17} cm^2. Figure 2.4 shows the EI cross section of a potassium ion as a function of electron beam energy. In order to further ionize an ion, the electron beam energy must be greater than the threshold energy of each charge state. The ionization probability of the reaction is given by

$$p = 1 - e^{-\frac{t_{EB}}{t_{1\rightarrow 2}}}, \tag{2.15}$$

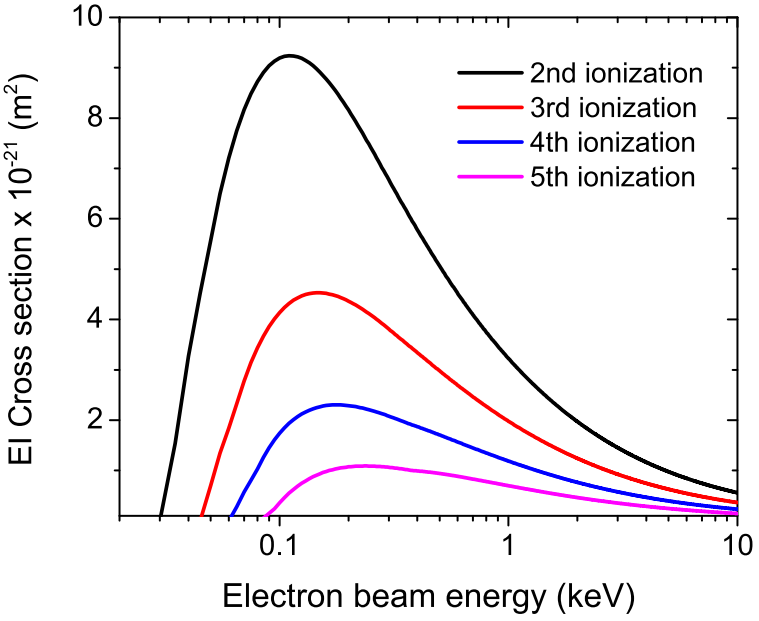

Figure 2.4 Electron impact ionization cross section of K^+ as a function of electron beam energy. The electron beam energy is required to be greater than the binding energy in order to produce the EI process.

with t_{EB} and $t_{1\to2}$ being the time required for an ion to spend inside the electron beam and to be ionized from a 1+ to a 2+ charge state, respectively. The time $t_{1\to2}$ is related to the EI cross section by

$$t_{1\to2} = \frac{e}{j_e \sigma_{EI}}, \tag{2.16}$$

where $j_e = 0.8\, I_e/\pi r_h^2$ is the electron beam current density. The time scale of this process is in a range of μs for an electron beam current density of 10^4 A/cm^2. The factor of 0.8 results from the Herrmann radius where πr_h^2 encloses 80% of the electron beam.

For a number of ions in a charge state i, the EI process can be described by the rate equation [37, 44],

$$\frac{dn_i}{dt} = n_e \nu_e \left[\sigma^{EI}_{i-1\to i} n_{i-1} - \sigma^{EI}_{i\to i+1} n_i\right] \tag{2.17}$$

where n_e, ν_e are density and velocity of the electrons, n_{i-1}, n_i, n_{i+1} are ion density in state $i-1$, i, $i+1$, and σ^{EI} is the cross section of the EI process for a given charge state. The equation is valid when assuming the ions are inside the electron beam with a constant electron beam current density. This rate equation will be used to benchmark the NEBIT code (see Section 5.4.4) and to calculate the effective current density (see Section 6.4.2).

Chapter 3

The EBIT as a Charge Breeder

Optimizing an EBIT as a charge breeder for rare isotope beams requires additional features than for standard physics applications. The injection process of singly charged ions, the extraction of highly charged ions (HCIs), and the ion capture process are described in the following as well as the physics of the ion beams.

3.1 Injection and extraction

A gas jet of neutral atoms or molecules can be injected into the EBIT through a radial port pointing at the center of the trap electrodes. When the jet passes through the electron beam, neutral particles are ionized and trapped by the space-charge potential created by the electron beam. This method to load ions into the trap has been used during the commissioning phase of the NSCL EBIT. To charge breed a rare isotope beam, the singly charged ion beam is injected through the collector as mentioned in Section 2.1. There are two methods in use for external injection: pulsed injection and continuous injection [45].

The pulsed injection concept is shown in Figure 3.1. A pulsed beam is injected into the EBIT and confined by the outer barrier of the trap which has to be pulsed between the injection and the extraction processes. In order to maximize the efficiency, the ion beam is first bunched by a bunching device such as an RFQ buncher before being injected into the

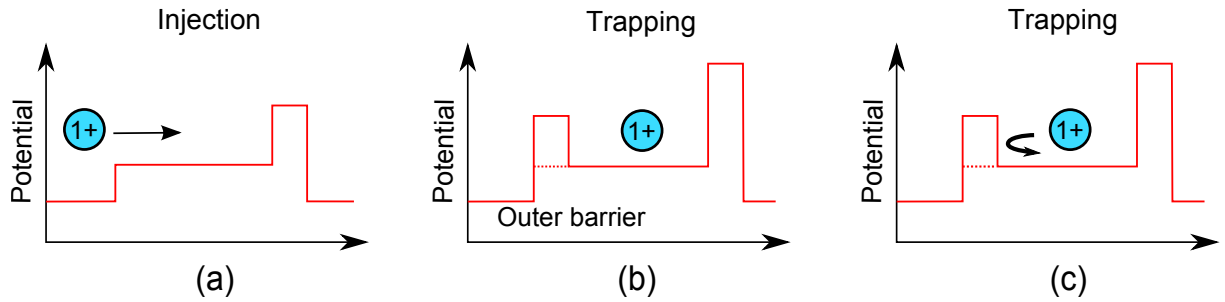

Figure 3.1 Pulsed injection process. (a) An ion is injected into the trap, (b) the outer barrier is raised up, and (c) the ion is confined inside the trapping region.

EBIT. The TITAN EBIT [46] and the REXEBIS [4] have successfully demonstrated the charge breeding of rare isotope beams using the pulsed injection.

In the continuous injection mode, also known as the accumulation mode, an ion beam is continuously injected into the trap. Figure 3.2 illustrates this concept. During the injection process, both potential barriers are fixed. The continuous ion beam with an energy slightly higher than the outer barrier is injected into the EBIT. Within a round-trip flight from the outer barrier, the ion is trapped if it loses at least one additional electron. Otherwise, it will leave the trap. The continuous injection has been demonstrated at REXEBIS and the total efficiencies of different injected beams are reported in Ref. [42, 47]. The capture efficiency of continuous injection is very dependent on the emittance of an injected ion beam. Ions that have large emittance are likely to reflect off the barrier due to the radial energy pickup because when crossing the magnetic field, the ions partially convert axial into radial energy. For the NSCL EBIT, the continuous injection is employed to avoid adding a bunching device which would limit the maximum beam intensity of the singly charged ions.

HCIs can be extracted from the EBIT with three possible methods: leaky, fast, and pulsed extraction. The concept of each extraction scheme is depicted in Figure 3.3. For the leaky extraction, also called slow extraction, the ions are continuously extracted from

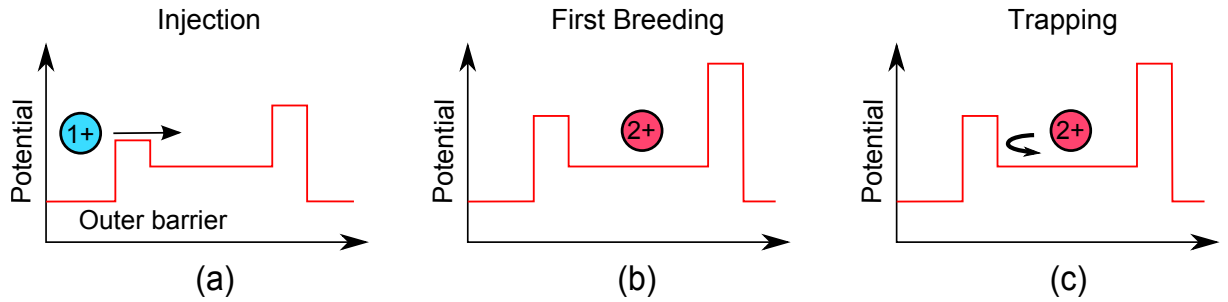

Figure 3.2 Continuous injection process. (a) An ion is injected with the energy slightly above the outer barrier, (b) the ion experiences the higher barrier after being charge bred, and (c) the ion is confined inside the trapping region.

the trap when they have enough axial energy to overcome the confinement barrier. The HCIs can gain energy from the electron heating process and ion-ion collisions. This method provides the extracted beam with a small energy spread.

By shaping the trap potential to a slope configuration, similar to Figure 3.3b, the HCIs are extracted fast as a pulsed beam. This method is valid only if the trap comprises several electrodes which provide flexibility to create different potential configurations. With a quick extraction period, the cycle of the charge breeding process can begin in a short time interval. However, the extracted beam tends to have large energy spread. By lowering the outer barrier to let the HCIs leave the trap without shaping the trap potential, shown in Figure 3.3c, the pulsed beam can be extracted with smaller energy spread. This method has been used in the NSCL EBIT.

3.2 Ion capture

Before being charge bred into HCIs, the singly charged ions have to be captured successfully by losing at least one addition electron via the electron impact ionization that leads to their confinement in the EBIT. This ion capture process is directly related to the overlap of the

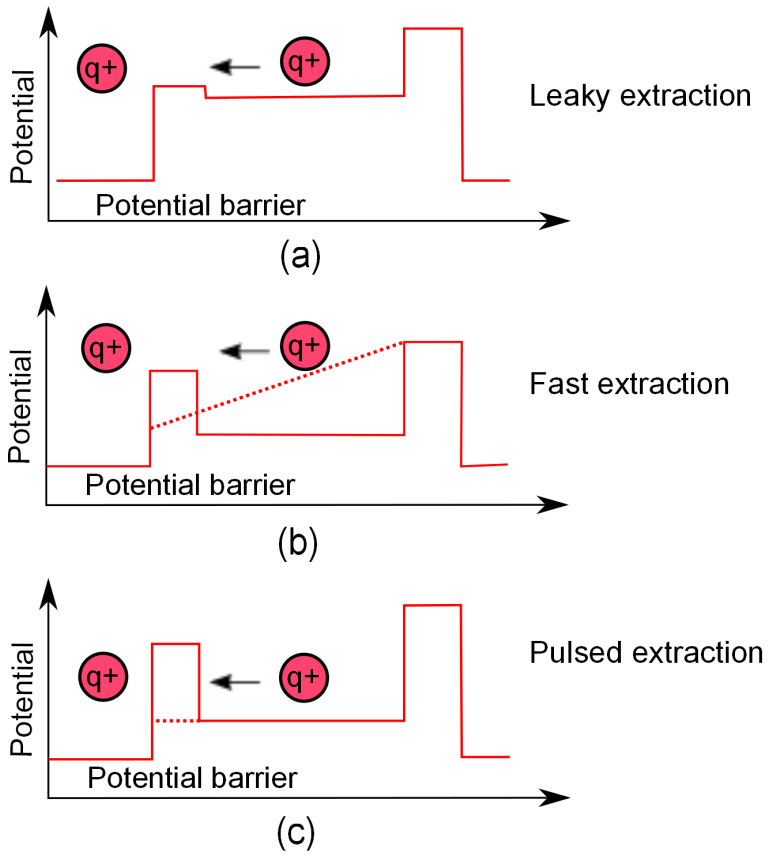

Figure 3.3 Three possible methods to extract HCIs from the EBIT: (a) leaky , (b) fast, and (c) pulsed extraction.

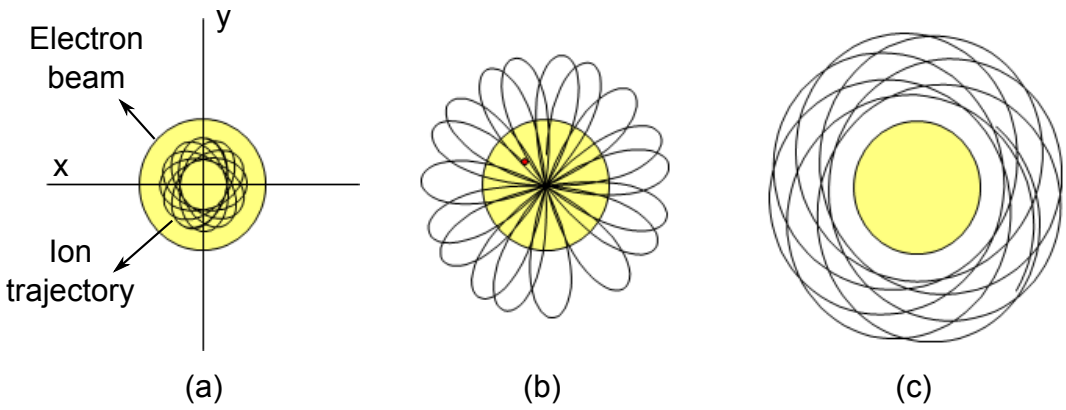

Figure 3.4 Three possible ion trajectories in the trap. The ion trajectory is (a) completely inside the electron beam, (b) partially inside the electron beam, and (c) totally outside the electron beam.

injected ion beam and the electron beam. The overlap can be described by three scenarios: full, partial overlap, and no overlap as shown in Figure 3.4. The full overlap occurs when the ion beam trajectories are entirely inside the electron beam. In this case, the possibility for the ions to lose one electron and then be trapped in the EBIT within a round-trip flight is large. If the ion beam trajectories partially overlap with the electron beam due to a high radial velocity or misalignment, the ions have less chance to lose one electron and become trapped. In the worst case scenario that the ion trajectories are totally outside the electron beam and the ions never interact with the electrons, the charge breeding process will never take place. For a beam with small emittance, the best overlap can be achieved by optimizing the beamline transport optics.

Alternatively, the overlap between the ion beam and the electron beam can be improved by increasing the electron beam size. However, the better overlap has to be traded with the lower electron beam current density and consequently longer charge breeding time, see Eq. 2.16.

3.3 Trap capacity

The capacity of the trap is important to determine the number of HCIs stored in the EBIT charge breeder. Depending on the electron beam current I, the trap size L, and the electron beam energy U_e in unit of eV, or velocity v_e, the trap capacity is given by

$$\text{Trap capacity} = \frac{\rho_l L_{\text{trap}}}{e} = \frac{I \times L_{\text{trap}}}{e v_e} = \frac{I \times L_{\text{trap}}}{e\sqrt{2\frac{e}{m_e}U_e}} \tag{3.1}$$

where ρ_l is linear charge density equivalent to I/v_e, and e and m_e are electronic charge and mass, respectively. For a 135 mA and 19.5 keV electron beam and 0.6 m trap size, the trap capacity of singly charged ions is 6.5×10^9 ions.

Not only does a larger trap size provide a greater number of stored ions, but it also extends the time the singly charged ions spend inside the trap. As shown in Eq. 2.15, the longer the interaction time, the higher the ionization probability will be.

3.4 Beam dynamics

3.4.1 Beam emittance

The quality of a charged beam can be quantified by "emittance," an area occupied by the beam in six-dimensional phase space: two in longitudinal and four in transverse directions. The longitudinal emittance which well describes the quality of a pulsed beam is defined by the phase difference $\Delta\phi$ and the energy spread ΔW. Without an optical element that couples between the longitudinal and transverse motions, the longitudinal emittance can be

considered separately from the transverse emittance. More details about the longitudinal emittance can be found in Refs. [48, 49].

The transverse emittance of a beam is determined by two transverse coordinates (x, y) and two angles ($x' = v_x/v_z$, $y' = v_y/v_z$) of the ions. If the beam transport system does not couple horizontal and vertical motions, the phase spaces of $x - x'$ and $y - y'$ can be considered separately and are equivalent for a system with axial symmetry. The emittance of the beam is constant, if the number of the particles is constant and there are no dissipative forces involved such as radiation.

From the statistical point of view the r.m.s. emittance ($\epsilon_{\rm rms}$) can be obtained from an ellipse in the phase space (x, x'), illustrated in Figure 3.5, which is defined by Twiss parameters: $\alpha_{\rm rms}, \beta_{\rm rms}$, and $\gamma_{\rm rms}$ [50]. The ellipse equation containing ions in phase space is given by

$$\gamma_{\rm rms} x^2 + 2\alpha_{\rm rms} x x' + \beta_{\rm rms} x' = \epsilon_{\rm rms}, \tag{3.2}$$

where $\gamma_{\rm rms}\beta_{\rm rms} - \alpha_{\rm rms}^2 = 1$ and $\epsilon_{\rm rms} = \sqrt{\overline{x^2}\,\overline{x'^2} - \overline{xx'}^2}$. The Twiss parameters are calculated from the second-moment of the particle distribution,

$$\beta_{\rm rms} = \frac{\overline{x^2}}{\epsilon_{\rm rms}}, \quad \gamma_{\rm rms} = \frac{\overline{x'^2}}{\epsilon_{\rm rms}}, \quad \alpha_{\rm rms} = -\frac{\overline{xx}}{\epsilon_{\rm rms}}. \tag{3.3}$$

3.4.2 Effective ellipse transformation

Eq. 3.2 can alternatively be written in a matrix form by

$$X^T \sigma X = \epsilon \tag{3.4}$$

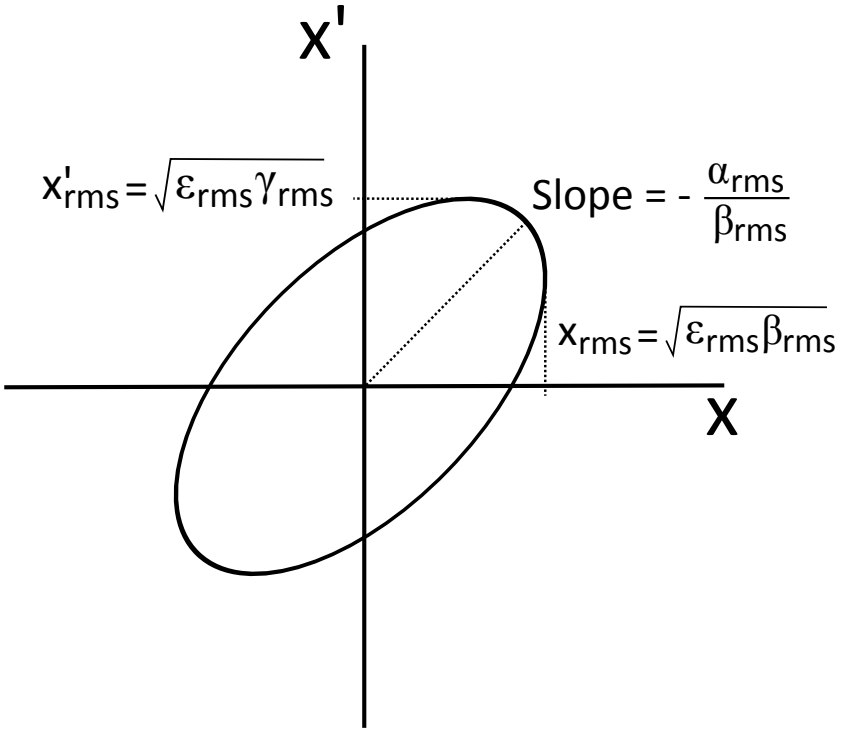

Figure 3.5 The r.m.s. ellipse in the phase space.

where $X = \begin{bmatrix} x \\ x' \end{bmatrix}, X^T = \begin{bmatrix} x & x' \end{bmatrix}$, and $\sigma^{-1} = \begin{bmatrix} \gamma & \alpha \\ \alpha & \beta \end{bmatrix}$ is an inverse beam matrix. Due to the invariance of the emittance, the transformation of the beam matrix between two locations is

$$\sigma_1 = \mathrm{R}\,\sigma_0\,\mathrm{R}^T \tag{3.5}$$

where R is a 2×2 transfer matrix that describes how the particle is transported. Considering an ion with x and x' travels through a drift region, the linear transformation of the ion's

position and angle is given by

$$\begin{bmatrix} x_1 \\ x_1' \end{bmatrix} = \begin{bmatrix} 1 & L \\ 0 & 1 \end{bmatrix} \begin{bmatrix} x_0 \\ x_0' \end{bmatrix}, \tag{3.6}$$

where L is a drift length. The angle remains unchanged, $x_1' = x_0'$ while the coordinate is dependent on the drift length by $x_1 = 1 + x_0' L$. For a complicated system comprising several optical elements, the transfer matrix is simply calculated by the multiplication of transfer matrix of each element, $\mathrm{R} = \mathrm{R}_1\mathrm{R}_2...\mathrm{R}_n$, and the beam property is transformed by

$$\begin{bmatrix} \beta_1 \\ \alpha_1 \\ \gamma_1 \end{bmatrix} = \begin{bmatrix} R_{11}^2 & -2R_{11}R_{12} & R_{12}^2 \\ -R_{11}R_{21} & 1+2R_{12}R_{21} & -R_{12}R_{22} \\ R_{21}^2 & -2R_{21}R_{22} & R_{22}^2 \end{bmatrix} \begin{bmatrix} \beta_0 \\ \alpha_0 \\ \gamma_0 \end{bmatrix}. \tag{3.7}$$

The above transformation is useful to determine the emittance of the beam. For the quadrupole emittance scan method, discussed more details in Section 6.1, the r.m.s. beam size ($\sqrt{\epsilon_{\mathrm{rms}}\beta_1}$) is directly measured. With known transfer matrix elements R_{11} and R_{12} that describe the quadrupole strength, the emittance is obtained by fitting the square of the r.m.s. beam size to the quadrupole strength with the following formula,

$$\begin{aligned} \epsilon_{\mathrm{rms}}\beta_1 &= \epsilon_{\mathrm{rms}} \left(\beta_0 R_{11}^2 - 2\alpha_0 R_{11}R_{12} + \gamma_0 R_{12}^2 \right) \\ \overline{x^2} &= C_1 R_{11}^2 - C_2 R_{11}R_{12} + C_3 R_{12}^2 \end{aligned} \tag{3.8}$$

where C_1, C_2, and C_3 are constant and given by

$$C_1 = \epsilon_{\text{rms}}\beta_0$$

$$C_2 = 2\epsilon_{\text{rms}}\alpha_0$$

$$C_3 = \frac{\epsilon_{\text{rms}}^2 + (\epsilon_{\text{rms}}\alpha_0)^2}{\epsilon_{\text{rms}}\beta_0}.$$

3.4.3 Geometrical acceptance

Similar to the emittance, the acceptance depicts an area in phase space to represent the ability to accept the injected beam. The acceptance contains information on the beam size and orientation for proper focusing. The acceptance which depends on the electron beam current and energy, the magnetic field, and the extraction voltages, is called a geometrical acceptance. The geometrical acceptance defines the phase space of the ion beam that fits inside the electron beam in the EBIT. The geometrical acceptance α, used to test the NEBIT code in Chapter , is analytically given by [42]

$$\alpha = \pi \frac{r_e}{\sqrt{2U_{ext}}} \left(Br_e \sqrt{\frac{q}{m}} + \sqrt{\frac{qB^2 r_e^2}{4m} + \frac{\rho_l}{2\pi\epsilon_0}} \right), \tag{3.9}$$

where r_e is the electron beam radius, U_{ext} is the injection potential, q is the ion charge, m is the ion mass, B is the magnetic field that compresses the electron beam, and $\rho_l = I/v_e$ is the linear charge density. With NSCL EBIT design parameters of a 2.5 A and 30 keV electron beam, a 6 T magnetic field, 0.8 m trap size, and for a 60 keV injected potassium beam, the geometrical acceptance is 6.8 π mm·mrad. In other words, a 100% capture efficiency is expected for an injected beam of up to 6.8 π mm·mrad if the EBIT can limitlessly accept

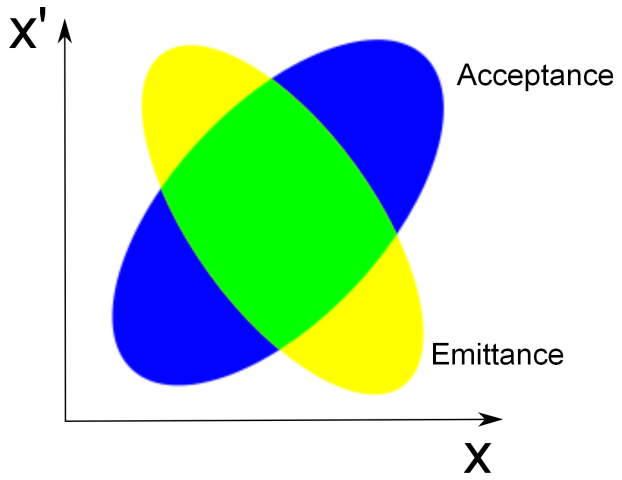

Figure 3.6 Capture probability calculated from the overlapped area in the phase space between emittance and acceptance.

the beam.

By considering together the emittance and the acceptance, the overlap of both areas in the phase space displayed in Figure 3.6 is interpreted as the probability that the ion will be captured by the electron beam. The probability is maximized if the ion beam emittance completely overlaps with the acceptance of the EBIT.

Chapter 4

The NSCL EBIT Charge Breeder

This chapter describes the experimental setup. Figure 4.1 gives an overview of the EBIT charge breeder including its test ion source and the Q/A separator. Electrostatic optical elements are installed at several locations to guide the ion beams along the beamline. Diagnostic tools, including microchannel plates (MCPs) and Faraday cups, are mounted at different Beam Observation Boxes (BOBs) to monitor the ion beam currents and shapes. Section 4.1 describes the main components of the EBIT. A description of the ion source used for the EBIT commissioning can be found in Section 4.2. Sections 4.3 and 4.4 contain information on the Q/A separator and diagnostic devices, respectively. Details of the beamline transport optical elements are presented in Section 4.5.

4.1 NSCL electron beam ion trap characteristics

The NSCL EBIT was built in collaboration with MPIK in Heidelberg and TRIUMF. Starting from the design of the TITAN EBIT [51], a number of changes were implemented to fulfill the requirements of the rare isotope reaccelerator. The electron gun design was modified to provide a higher electron beam current. By adding together the EBIT and EBIS characteristics, the magnet design was changed to a combination of a solenoid and Helmholtz coils [52]. Table 4.1 lists requirements and design parameters for the NSCL

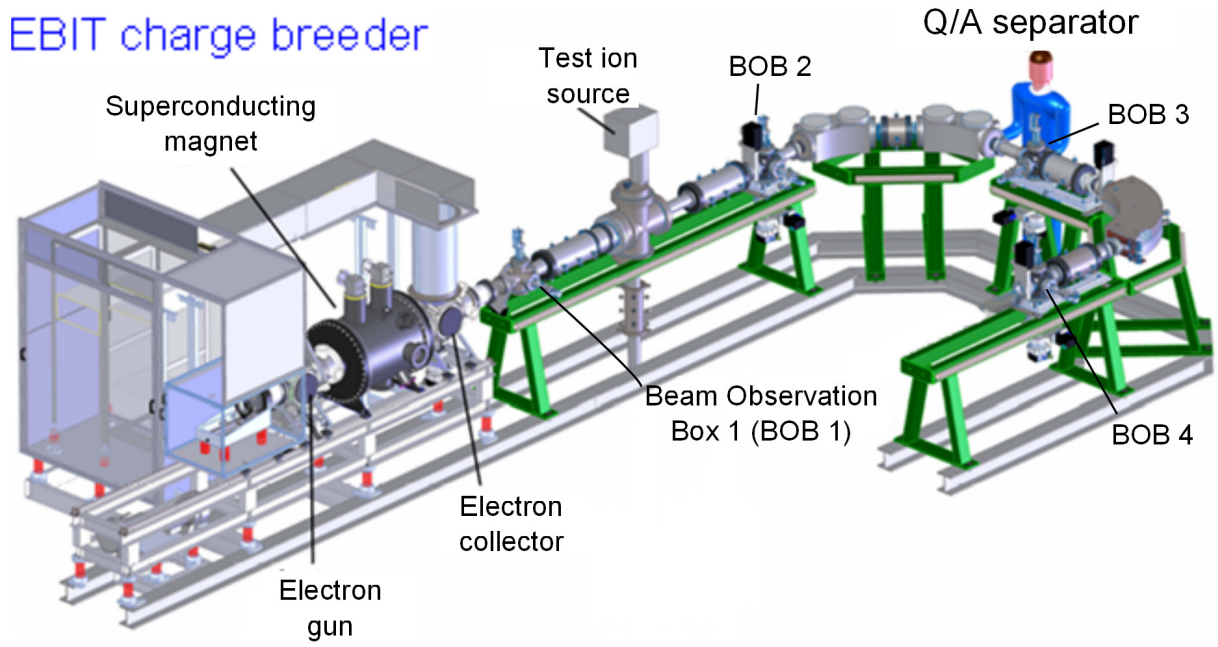

Figure 4.1 Overview of the NSCL EBIT charge breeder.

EBIT. The breeding time is estimated to be of the same order as the time used in the gas stopping process [53]. The total efficiency expected is based on the efficiency REXEBIS [54] reached at the time that the ReA project was initiated. A large number of stored charges is required in order to support the high intensity beams needed for the future FRIB operation. To attain these requirements, the NSCL EBIT was constructed according to the listed design parameters. For fast charge breeding, the NSCL EBIT aims to reach up to 10^4 A/cm^2 which requires a high magnetic field of 6 T and a high electron beam current of 2.5 A. An electron beam energy of up to 30 keV is sufficient to charge breed uranium into the neon-like charge state. The long trap length increases the number of ions that can be stored and the total efficiency.

Requirements		Design parameters	
Breeding time	< 50 ms	Electron beam energy	< 30 keV
Total efficiency	20 - 50 %	Electron beam current	< 2.5 A
Stored positive charges	10^{10} charges	Length of trapping region	0.8 m
		Magnetic field	6 T
		Electron beam current density	$< 10^4$ A/cm^2

Table 4.1 NSCL EBIT requirements and parameters. The choices for the design parameters to satisfy the performance requirements are described in more details in the text.

4.1.1 Electron gun and collector

The electron gun consists of a Pierce-type cathode, an anode, and a focusing electrode. Using a plug-in design, the electron gun core with a cathode of 6.35 mm in diameter can be easily replaced by one with a cathode of 12.7 mm in diameter. The small and the large cathodes were designed to provide up to 1.4 A and 2.5 A of electron beam current, respectively. The drawing and the picture of the assembled electron gun head is depicted in Figure 4.2(a, b). Since the compression of the electron beam inside the trap is influenced by the magnetic field B_C at the cathode (see Eq. 2.2), the compression is maximized if B_C vanishes. Therefore, the fringe field from the superconducting magnet is reduced by a soft iron shield with a thickness of 15 mm and canceled by a magnetic field created by bucking coils inside the iron shield. The coil outside the shield improves the electron beam transport into the fringe field region. By applying 1 A of current, the set of three coils and the front coil produce 60 G at the cathode and up to 120 G at the transition region from the electron gun to the EBIT trapping region.

After passing the trapping electrodes, the electron beam is absorbed by the collector. Figure 4.2(c, d) shows a drawing and photos of the collector electrode, and its full assembly. The magnetic field inside the collector is reduced by the magnetic field from the coil

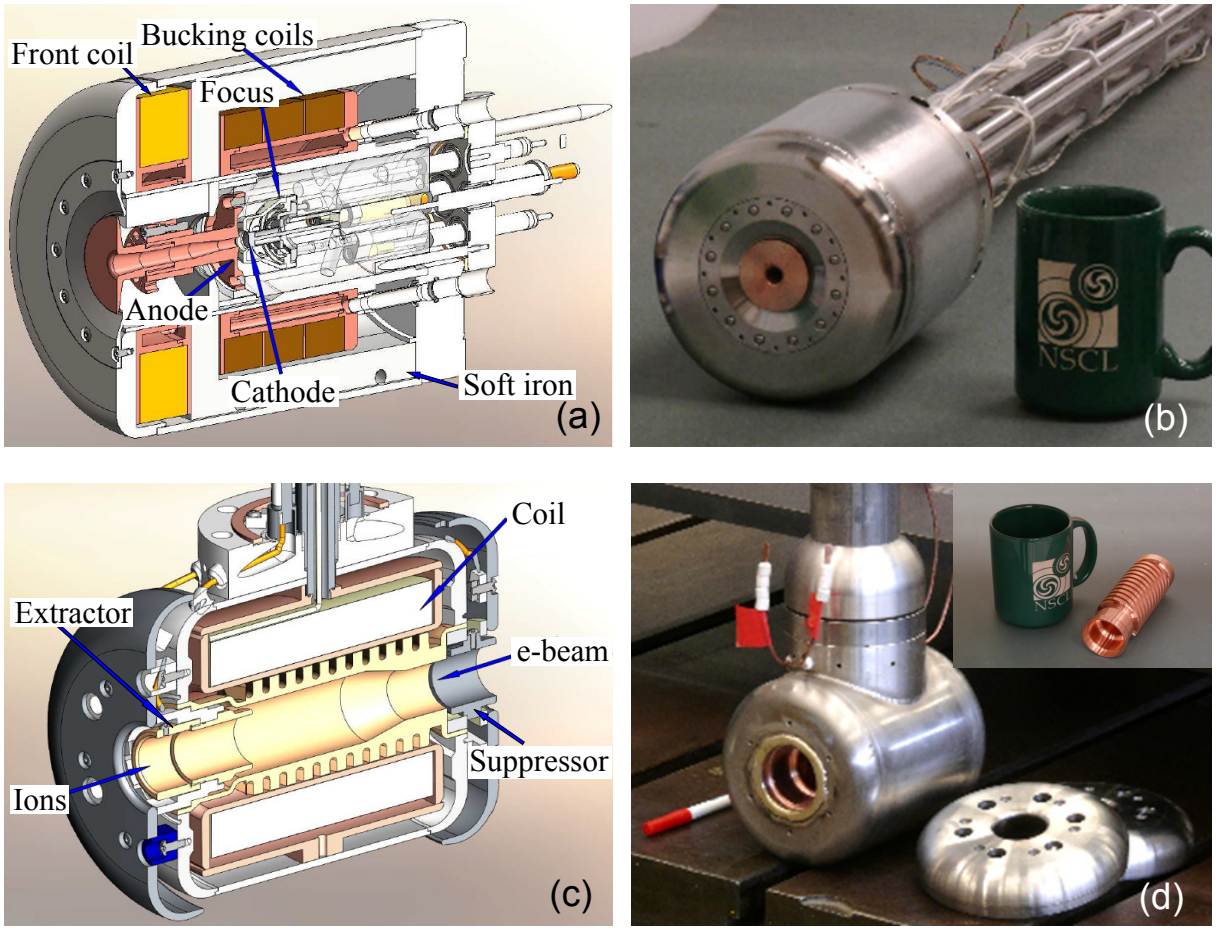

Figure 4.2 Side view cross sections of the electron gun (a) and the collector drawings (c) and the electron gun (b) and the collector assemblies (d).

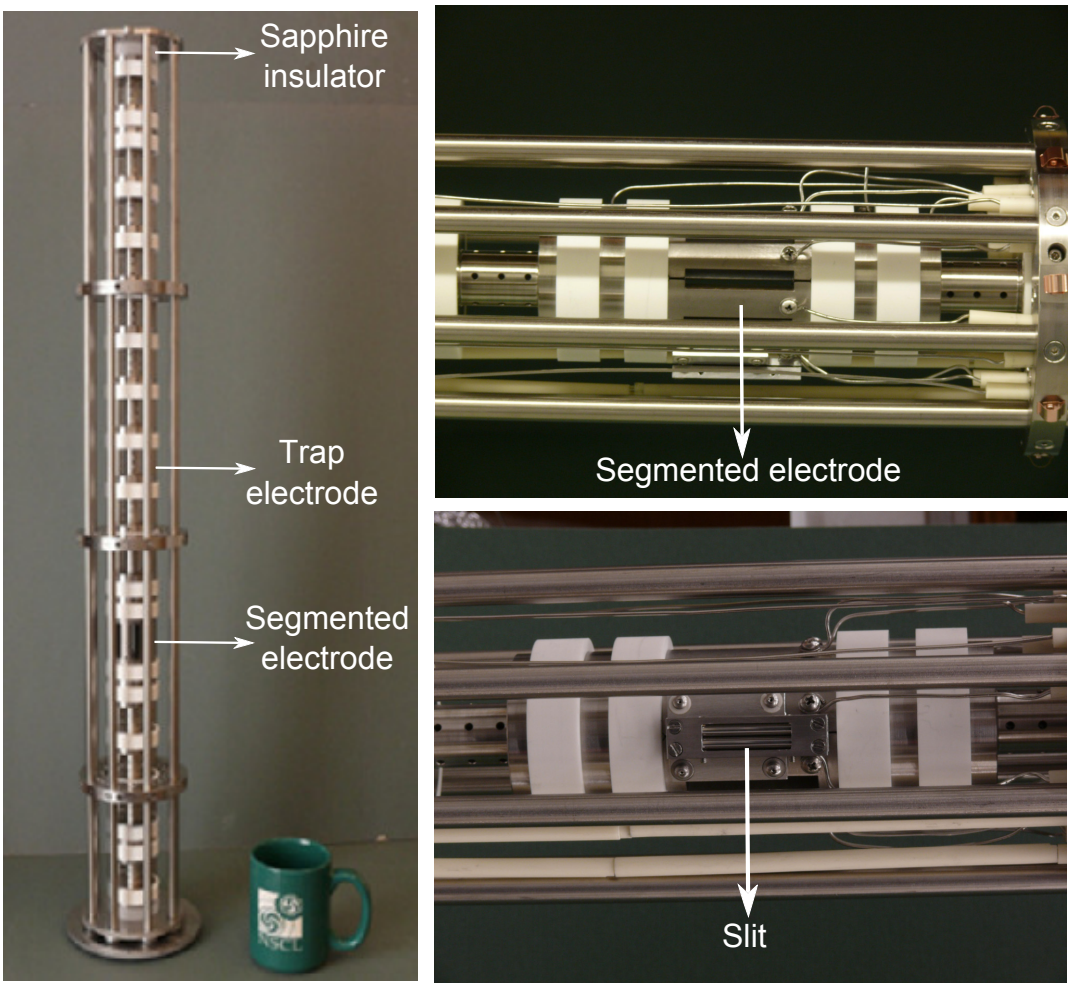

Figure 4.3 Trap electrode structure for the NSCL EBIT.

surrounding the collector electrode. Secondary electrons from the collision between the electron beam and the collector surface are suppressed by the suppressor electrode while the extractor electrode prevents electrons from traveling into the main beamline.

4.1.2 Trap electrode structure

As shown in Figure 4.3, the trap structure of the NSCL-EBIT consists of 25 electrodes. The electrodes are made of titanium because it is non-magnetic and has a low thermal conductivity. The trap size is 0.8 m in length and the overall trap, including support

structure, is around 1 m long. The sapphire insulators that are located between trap electrodes (not seen in the picture) and at both ends are used as 4 K thermal link to the trap structure. Segmented electrodes at the trap center allow radial access, for example, injecting a gas jet and x-ray spectroscopy. A small slit attached to the electrodes can be used for imaging the electron beam with an x-ray CCD camera.

4.1.3 Hybrid superconducting magnet

Figure 4.4 shows the complete assembly of the superconducting magnet, the electron gun, the collector, and the test ion source (a) and a section view(b). The section view displays the position of two different types of magnets: the Helmholtz coils and the solenoid. The Helmholtz coils generate a strong magnetic field in a small trapping region to shorten charge breeding time due to the high electron beam compression. The solenoid is not only designed for a large trapping region and storage capacity but also to provide a large acceptance for the EBIT. Since the magnets can independently produce magnetic fields up to 6 T, the EBIT can be operated with different magnetic field configurations and electron beam radii. The study of the capture probability independence of the different field configurations can be found in Chapter 5.5. Two "bucking" coils at both ends of the magnet support the electron beam transport from the electron gun to the collector.

4.2 Test ion source

For EBIT commissioning and off-line experiments, a test ion source is available. It is mounted about 2 m away from the EBIT on an independent beamline. A hot cathode ion source (Colutron model 100-Q) is used to provide a K^+ beam [55]. When a tungsten

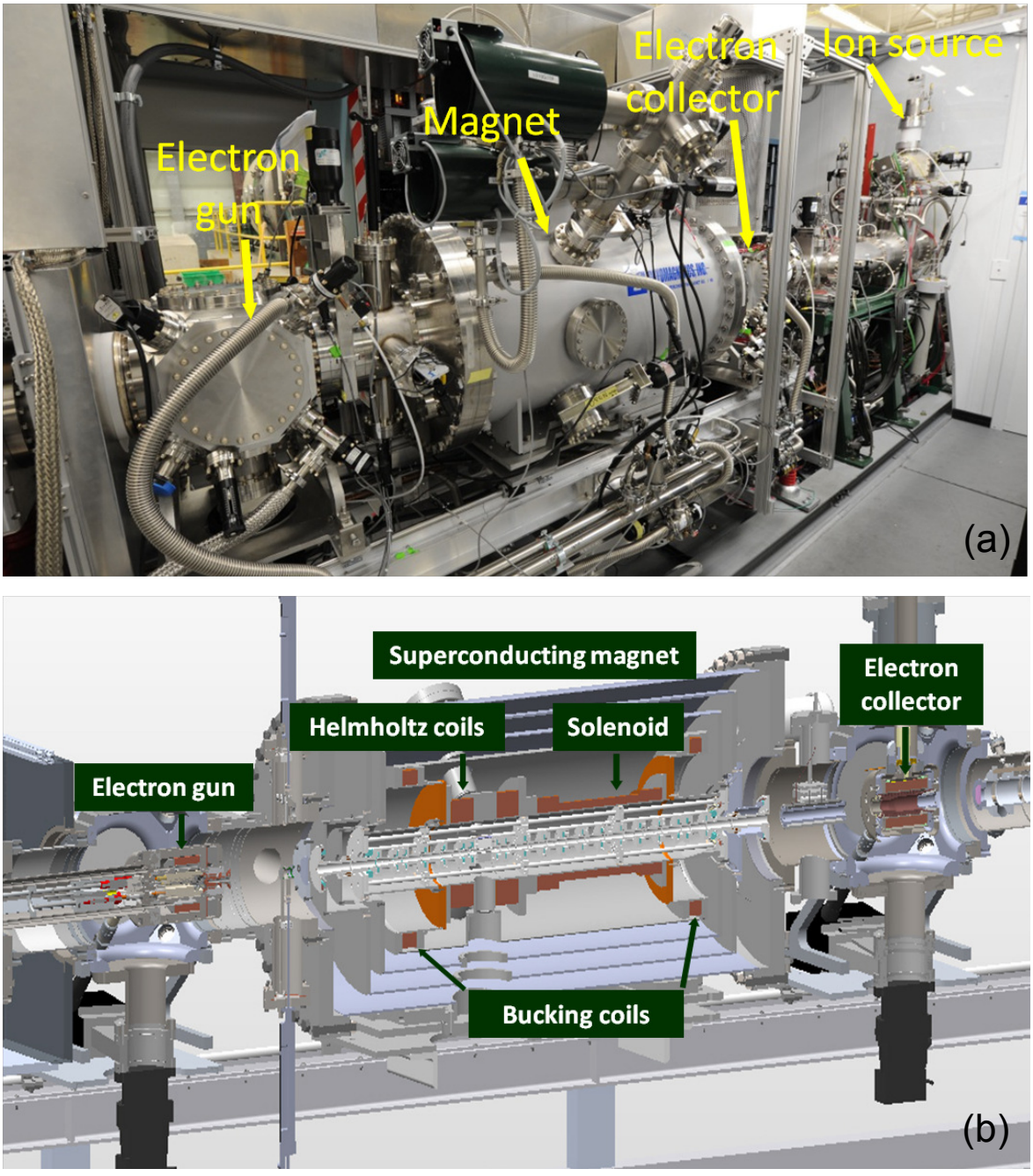

Figure 4.4 NSCL EBIT with the test ion source (a) and a side view cross section showing the combination of a solenoid and Helmholtz coils (b).

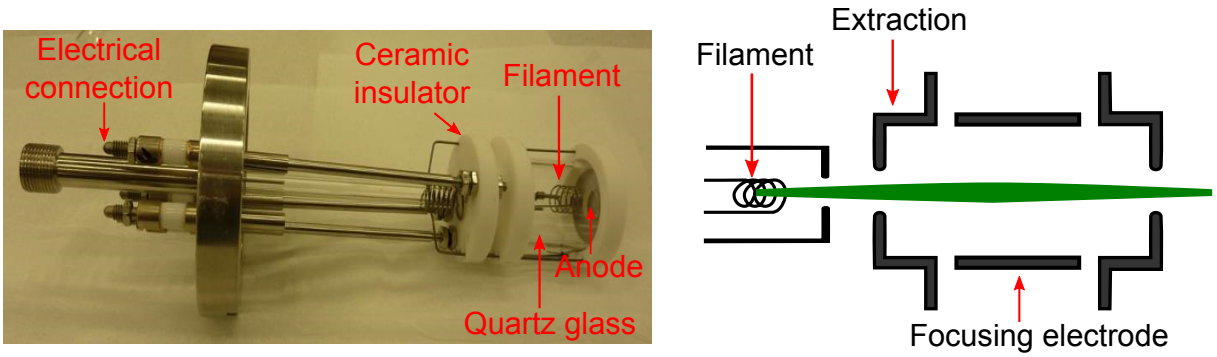

Figure 4.5 A hot cathode ion source (left) and a schematic corresponding to each component.

filament is heated, it ejects potassium ions through a surface ionization process [56]. Figure 4.5 displays the off-line ion source and its schematic. During the experiment, it was biased to 20 kV for producing a 20 keV ion beam. The used filament with a 20 mil diameter which was supplied with a voltage of 10.5 V and a 16 A current provided up to 2 nA during the tests. The anode was set to zero and the extraction was set at -5 kV.

4.3 Achromatic Q/A separator

The achromatic Q/A separator is designed to analyze and separate HCIs extracted from the EBIT. The Q/A acceptance of the separator is between 0.2 and 1 for a 12 keV/u ion beam energy. Within this range, it is enough to cover all isotopes available at the NSCL and FRIB. The separator mainly consists of two 45° electrostatic benders and a bending magnet as shown in Figure 4.6. Between the second electrostatic bender and the bending magnet, an adjustable horizontal slit is mounted to be able to cut the energy spread of the beam if desired. The energy dispersion calculated by first order optics is $(x, \delta_E) = 10$ mm/%. The calculated acceptance for the 12 keV/u ion beam is up to 120 π mm·mrad equivalent to a normalized emittance of 0.6 π mm·mrad [57].

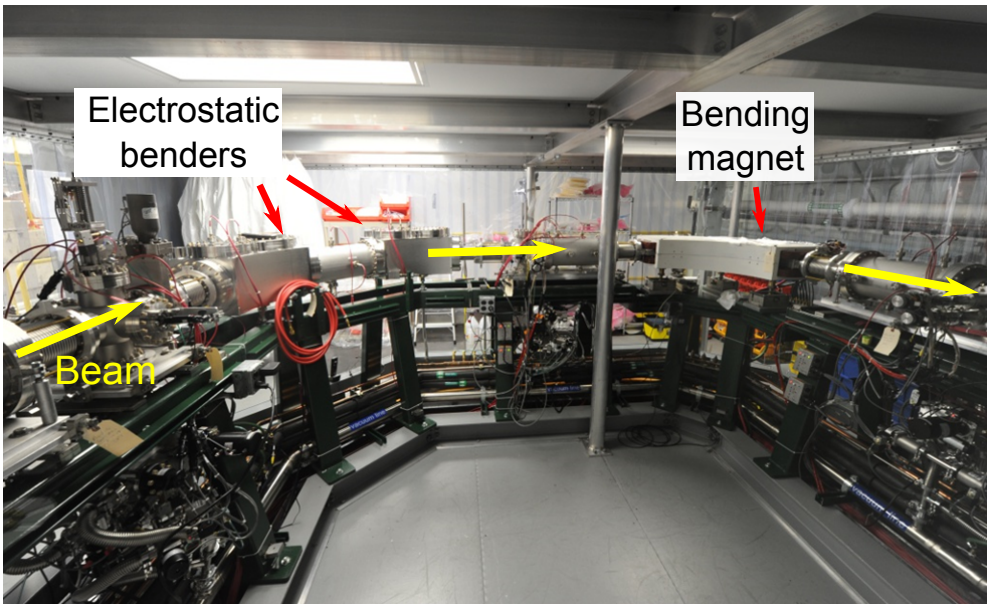

Figure 4.6 The Q/A separator consisting of two electrostatic benders and a bending magnet. The yellow arrow displays the direction of the beam extracted from the EBIT and transported to the linear accelerator.

4.4 Diagnostic devices

Based on the requirements to monitor the beam current in the range from 10 fA to 1 nA, to observe the beam image, and to measure the time-of-flight (TOF) of the ion beam, microchannel plates (MCPs) and Faraday cups (FCs) were chosen.

The MCP is a device used to detect charged particles and image the beam. It can also be used to measure a TOF signal when connected to an oscilloscope. Figure 4.7 displays the MCP mounted along the ReA beamline. The Faraday cup (FC) is a device that measures the beam current of charged particles in a vacuum system. It contains a measuring cup and an electron suppressor ring. In order to measure the beam current, the cup is inserted to obstruct the beam. A negative voltage is supplied to the suppressor electrode to prevent the escape of secondary electrons from the cup. By connecting the FC to Keithley high resolution ammeter [58], it is possible to precisely detect the ion beam to a range of 10 fA.

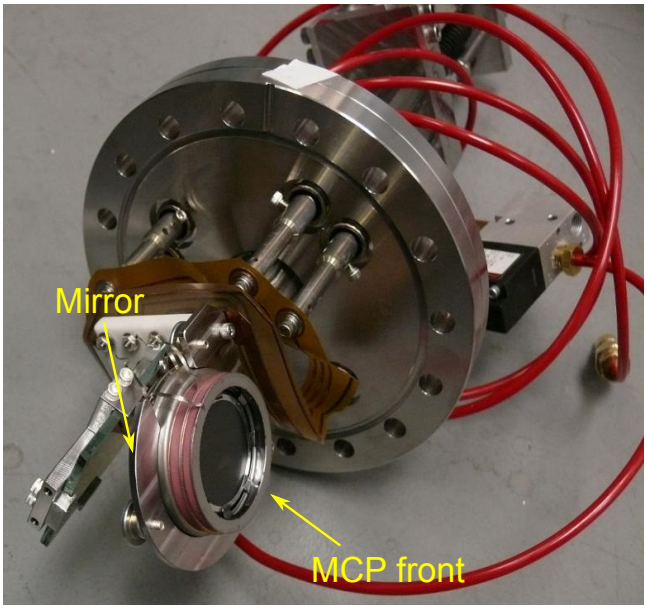

Figure 4.7 A picture of a microchannel plate installed in the ReA beamline.

4.5 Beamline transport optics

Along the beamline, several optical elements are installed to control the ion beams. Several electrostatic quadrupoles are used for ion transportation. For the NSCL EBIT charge breeder, two Einzel lenses are used: one next to the extraction electrode inside the ion source chamber and another inside the acceleration/deceleration column. A transfer lens is located between the electron collector and the trap entrance in order to focus the ion beam into the EBIT trapping region and help transport the electron beam to the collector. To correct the ion beam trajectory along the beamline, electrostatic steerers are employed. Figure 4.8 illustrates the quadrupole triplet and steerer electrodes, the fully assembled acceleration/deceleration column, and the transfer lens.

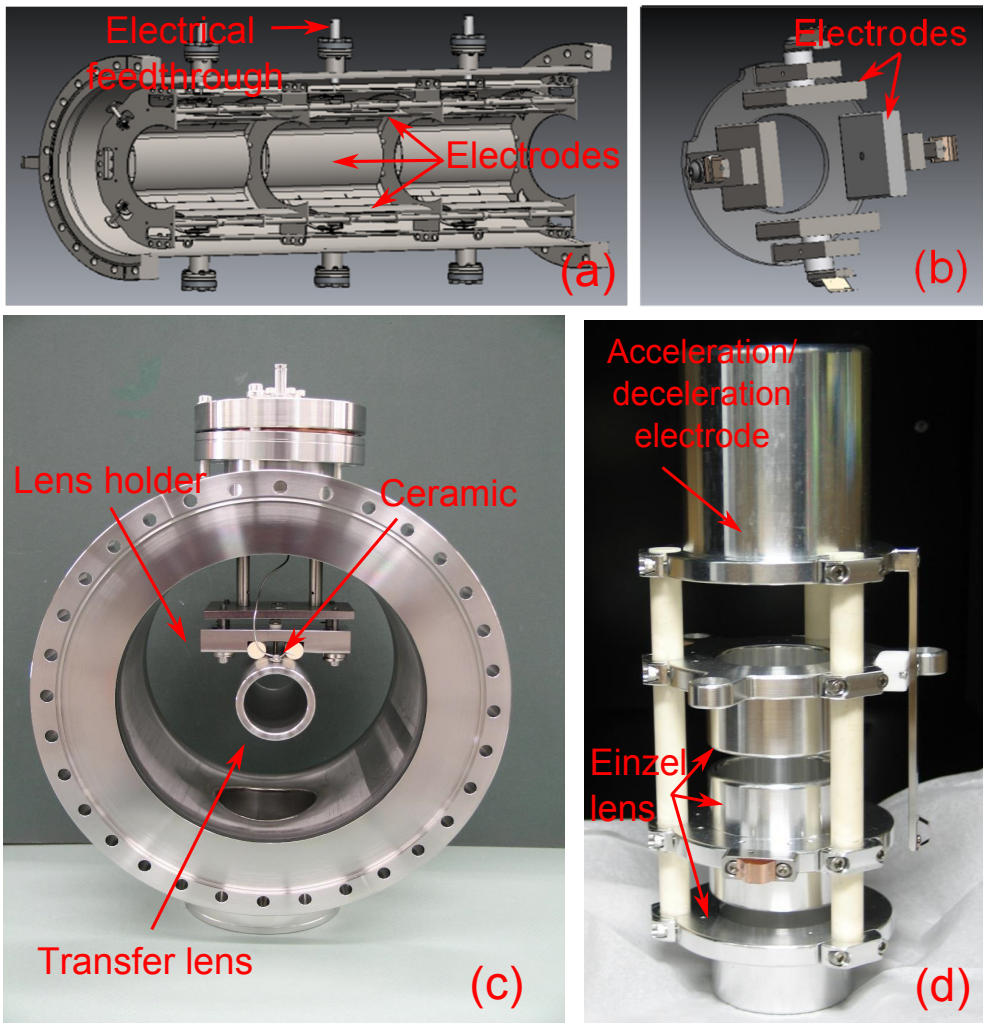

Figure 4.8 Drawing of a quadrupole triplet (a) and a steerer element (b), the transfer lens (c), and the fully assembled acceleration column consisting of an acceleration/deceleration electrode and an Einzel lens (d).

Chapter 5

Simulation of Ion Injection and Acceptance

Extensive simulations have been performed with the SIMION and "NEBIT" packages. Details of both will be discussed in the following sections. Section 5.1 explains the calculation of the electric and magnetic fields that are used in the simulations. Section 5.2 reports ion trajectory simulations that have been studied with SIMION to provide the optimum voltage settings for ion beam transport. Section 5.3 describes an in-house simulation code used to study capture efficiencies, called NEBIT. Results of NEBIT comparisons with a) an analytical formula, b) prediction by the Charge Breeding SIMulation (CBSIM) code, and c) an earlier version of NEBIT can be found in Section 5.4. Examples of capture efficiency simulations are discussed in Section 5.5.

5.1 Calculation of electric and magnetic fields

The electric field used in both simulations has been obtained by solving the Laplace equation for the entire EBIT electrostatic electrode system with SIMION. SIMION is a simulation package which calculates the electric field and trajectories of charged particles for a given configuration of electrodes [59]. Based on the design drawing of the EBIT a SIMION

electrode system, "workbench," was created in SIMION that includes a ground electrode, an acceleration/deceleration column, a collector, a transfer lens, and trap electrodes as depicted in Figure 5.1a. The instance starts at the location equivalent to the center of the BOB 1, see Figure 4.1. To avoid a large file size, the SIMION workbench is divided into two instances: a collector part and a trap part. The collector part starts at the ground electrode and extends to the center of the transfer lens and the other half includes all trap electrodes. After assigning voltages to the electrodes, the potential distribution and the electric field are calculated. Figures 5.1b and 5.1c illustrate the potential and electric field maps when the electrodes are set for the injection of a 60 keV ion beam. The electric field is highest at the transition between the ground electrode and the high voltage platform. For the acceptance simulation, the electric field map files from SIMION are imported into the NEBIT code.

The NSCL EBIT consists of five groups of magnets: a solenoid, a pair of Helmholtz coils, two bucking coils, and a collector coil [60]. The magnetic field used in both SIMION and NEBIT is obtained from an analytical solution for the superposition of the magnetic fields calculated for each magnet. With the approximation at small radii, the axial magnetic field component is equivalent to the on-axis one and the radial magnetic field component is proportional to the derivative of the on-axis magnetic field component. Unless specified otherwise, the magnetic field configuration used in the simulation are 1T (solenoid) -6T (Helmholtz coils) and 6T-6T. These magnetic field distributions are illustrated in Figure 5.2. The magnetic field of 1 Tesla is arbitrarily selected to provide a large electron beam size and 6 Tesla is the highest field strength the NSCL-EBIT can produce. The sketch on top of the figure indicates the position of each coil. At the center of the collector, the magnetic

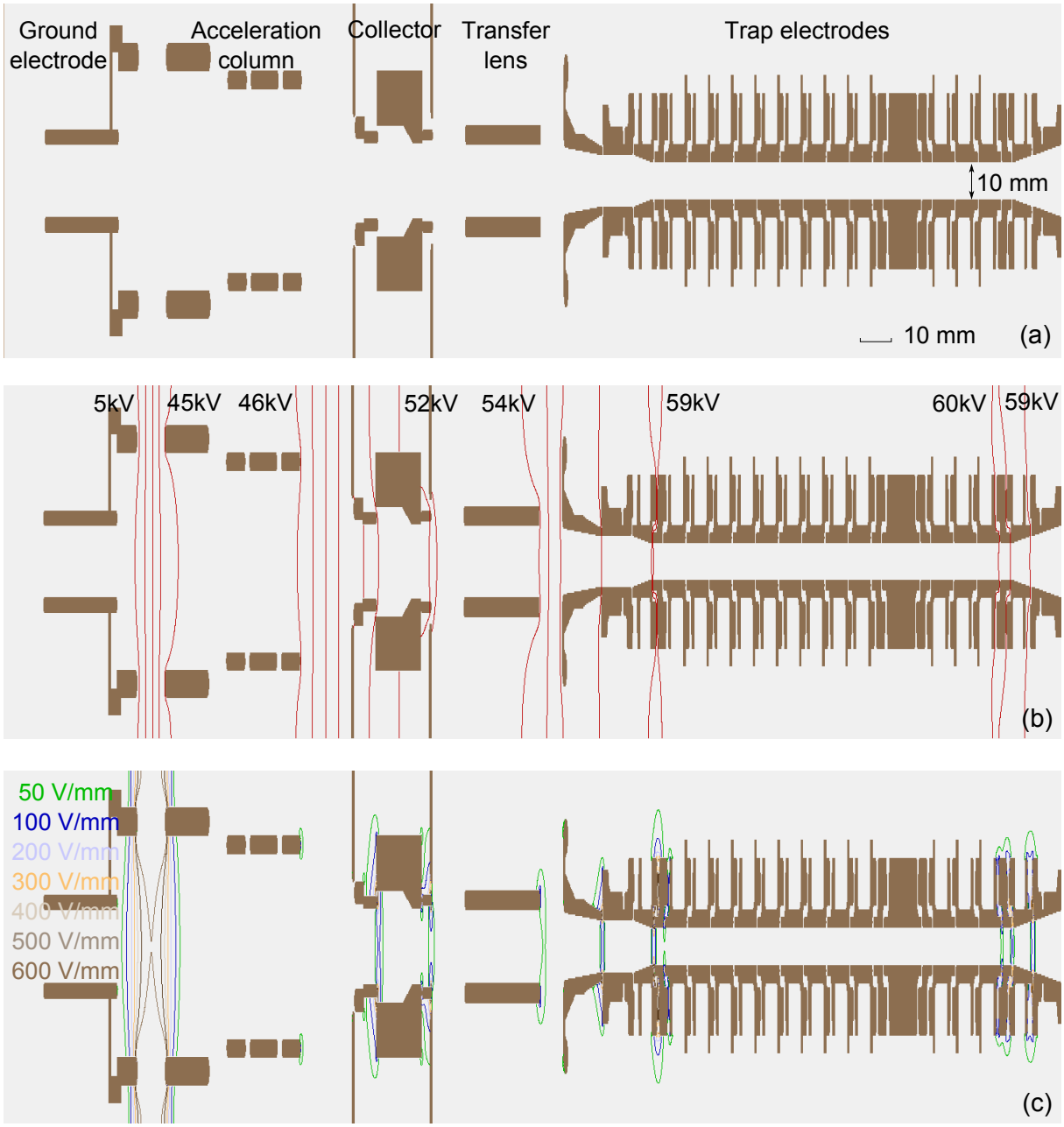

Figure 5.1 EBIT workbench in SIMION containing a ground electrode, an acceleration/deceleration column, a collector, a transfer lens, and trap electrodes (a), potential (b) and electric field map (c) solved by SIMION.

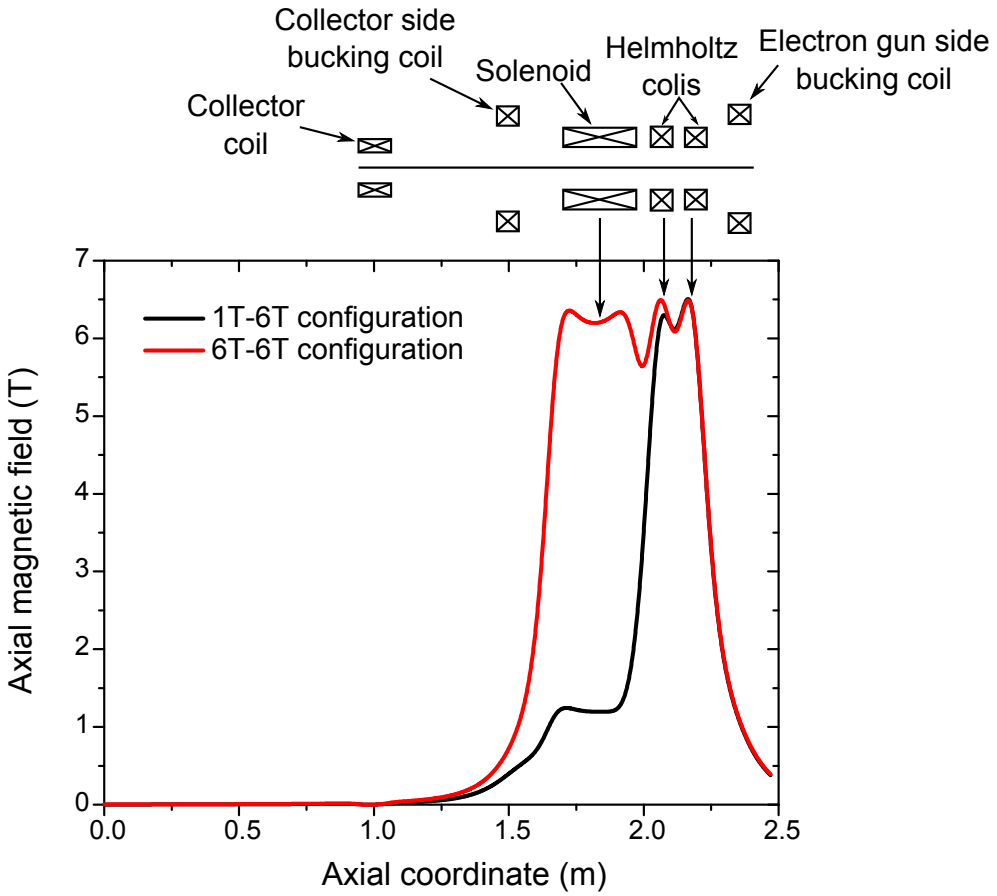

Figure 5.2 Magnetic field distribution of 1T-6T (black) and 6T-6T (red) used throughout the calculations. The trap center is at $z = 2.12$ m.

field is minimized by the field from the collector coil. For the ion trajectory simulations within SIMION, the magnetic field is separately calculated and saved as a file which can be imported by SIMION. In NEBIT, the magnetic field is calculated from a routine describing a superposition of thin coils.

5.2 Ion trajectory simulation by SIMION

SIMION was used to simulate the ion trajectories to understand the ion beam's behavior. It provided optimum voltage settings for minimizing the ions' radial energy pickup. The larger the radial energy, the less the ions overlap with the electron beam.

To simulate the ion trajectories a singly charged ion beam of 60 keV and 10 π mm·mrad was used. The beam started at the beginning of the ground electrode and traveled toward the trap. Assuming that the electrons are uniformly distributed over the electron beam cross section, the space-charge potential, Eq. 2.3, was calculated and added into SIMION via a user program.

Illustrated in Figure 5.3, the ion beam trajectories in the 1 T and 6 T magnetic fields are compared without (a, c) and with (b, d) the 2 A and 12.5 keV electron beam. The location of the outer barrier is indicated in Figure 5.3a. Without the electron beam, the ion beams are focused by electric and magnetic fields at the trap entrance and a helical motion is observed which results from existence of the high magnetic field. The ions are retarded at the outer barrier and pick up radial energy when crossing magnetic field line. Without proper injection, most of the ions having high radial energy tend to hit the surrounding electrodes at this location. The ions traveling into the 6 T magnetic field have higher cyclotron frequency than those of the 1 T magnetic field. When the electron beam is switched on, the ion beam radius becomes smaller due to the radial space-charge field. The effect of space-charge to the ion trajectories starts when the ions pass the collector.

Figure 5.4 displays a contour plot for the initial phase space of the radial energy that the ions gain during the transport into the EBIT. The results were recorded at the location where the magnetic field is produced mainly by the solenoid. The ions flying into the 1 T magnetic field gain less energy than those into the 6 T magnetic field. Ions injected with small transverse velocity or off-axis distance gain less radial energy than those with large transverse velocity or off-axis distance. The highest radial energy that the ions in a beam with 15 π mm·mrad emittance can gain are 9 and 90 eV for the 1 T and the 6 T magnetic

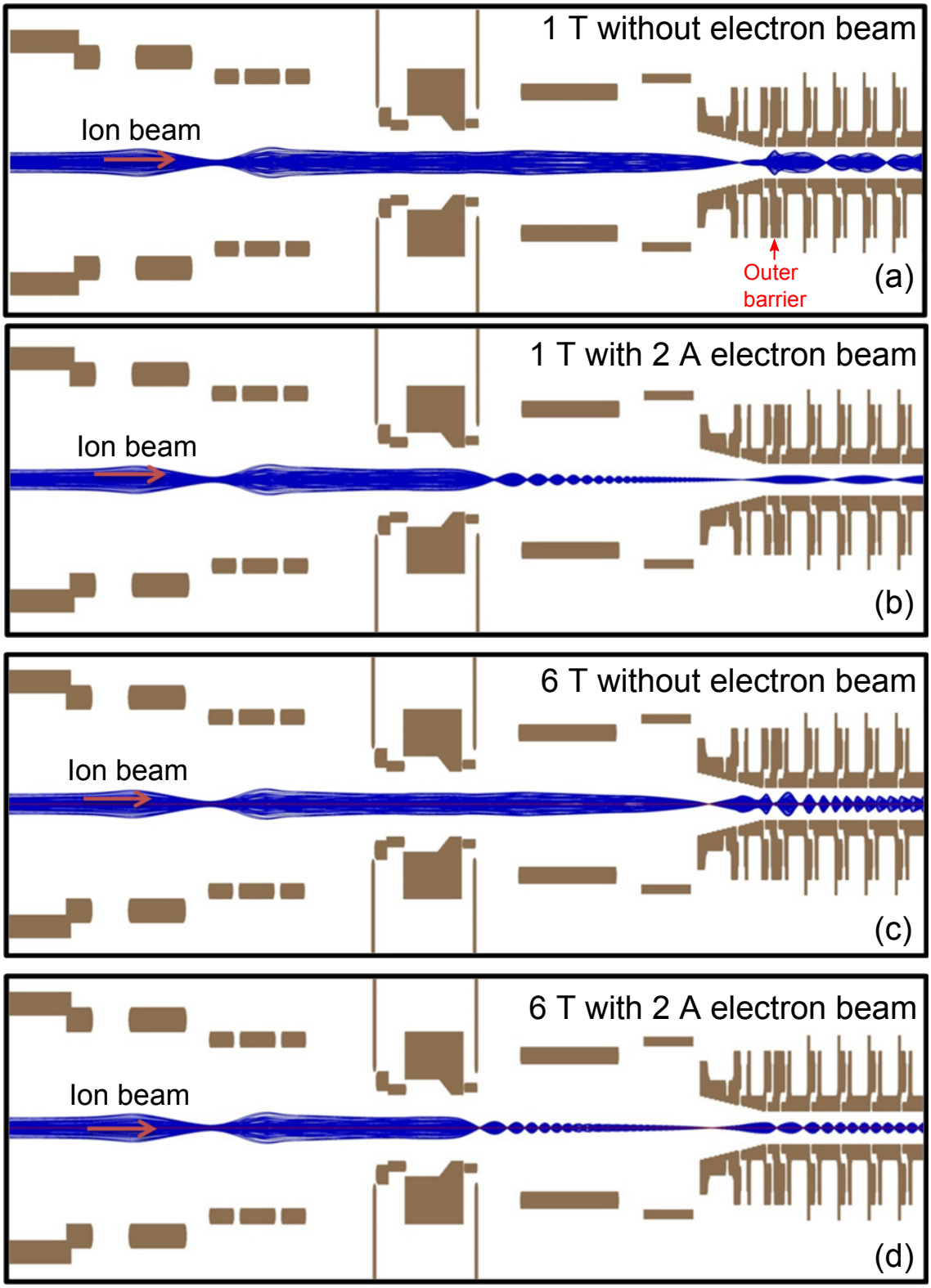

Figure 5.3 Comparison of ion trajectories in the 1 T magnetic field without (a) and with a 2 A electron beam (b) and the 6 T magnetic field without (c) and with a 2 A electron beam (d). A 60 keV beam of injected ions and an electron beam energy of 12.5 keV were used.

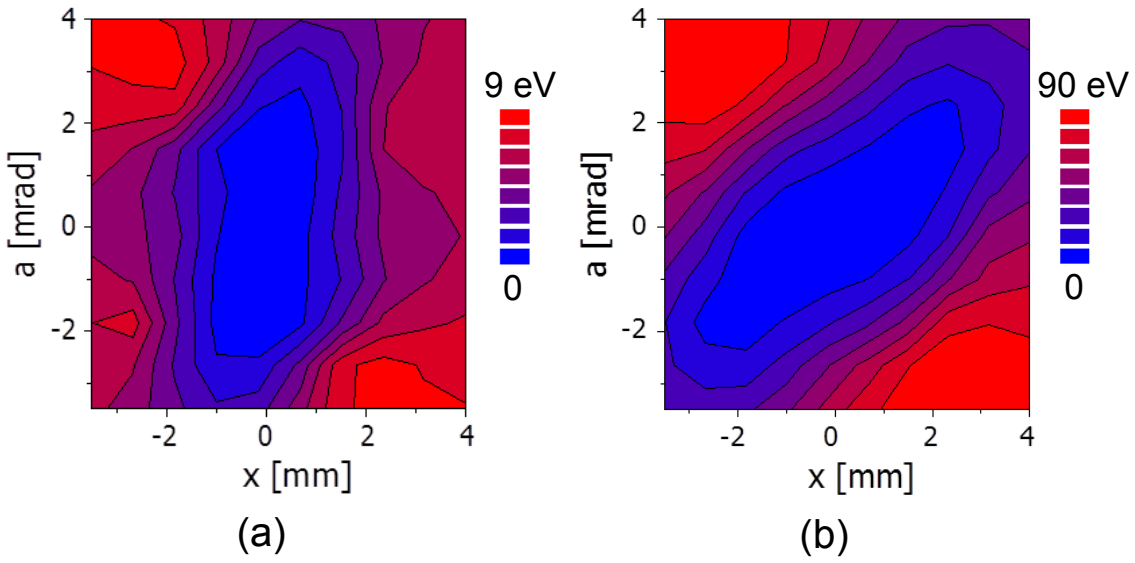

Figure 5.4 Contour plot of radial energy that the ions gain while traveling into the 1 T (a) and the 6 T (b) magnetic fields. The radial energy is plotted as a function of the initial phase space.

fields, respectively. The contour plot also indicates the proper orientation of the injected ion beam in the phase space.

It was found from the simulation that the beam focusing is most sensitive to the changes of voltages at the acceleration/deceleration electrode and the Einzel lens rather than the transfer lens. The optimization of a voltage setting was achieved by adjusting the voltage applied to each electrode and tracking the ion beam radius inside the trapping region. The number of ions lost to the electrode had to be minimized.

5.3 NSCL EBIT simulation code

The NSCL EBIT simulation code (NEBIT) was originally created by E. Gavartin [61], based on the "IonCool" package [62], to calculate the NSCL EBIT's acceptance and capture efficiency. The acceptance was evaluated based on an EBIT geometry primarily consisting of the collector, barriers, and trap electrodes. The magnet structures providing two different

Feature	Earlier NEBIT	Current NEBIT
Electric potential	Linear approximation	Solving Laplace equation by SIMION
Space charge potential	No energy correction	With energy correction
Electrode structure	Simple structure	Real design structure
Monte-Carlo approach	EI process	EI process, initial sample selection

Table 5.1 Comparison of features used in the earlier and the current versions of NEBIT.

magnetic field configurations were determined based on the EBIT geometry. The potential was defined by voltages applied to electrodes and linearly interpolated at the drift space. The radial electric field from electrodes was neglected. The space-charge was simply calculated from Eq. 2.3 and the electric field was calculated by the two-point backward-difference formula [39].

During this thesis work, NEBIT was developed further by using the detailed NSCL EBIT geometry which also contains the ground electrode, the acceleration/deceleration electrode, the Einzel lens, and the transfer lens, see Figure 5.1. The magnetic field distribution is calculated based on the existing magnet design. The potential and electric field are obtained by solving the Laplace equation with SIMION and all electric field components are taken into account. The space-charge potential is calculated using the corrected electron beam energy by implementing Eq. 2.8. A Monte-Carlo approach is used to determine the EBIT acceptance and the ionization probability for the EI process. Table 5.1 summarizes main features used in the earlier and the improved versions of NEBIT. The details of the current version of NEBIT are described in the following.

The simulation algorithm describing how NEBIT calculates the acceptance of the EBIT is shown in Figure 5.5. EBIT parameters and configurations containing an electric field, a magnetic field, and space-charge potential are set at the beginning. Monte-Carlo sampling is performed within the given phase space at first and the ion beam properties of mass,

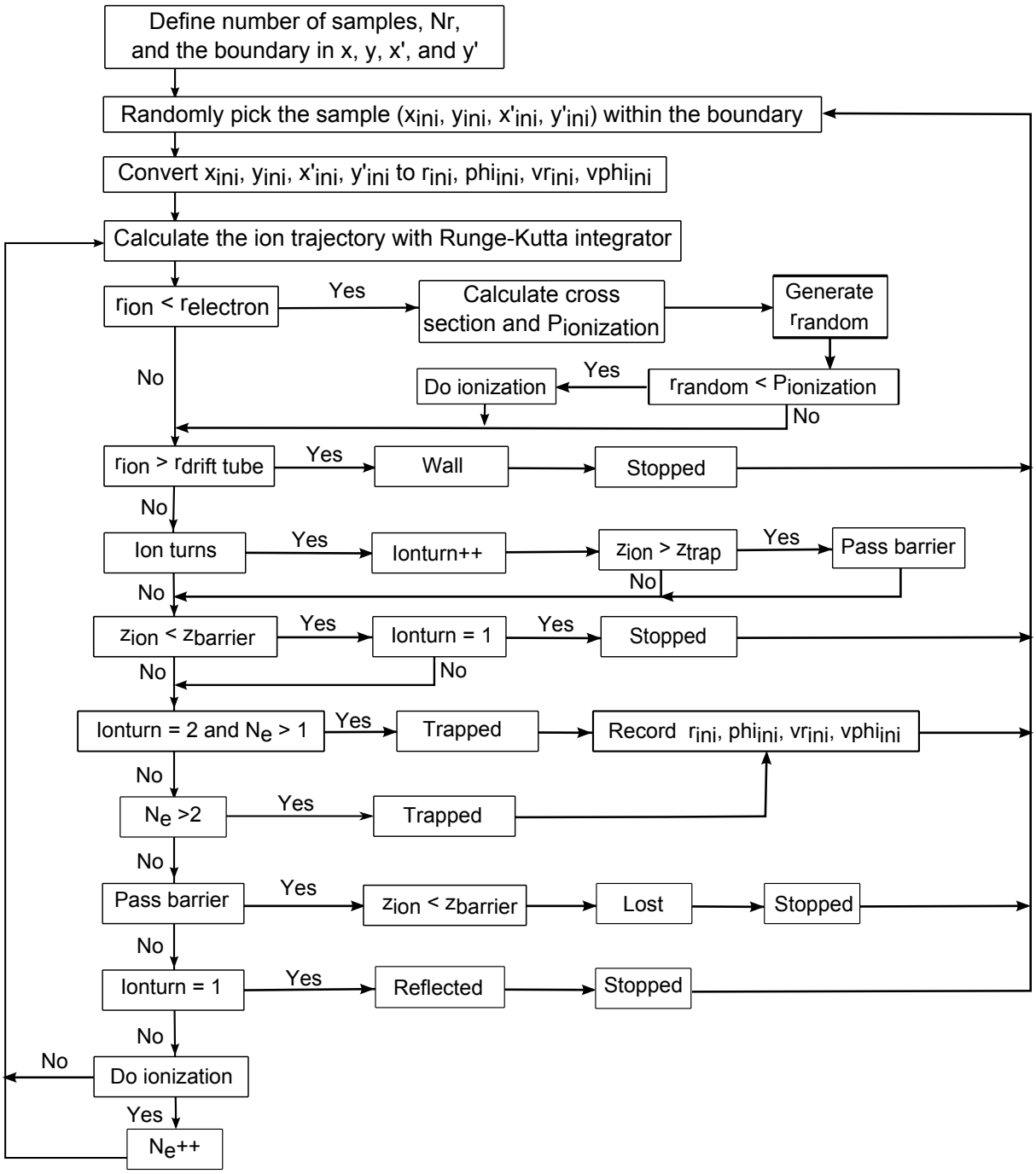

Figure 5.5 Flowchart showing the algorithm of the acceptance calculation.

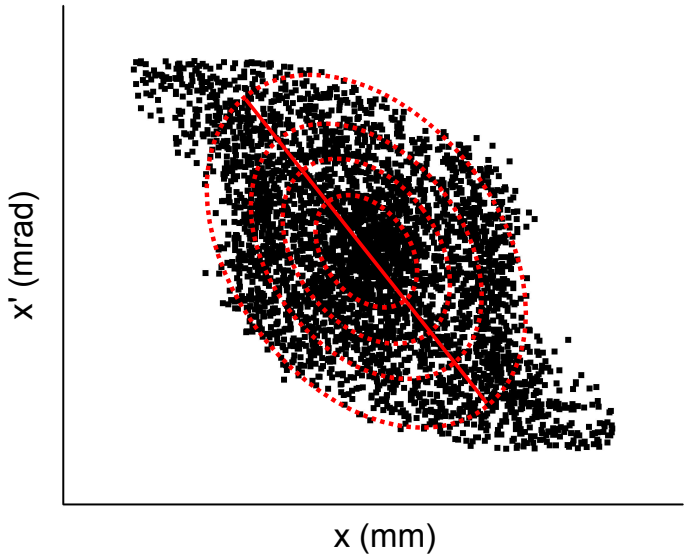

Figure 5.6 Concept of simulated capture efficiency. The ratio of the number of the trapped to the injected ions in the same phase space area is interpreted as a capture probability. The ellipse is aligned along the line from the linear fit (red solid line).

atomic number, and axial energy are initially established. A Runge-Kutta integrator [63] is used to calculate the ion trajectories since it well solves the ordinary differential equations of motion. Ionization process is considered if the trajectory is inside the electron beam. The ions are trapped if they change direction twice and the charge state is greater than 1+ or the charge state turns to 3+ at any location in the trap. The NEBIT output are the initial positions and angles of the trapped ions and this collection forms the acceptance phase space of the EBIT. A single ion calculation stops if the trajectory ends up at an electrode or if the ion leaves the trap.

To acquire the capture efficiency as a function of beam emittance, a separate code is used. The code initially loads the beam parameters and the acceptance phase space which is outputted from NEBIT. The acceptance phase space ($x - x'$ and $y - y'$) is fitted with

linear and elliptic equations to provide an ellipse orientation and Twiss parameters (α, β, γ). The capture efficiency is computed from the overlap in phase space of the beam emittance and the acceptance of the EBIT. The concept of capture efficiency is illustrated in Figure 5.6. With the total number of ions N which are sampled in the defined phase space area, $s = x \cdot x'$, a number of particles per unit phase space area N/s is calculated. A capture efficiency ϵ_{cap} is given by

$$\epsilon_{\text{cap}} = \frac{n_i}{\epsilon_i \cdot N/s} \tag{5.1}$$

where n_i is the number of particles inside the ellipse corresponding to emittance ϵ_i. By varying the beam emittance and keep Twiss parameters to be the same, the capture efficiency is obtained as a function of the injected beam emittance. The statistical error of the capture efficiency is calculated from the relative uncertainty, $1/\sqrt{n_i}$.

5.4 NSCL EBIT code benchmarking

It is crucial to ensure that the simulation code works correctly and provides results consistent with those from other reliable software. In order to benchmark the code, the following test and comparisons were performed:

1. Test of energy conservation along the ion trajectory
2. Comparison of geometrical acceptance from NEBIT and an analytical formula
3. Comparison of capture efficiency from NEBIT and an analytical formula
4. Comparison of charge evolution from NEBIT and CBSIM
5. Comparison of capture efficiency between current and earlier versions

Parameter	Value
Atomic number	26
Atomic mass (amu)	56
Electron beam energy (keV)	12.5
Electron current (A)	1, 2.5
Axial energy (keV)	60
Cathode radius (mm)	3.175, 6.35
Magnetic field at cathode (G)	10
Cathode temperature (K)	1400

Table 5.2 EBIT and ion beam parameters used in SIMION and NEBIT unless otherwise specified.

5.4.1 Test of energy conservation along the ion trajectory

It is important that the NEBIT code handles forces correctly. Total energy conservation is calculated to provide a test of numerical issues. The potential energy is obtained from SIMION and the kinetic energy are numerically calculated. Computed from the space-charge potential with energy correction, the complex formula for the electric field comprises several terms which possibly cause mistakes during the code construction. By checking the conservation of the total energy, it is helpful to find out whether the implementation of space-charge is correct or not.

The settings for the calculation can be found in Table B.1 of the appendix. The trap potential is extended up to the TE4 electrode, see Figure B.1. The EBIT and ion beam parameters are obtained from Table 5.2. The cathode radii for the electron beam current of 1 A and 2.5 A are 3.175 mm and 6.35 mm, respectively. An ion with 60 keV is injected both on- and off-axes. The off-axis calculation helps investigate how much the radial component contributes to the total energy.

Figure 5.7 illustrates the error of the total energy for on- and off-axis calculations (a) and the potential, kinetic, and total energy (b). For the off-axis calculations with 1 A and 2.5 A

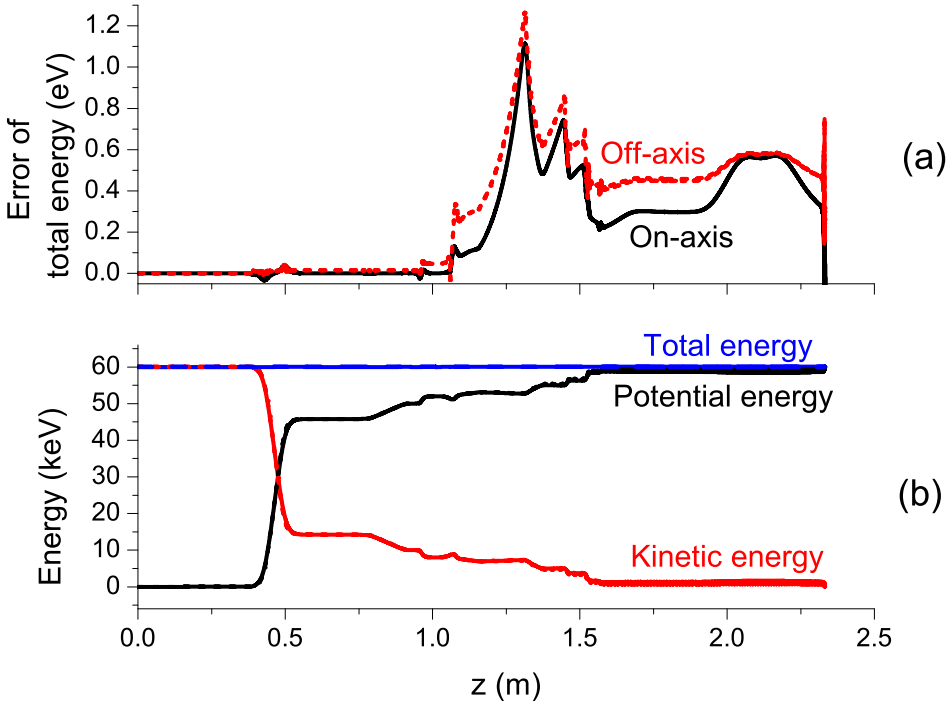

Figure 5.7 The error of the total energy from on- (black) and off-axis (red) injections (a) and kinetic, potential, and total energy (b). The ion is injected with an offset of $x = 2.31$ mm, $y = 0.12$ mm, $a_x = -31.39$ mrad, $a_y = -2.62$ mrad.

electron beam currents, the initial positions and angles in the phase space of horizontal and vertical axes are shown in Figure 5.8. A test ion with extreme initial conditions is chosen where numerical errors can contribute most. The maximum errors of the calculated from the initial total energy are shown in Table 5.3. We can see that the error increases with the electron beam current and the maximum error is independent of the position in the phase space where the ion is injected. Even though, the error in Figure 5.9 is 25 eV for 2.5 A electron beam current, the relative error when compared to space-charge potential is less than 1%.

It is obviously shown that the error starts to appear after ion passes the collector and results from integrated numerical error during the calculation of axial space-charge electric field. Within this range of the negligible errors of the total energy, the calculation performed

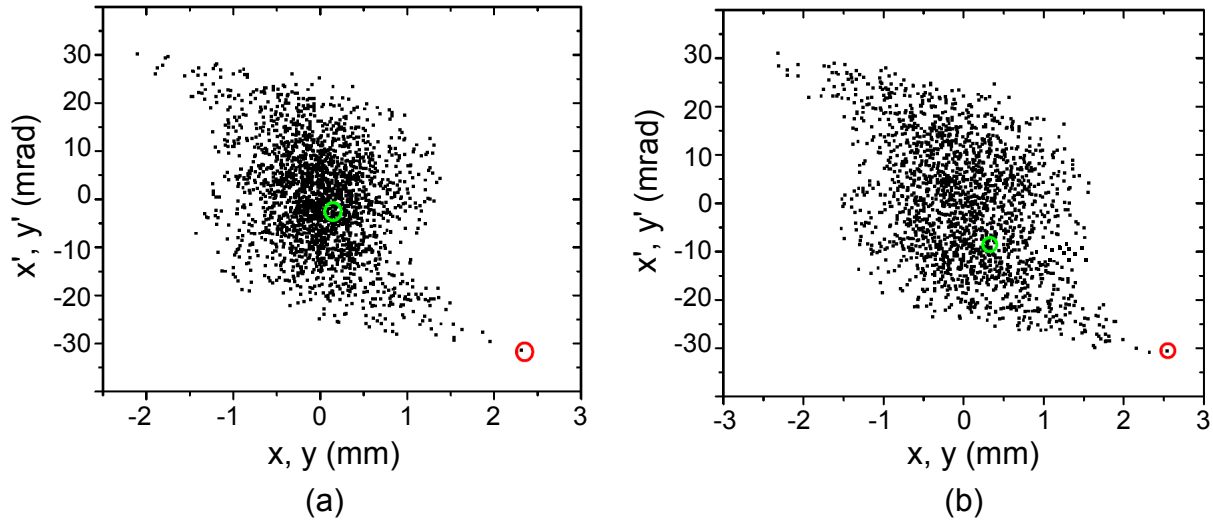

Figure 5.8 Acceptance phase space in x direction calculated for 1 A (a) and 2.5 A (b) electron beam currents and a 1T-6T magnetic field configuration. The initial position and angle in x (red) and y (green) directions are given in circles.

Calculation	Error (eV)	
	$I_e = 1$ A	$I_e = 2.5$ A
on-axis	1.1	25
off-axis	1.3	24

Table 5.3 Maximum errors of the total energy. The calculations were performed with the electron beam currents of 1 A and 2.5 A and the test ion was injected both on- and off-axes.

by NEBIT shows the behavior of conservation of energy. It confirms that the code is good enough for the acceptance calculation.

5.4.2 Comparison of geometrical acceptance from NEBIT and an analytical formula

The geometrical acceptance, Eq. 3.9, determines the maximum emittance of an ion beam that can be filled into the electron beam. With the real NSCL EBIT structure, the geometrical acceptance calculated by NEBIT is compared against the predicted value from

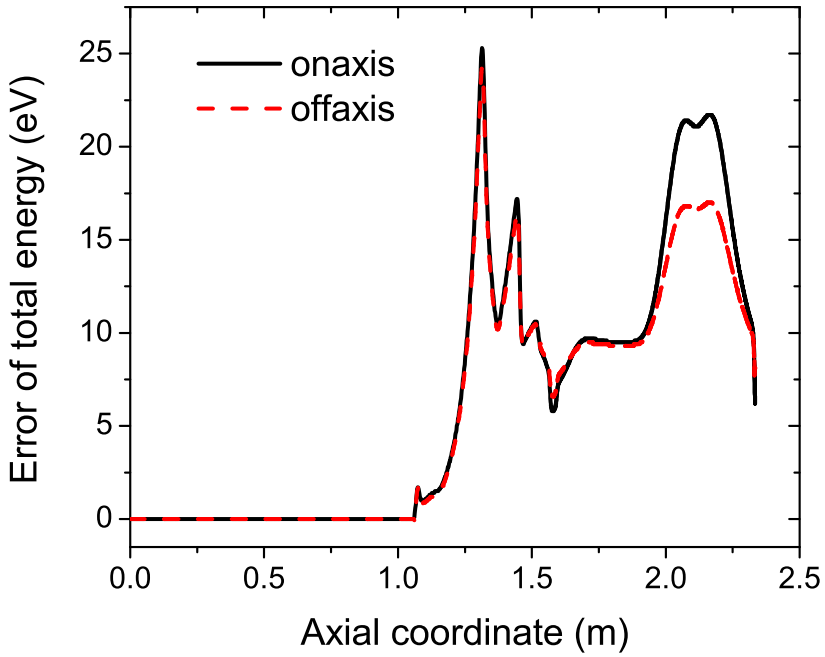

Figure 5.9 The error of total energy calculated from on- (black) and off-axis (red) ion injections with the electron beam current of 2.5 A.

Parameter	Value
Atomic number	26
Atomic mass (amu)	56
Monte-Carlo sample	200,000
Kinetic energy (keV)	60
Electron energy (keV)	12.5
Electron current (A)	0.1, 1
Cathode radius (mm)	3.175
Magnetic field at cathode (G)	10
Cathode temperature (K)	1400

(a)

Parameters		1T-6T (1T)	1T-6T (6T)	6T-6T
0.1 A	x_{min}, x_{max} (mm)	-0.35, 0.35	-0.25, 0.25	-0.3, 0.3
	x'_{min}, x'_{max} (mrad)	-8.5, 8.5	-5.5, 5.5	-6, 6
1.0 A	x_{min}, x_{max} (mm)	-0.7, 0.7	-0.4, 0.4	-0.4, 0.4
	x'_{min}, x'_{max} (mrad)	-20, 20	-12, 12	-11.5, 11.5

(b)

Table 5.4 Beam and EBIT parameters for the NEBIT calculations (a) and sample phase space of 0.1 A and 1 A electron beam currents for 1 T and 6 T regions of the 1T-6T magnetic field configuration and the 6T-6T configuration (b). The number in the parenthesis indicates the region of the magnetic field used for the evaluation of the acceptance.

the analytical formula. The 1T-6T magnetic field configuration is divided into two regions of constant magnetic field. An injected ion is considered to be trapped if its trajectory is completely inside the electron beam. On the other hand, the injected ion is lost if the radius of its trajectory is larger than the drift tube radius, the ion returns, or the axial coordinate of the ion travels beyond the 1 T or 6 T region.

The voltages applied to each electrode can be found in Table B.2. Once the electron beam current changes from 0.1 A to 1.0 A, the voltage setting has to be re-optimized to accommodate the beam into the trap, especially at the trap entrance. The EBIT and the beam parameters used in these calculations are listed in Table 5.4.

Figure 5.10 shows the acceptance phase space calculated from the NEBIT code using

Electron beam current (A)	Magnetic field configuration	Interested region	Acceptance (π mm·mrad)		Deviation (%)
			NEBIT	Geometrical	
0.1	1T-6T	1T	1.48	1.57	-5.7
	1T-6T	6T	0.66	0.72	-8.3
	6T-6T	-	0.65	0.72	-9.7
1.0	1T-6T	1T	5.45	5.33	2.2
	1T-6T	6T	2.14	2.21	-3.6
	6T-6T	-	2.20	2.22	-0.9

Table 5.5 Comparison of geometrical acceptance calculated with the analytical formula and NEBIT.

electron beam currents of 0.1 A (a, b, c) and 1 A (d, e, f), respectively. The red ellipses represent the calculated acceptance from the NEBIT code. The rotations of the acceptance phase space show the injected beam characteristics whose trajectories are entirely inside the electron beam. The acceptance indicated by areas within the red ellipses are compared with the predicted values and shown in Table 5.5. From the table we can see that the largest deviation is -9.7 % from the calculation of 0.1 A electron beam current at 6 T region of the 1T-6T configuration. Overall, a good agreement between the two methods is observed.

5.4.3 Comparison of capture efficiency calculated with NEBIT and an analytical formula

Combining the geometrical acceptance α from Eq. 3.9 with the ionization probability from Eq. 2.15, one can estimate the capture probability of the EBIT. The cross section of going from a 1+ to a 2+ charge state is obtained from Lotz's semi-empirical formula with the given element, see Section 2.4. To acquire the ionization probability, the time the ion spends inside the electron beam is computed from the ion mean energy in the trap and the trap

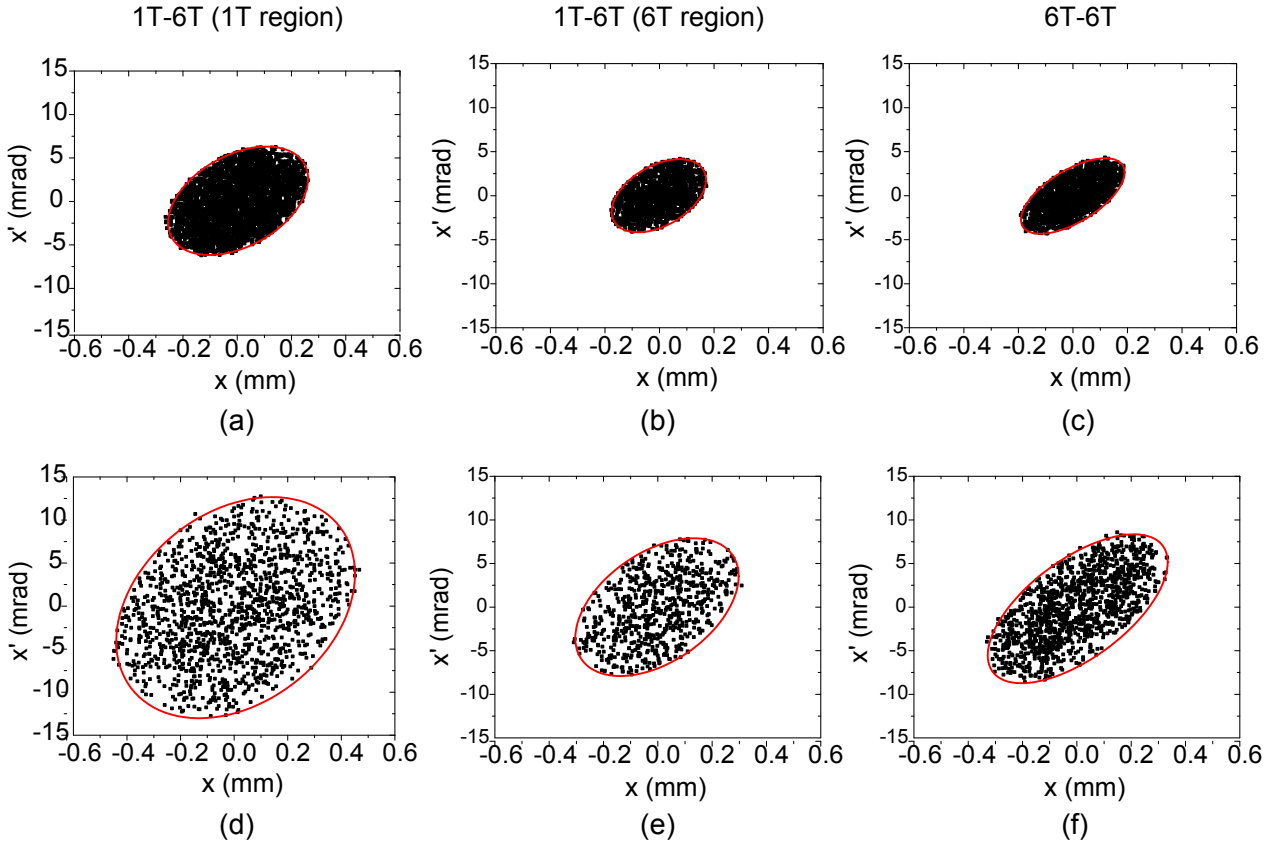

Figure 5.10 The acceptance phase space determined in the 1 T region (a, d) and the 6 T region (b, e) of the 1T-6T magnetic field configuration and the 6T-6T configuration (c, f) with 0.1 A (a, b, c) and 1 A (d, e, f) electron beam currents.

Input parameters	Value	Unit
Electron beam current	1	A
Magnetic field	6	T
Electron beam energy	12.5	keV
Trap length	0.75	m
Ion mean energy in trap	1	keV
Ion extraction energy	60	keV
Atomic mass	56	amu

Output parameters	Value	Unit
Electron beam current density	1.46×10^4	A/cm^2
Time required for $1+ \rightarrow 2+$	1×10^{-6}	s
EI cross section	1×10^{17}	cm^2
Ion mean velocity	8.3×10^4	m/s
Ion-electron overlap time	9×10^{-6}	s
Ionization probability	1	
Geometrical acceptance	2.34	π mm·mrad

Table 5.6 List of input (top) and output parameters, and geometrical acceptance (bottom).

length. The capture efficiency ϵ_{cap} is given by

$$\epsilon_{\text{cap}} = \begin{cases} \frac{\text{Emittance}}{\alpha} \times \text{Ionization probability (\%)} & \text{Emittance} > \alpha \\ \text{Ionization probability (\%)} & \text{Emittance} < \alpha. \end{cases} \tag{5.2}$$

Table 5.6 shows the input and output parameters, and the calculated geometrical acceptance. Depicted in Figure 5.11, the capture efficiency as a function of the beam emittance are calculated from both the analytical formula and NEBIT where the 6T-6T magnetic field configuration and the 1 A electron beam current were used. At an emittance $>$ 5 π mm·mrad, the capture efficiencies from both approaches agree. The difference of the capture efficiency at low emittances can be explained by not having included, in the analytical formula, the possibility that ions are charge bred to higher charge states before

they reach the outer barrier. Because of this, ions with small emittance are likely to be completely inside the electron beam, have large ionization probability, and can be lost. The capture efficiency from NEBIT is then smaller than what it is predicted by the analytical formula. By flying the particles on axis, the NEBIT result shows that up to 14 % are further ionized to the 2+ charge state before the outer barrier. By including this factor and considering an injected beam with 1 π mm·mrad emittance, the capture efficiency from NEBIT and the analytical formula are 83% and 86%. At 2 π mm·mrad, the difference of 16% results from radial energy pickup of the ions. The 1+ ions pick up the radial energy while crossing the magnetic field and insufficiently have energy to overcome the outer barrier. Therefore, those ions that are reflected at the trap entrance cause the efficiency to be smaller than the value expected from Eq. 5.2.

Concludingly, NEBIT is reliable in calculating capture probabilities. Compared to the simple formula, it provides necessary details of the ion beam while traveling into the EBIT which is not available from the analytical formula, for example, the ion trajectory in the inhomogeneous magnetic field or the effect of the space charge potential to the ion trajectory as well as the phase space and its orientation of the injected beam which is helpful for setting up the ion injection optics.

5.4.4 Comparison of charge evolution between NEBIT and CBSIM

CBSIM is a popular code to study charge evolution developed by R. Becker and O. Kester [44]. The charge evolution in CBSIM is calculated from a rate equation which includes cross sections for charge exchange, radiative recombination, and a model for ion heating. However, to compare the charge evolution between NEBIT and CBSIM, the charge exchange

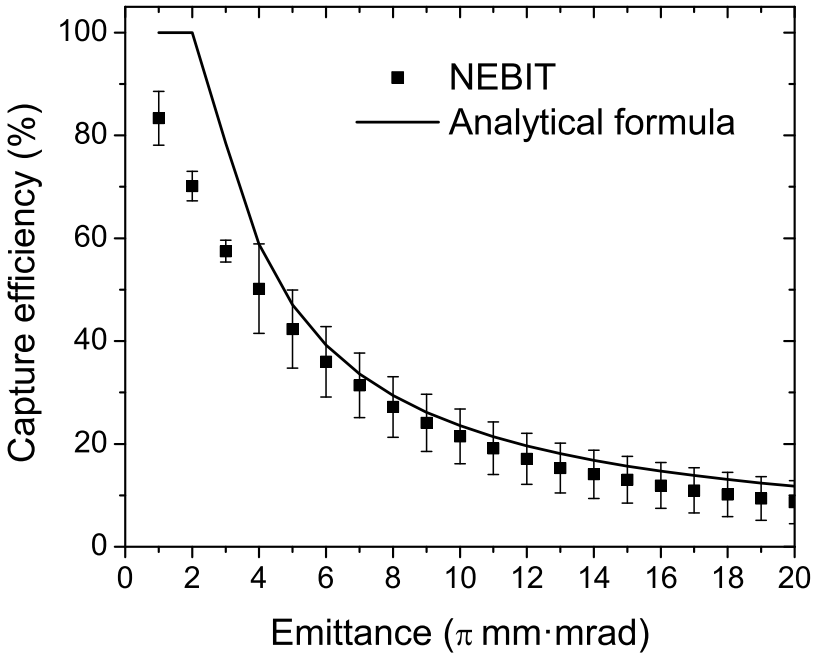

Figure 5.11 Comparison between the capture efficiency calculated from the analytical formula and NEBIT with the electron beam current of 1 A and the 6T-6T magnetic field configuration.

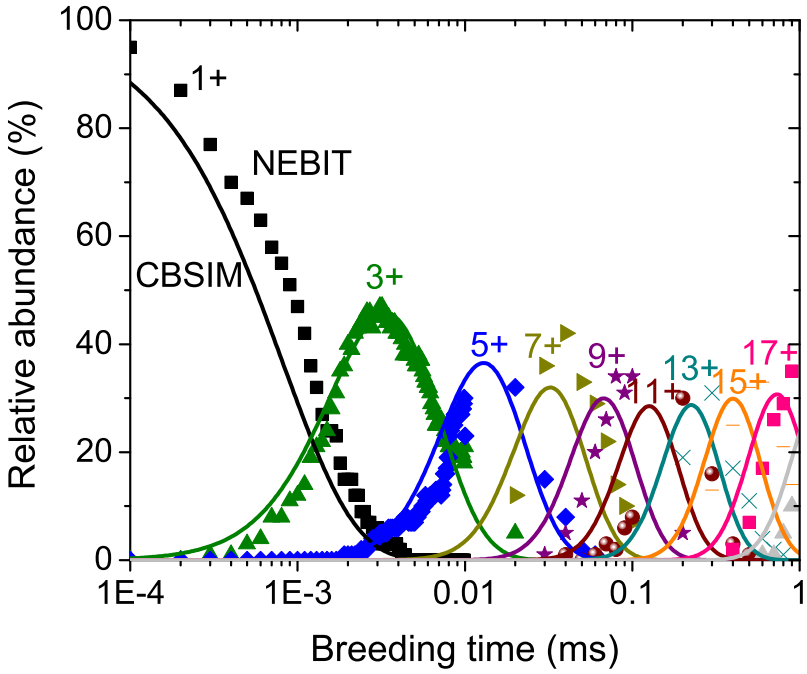

Figure 5.12 Charge evolution of iron ions calculated from CBSIM (lines) and NEBIT (symbols). The highest relative abundances on the leftmost and rightmost curves of the figure represent charge states of Fe^{1+} and Fe^{17+}, respectively. The calculation stopped at a charge breeding time of 1 ms and the electron beam of 1 A and the 6T-6T configuration were used.

and the radiative recombination cross sections are neglected because the pressure in the EBIT trapping region is very low and the capture process occurs at low charge states. Therefore, the EI process alone is sufficient. The ionization cross section used in CBSIM is from Lotz's formula as well.

Since CBSIM assumes a constant magnetic field, the 6T-6T magnetic field configuration was used. The NEBIT simulation was performed with the 1 A and 12.5 keV electron beam. The potential allocations for the trap can be found in Table B.3. To simulate charge evolution under conditions used in CBSIM, an ion has to start inside the electron beam and be confined in the trapping region. Both inner and outer barriers are raised high enough

to completely confine ions inside the trap. The calculation runs for 1 ms, which is sufficient to charge breed iron ions up to Fe^{16+}.

The charge evolutions computed from CBSIM and NEBIT are illustrated in Figure 5.12. To obtain the charge evolution from CBSIM, we need to know the electron beam current density because the output of CBSIM is recorded as a product of the electron beam current density and charge breeding time. For $I_e = 1$ A, $B = 6$ T, $B_C = 10$ G, the electron beam current density is 1.2×10^4 A/cm^2. At low charge states, the result from NEBIT agrees with the one from CBSIM while there is a small difference at high charge states. The optimal charge breeding time for Fe^{15+} are 0.4 and 0.6 ms calculated from CBSIM and NEBIT, respectively. Since the magnetic field at the edge of the trapping region is significantly weaker than that at the trap center by a factor of two, the ions are likely to experience a lower electron beam current density and require longer breeding time to get charge bred to a higher charge state. Results from both codes show Fe^{17+} dominates in the trap at 1 ms.

In conclusion, only with the electron impact ionization, NEBIT provides the charge evolution consistent with that from CBSIM.

5.4.5 Comparison of capture efficiency between current and earlier versions

Since different approximations are employed in the original and the improved NEBIT code, it is important to understand how these differences can influence the capture efficiency. Figure 5.13 displays a capture efficiency calculated with the earlier and the current versions of the code. The calculation of the current NEBIT version for the small emittance beam was carried out with higher statistics than that for the large emittance. At the small

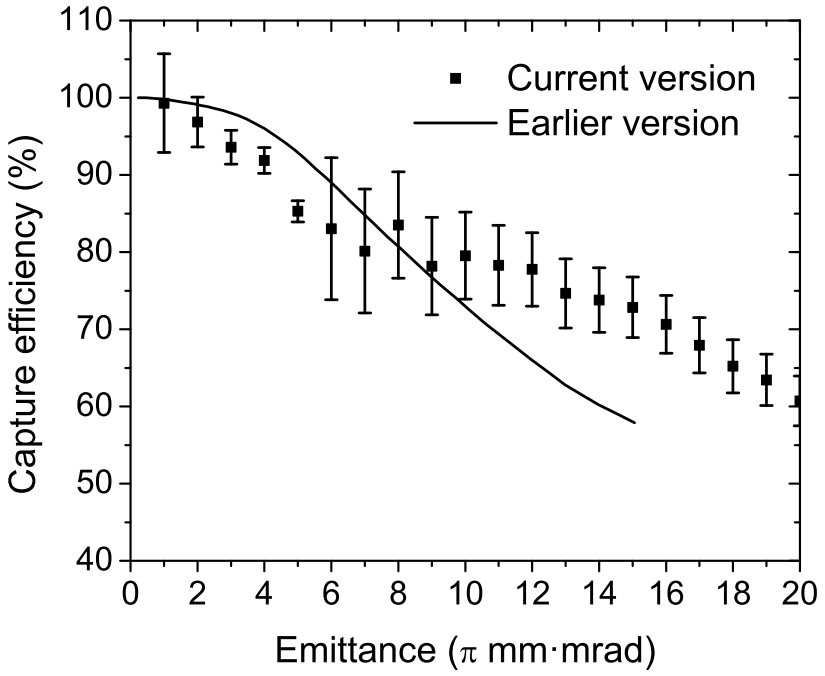

Figure 5.13 Comparison of the the capture efficiency calculated from the current and the earlier versions of NEBIT. The electron beam of 2.5 A and 12 keV were used with the 1T-6T magnetic field configuration.

emittance range, the capture efficiency from both versions are close to 100% and show an only small deviation. When the emittance is larger ($> 10\ \pi$ mm·mrad), the difference is more significant and can be explained by the following: the use of the final EBIT geometry, the implementation of the electron beam energy correction, and the improvement of the electric field imported from SIMION.

The geometry of the EBIT used in the current version has a longer distance between the collector and the entrance of the EBIT, when compared to the earlier version. This difference causes the ions that form the small emittance beam to be ionized into the 2+ charge state before reaching the trap. The small emittance beam entirely overlaps with the electron beam, therefore it has a high probability to be ionized into a higher charge state. This effect is seen in Figure 5.13 where the capture efficiency is computed higher in the

earlier version than the current version.

With the electron beam energy correction included (Eq. 2.8), the space-charge potential created by the electron beam is larger and deeper than that without the correction. Because of this, ions at larger emittance are well trapped. Furthermore, the electric field from SIMION also provides the radial component, which is not included in the earlier version of NEBIT, to help radially confine ions. These two enhancements are particularly important for the injected ion beam with large emittance.

5.5 Simulation results

We have seen in the previous sections that NEBIT is a reliable tool to study the capture efficiency. This section will show the simulation results from NEBIT for different operation parameters.

5.5.1 Capture efficiency with maximum design parameters

The capture efficiencies were simulated for the electron beam currents of 1 A and 2.5 A. The electron beam currents were chosen according to the value we could obtain from the previous electron gun commissioning [64] and the maximum designed current.

Figure 5.14 depicts the capture efficiency as a function of the ion beam emittance for the electron beam currents of 1 A and 2.5 A produced by cathodes with 6.35 and 12.7 mm diameters, respectively. An electron beam energy of 12.5 keV at the trap center as well as the 1T-6T magnetic field configuration was used. The 60 keV Fe^{+} beam was injected into the EBIT with the 1T-6T magnetic field configuration. The iron beam was chosen because it is the heaviest element whose database for the EI cross sections are available. The trap

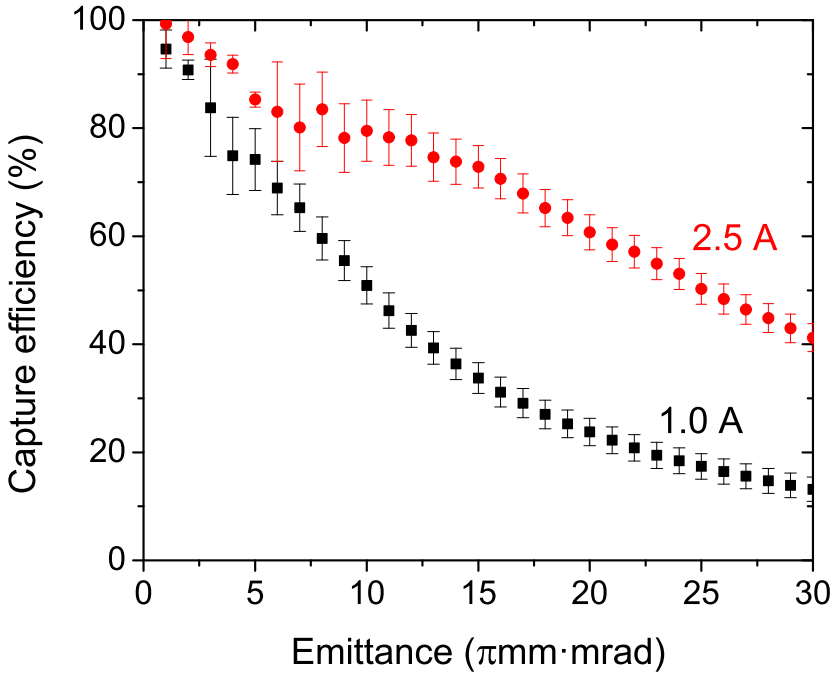

Figure 5.14 Capture efficiency as a function of injected beam emittance for 1 A (black) and 2.5 A (red) electron beam current. The calculation were carried out with the electron beam energy of 12.5 keV and the 1T-6T magnetic field configuration.

of 0.75 m was defined between LTC11 and LTE4 electrodes, see Figure B.1. At small emittance, the capture efficiency is high since the ions travel close to the electron beam axis and have high probability to be trapped during the round-trip flight. On the other hand, the beam with large emittance has a small chance to be charge bred and trapped since the overlap between the ion beam and the electron beam is small. The decrease of the total efficiency for the injected beam having large emittance was also observed at REXEBIS [12]. At 10 π mm·mrad of ion beam emittance, the capture efficiencies of 80 % and 51 % for the electron beam current of 2.5 A and 1 A, respectively, could be reached in the simulations. As expected, the higher the electron beam current, the higher the efficiency will be.

Assuming $B_C = 10$ G, the electron beam current of 1 A produces 1.5 kV of space-charge potential and the electron beam current density of 1.2×10^4 A/cm^2 can be reached at the trap center. The 2.5 A electron beam current creates 3.7 kV space-charge potential with electron beam current density of 8.8×10^3 A/cm^2. The fact that the higher electron beam current gives the lower electron beam current density is due to the increased cathode size for the higher current.

The capture efficiency was also investigated for different magnetic field configurations as shown in Figure 5.15. The same ion beam parameters and trap size as the previous calculation were used for this study. The 12.5 keV and 1 A electron beam was used and yielded the electron beam current density of 1.6×10^3 A/cm^2 and 1.2×10^4 A/cm^2 at 1 T and 6 T regions, respectively. At 10 π mm·mrad of ion beam emittance, the efficiencies of 51 % and 21 % were predicted. For the 1T-6T configuration, the electron beam radius at the extended trap section is larger than that of the 6T-6T. Since the bigger electron beam radius provides a better overlap between the ion and the electron beam, the capture

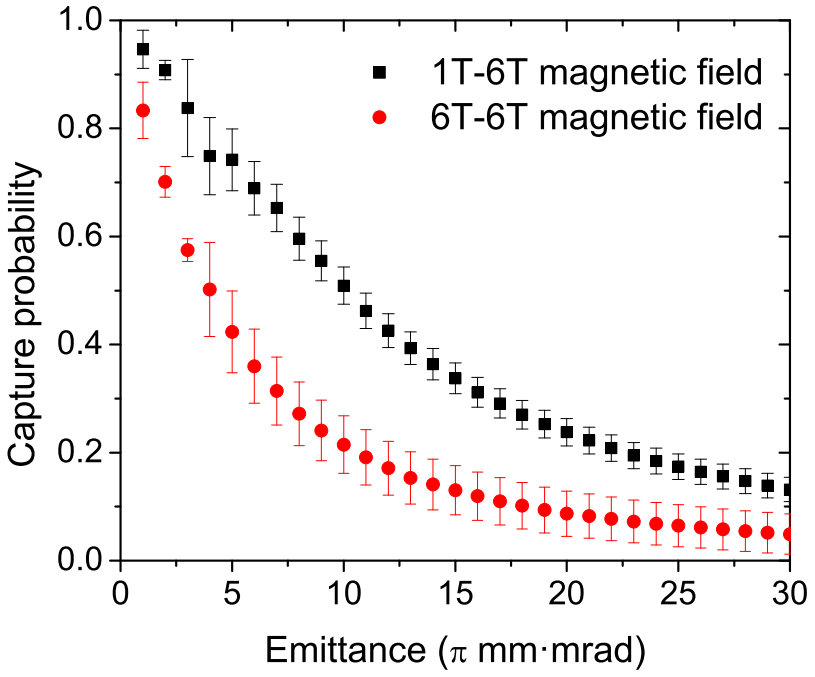

Figure 5.15 Capture efficiency as a function of injected beam emittance for 1T-6T (black) and 6T-6T (red) configurations for the 1 A and 12.5 keV electron beam.

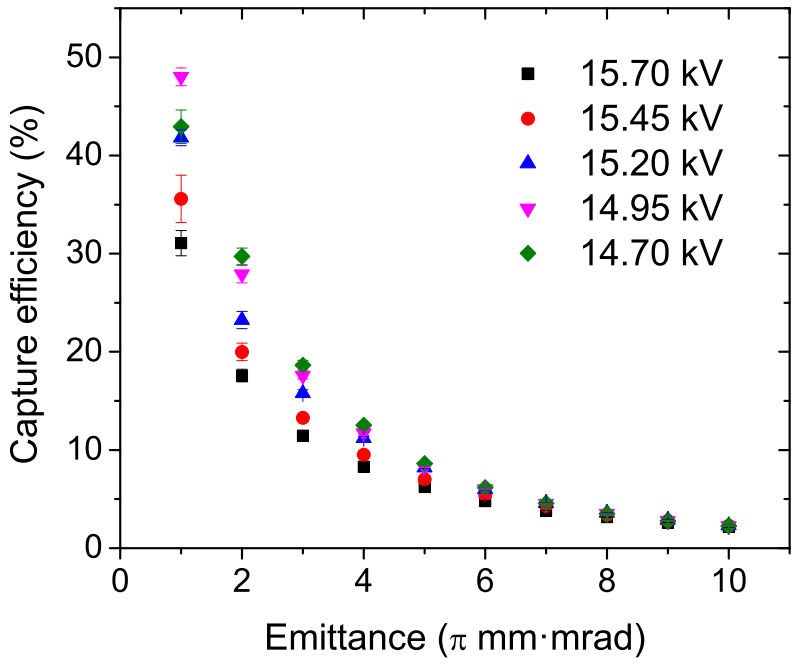

Figure 5.16 Calculated capture efficiency as a function of voltage applied to the acceleration/deceleration electrode.

efficiency becomes larger.

5.5.2 Capture efficiency with different transport optics

The optimization of the setting was performed for every electrode but only three of them, the acceleration/deceleration electrode, the Einzel lens, and the transfer lens, were chosen as examples. The calculation in this section used the EBIT and the beam parameters from the experiment. The 2T-2T magnetic field configuration as well as the 19.5 keV and 135 mA electron beam was used and the 20 keV K^+ beam was injected into the EBIT. Figure 5.16 illustrates the capture efficiency as a function of emittance for different voltages applied to the acceleration/deceleration electrode. The variation of the voltages causes the efficiency to be different by 17 % and 4 % at 1 and 4 π mm·mrad. Within this range of voltage, the

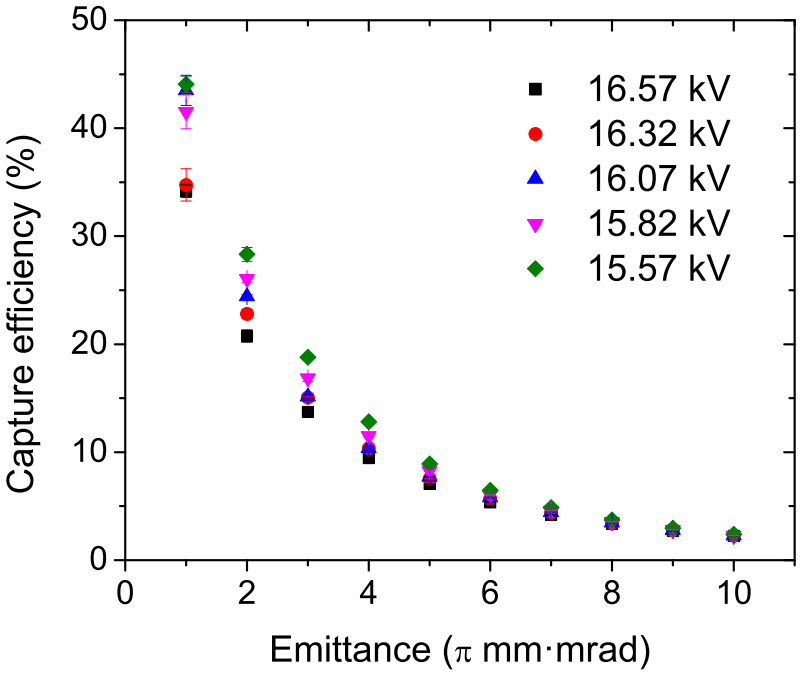

Figure 5.17 Calculated capture efficiency as a function of voltage applied to the Einzel lens: 16.57 (black), 16.32 (red), 16.07 (blue), 15.82 (magenta), and 15.57 kV (green).

capture efficiency is less influenced by the acceleration/deceleration voltage at a large than a small emittance beam. For the 1 π mm·mrad beam, 14.95 kV applied to the electrode provides the highest efficiency. If the emittance is larger than 1 π mm·mrad, the highest efficiency is obtained when the voltage is adjusted to 14.70 kV.

Figure 5.17 depicts the calculated capture efficiency as a function of voltage applied to the Einzel lens. Within a range of 1 kV applied to the Einzel lens, the capture efficiencies are different by 10 % and 3 % for 1 π mm·mrad and 4 π mm·mrad beams, respectively. The highest capture efficiency is received by adjusting the voltage of the Einzel lens electrode to 15.57 kV. The effect on the Einzel lens is small at a large emittance beam as well.

Simulations were also performed to optimize the voltage applied to the transfer lens, Figure 6.4 item 4. It is found that within 1 kV range, the capture efficiency for 2 π mm·mrad

and larger are almost equivalent. By using NEBIT to optimize the voltage setting for the beam transport into the EBIT, we do not only obtain the optimal value but also are able to indicate that the acceleration/deceleration electrode and the Einzel lens are the most sensitive to the ion beam.

5.5.3 Capture efficiency with parameters used in experiments

Different EBIT parameters, electron beam currents, trap sizes, and trap potential were systematically studied using NEBIT. An electron beam of 19.5 keV and the 2T-2T magnetic field configuration were used throughout the following calculations. Figure 5.18 displays the simulated capture efficiency as a function of electron beam current for the injected beam emittance ranging between 1 - 6 π mm·mrad. The maximum trap size of 0.64 m, defined by the distance between LTC10 and LTE4 electrodes (see Figure B.1), was set. At this range of the electron beam current, the capture efficiency is apparently different even when the emittance of the injected beam is small. The trend of the capture efficiency for different electron beam currents is in the same direction that the higher the electron beam, the larger the simulated capture efficiency. The relation between the electron beam current and the ionization probability can be found in Eq. 2.15 and 2.16.

Figure 5.19 illustrates the simulated capture efficiency as a function of trap size for the injected beam emittance ranging between 1 - 6 π mm·mrad. The electron beam current of 100 mA were used. The capture efficiency for the beam with smaller emittance is more influenced by the trap size than that with larger emittance. Because of the short distance in the trapping region, ions do not spend enough time to interact with the electron beam and are not further ionized to the 2+ charge state. Therefore, a small amount of ions are

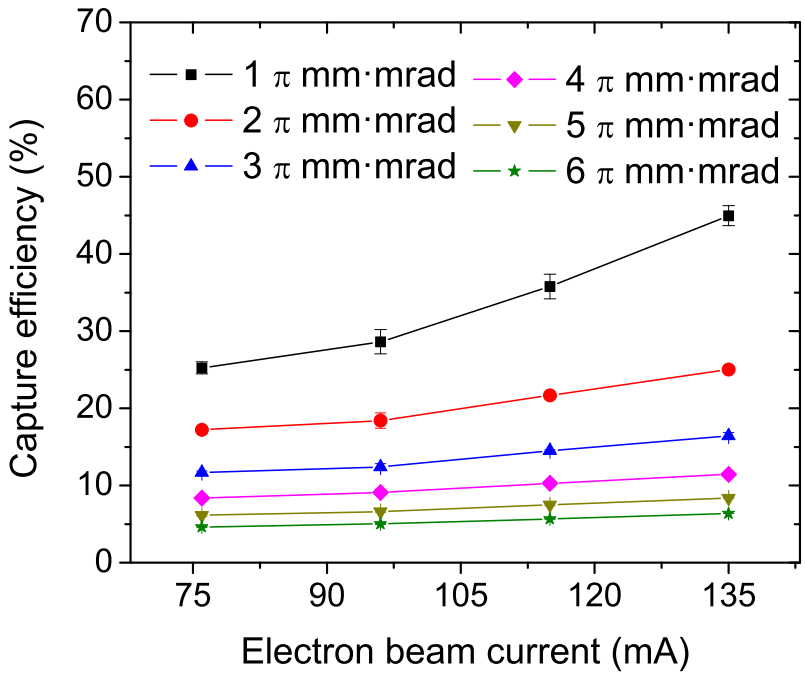

Figure 5.18 Calculated capture efficiency as a function of electron beam current for injected ion beams with emittances from 1 - 6 π mm·mrad.

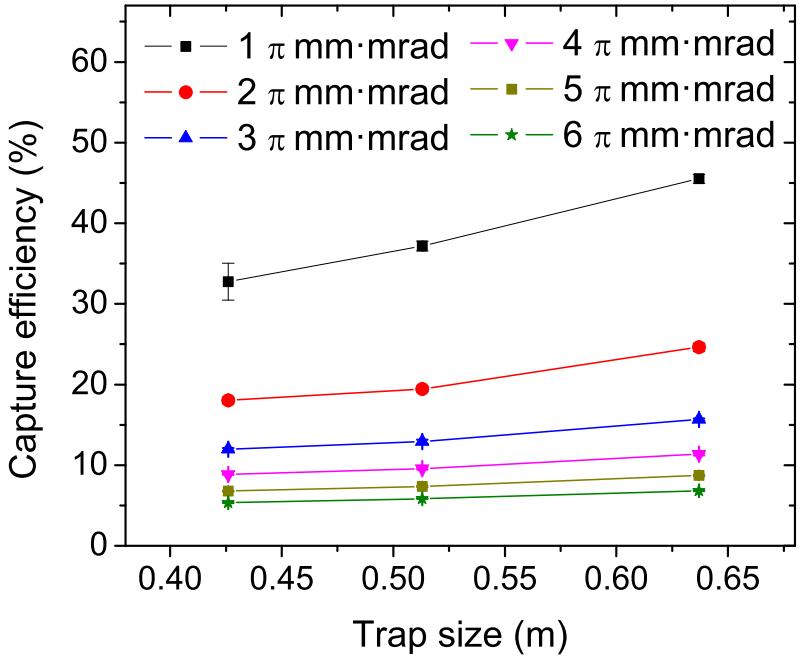

Figure 5.19 Calculated capture efficiency as a function of trap size for injected ion beams with emittances from 1 - 6 π mm·mrad.

trapped and the capture efficiency is low.

Figure 5.20 depicts simulated capture efficiency as a function of trap depth for the injected beam emittance ranging between 1 - 6 π mm·mrad. The electron beam current of 122 mA was used. The negative value indicates that the trap potential is lower than the outer barrier. The trap potential has to be optimized since the trap depth, corresponding to the ion energy in the trap, can influence the capture efficiency. The optimal value is -30 V for a beam of 1 π mm·mrad and changes to -10 V for a beam of 2 π mm·mrad or higher. The optimal value expresses the balance of the ion energy and the trapping potential. If either of these values is too large or small, the capture will become small. The relation between the capture efficiency and the trap depth are described in details in Section 6.3.4.

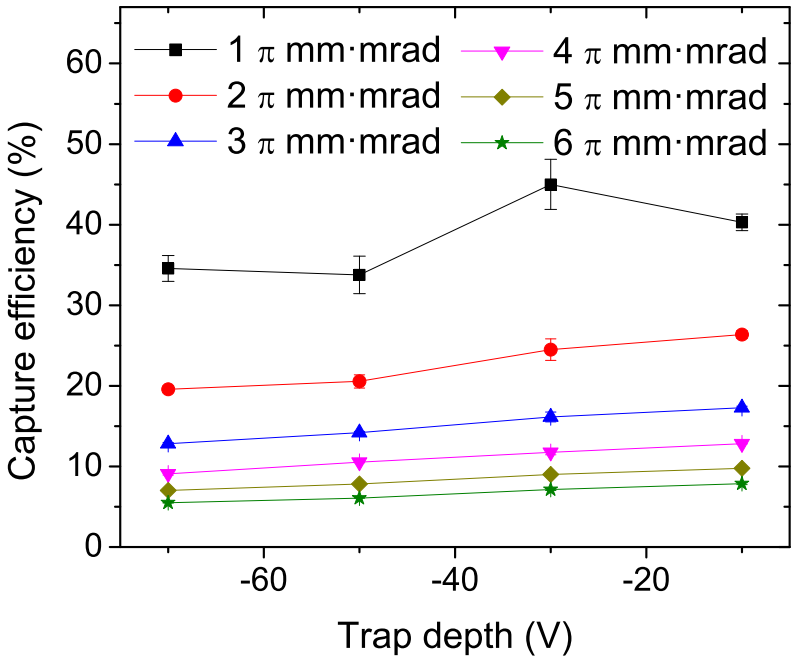

Figure 5.20 Calculated capture efficiency as a function of trap depth for injected ion beams with emittances from 1 - 6 π mm·mrad.

Chapter 6

Measurements, Results, and Discussion

In order to investigate the efficiency of the NSCL EBIT, several studies were performed. The emittance of the ion beam generated from the test ion source was determined. The voltage settings to efficiently transport the ion beam into the EBIT were optimized by employing a radial energy pickup technique and observing the location of the ion reflection. With optimal tuning, capture efficiencies were systematically studied through the variation of injected ion beam currents, electron beam currents, trap sizes, and trap potential depths. From the charge state evolution, the effective electron beam current density was estimated. Details of each measurement are contained in the following sections. In Section 6.1, the transverse emittance measurement of the beam from the test ion source is discussed. The optimization of the ion injection into the EBIT is described in Section 6.2. The relation between capture efficiency and the EBIT parameters is investigated in Section 6.3. Section 6.4 reports on the charge state evolution of potassium ions and a measurement of the effective current density of the electron beam.

6.1 Transverse emittance measurement of K^+ beam

We have seen in Section 5.5 that the capture efficiency changes as a function of the injected beam emittance. If the emittance of the beam from the test ion source is well measured, it allows us to calculate the capture efficiency of the EBIT correctly. With the current experimental setup, the emittance measurement was performed by using a well known quadrupole scan method [65]. The method requires, at a minimum, a quadrupole lens and a screen for imaging the beam. The emittance is obtained by fitting the beam profiles using the quadrupole transfer matrix elements.

6.1.1 Experimental setup and procedure

Figure 6.1 schematically illustrates the devices used for the emittance measurement. A 20 keV beam of K^+ was generated from the test ion source and transported to an MCP at BOB 1. Along the beamline, the beam was directed by an Einzel lens, a quadrupole triplet, steerer electrodes, an electrostatic bender, and an electrostatic deflector. Inside BOB 1, the MCP was mounted to provide an image of the beam , which was captured by a camera.

The horizontal and vertical beam profiles were extracted from the beam images with different voltages applied to each of the three quadrupoles of the triplet as depicted in Figure 6.2. The voltages were varied independently for one quadrupole during the measurement while keeping the voltages of the others constant. Once the applied voltage was off the optimal value, the beam was out of focus leading to a wider beam diameter on the viewing screen in one direction. A Gaussian function was used to fit the beam profile and the beam size was described by one standard deviation (1σ) which is equivalent to the r.m.s radius.

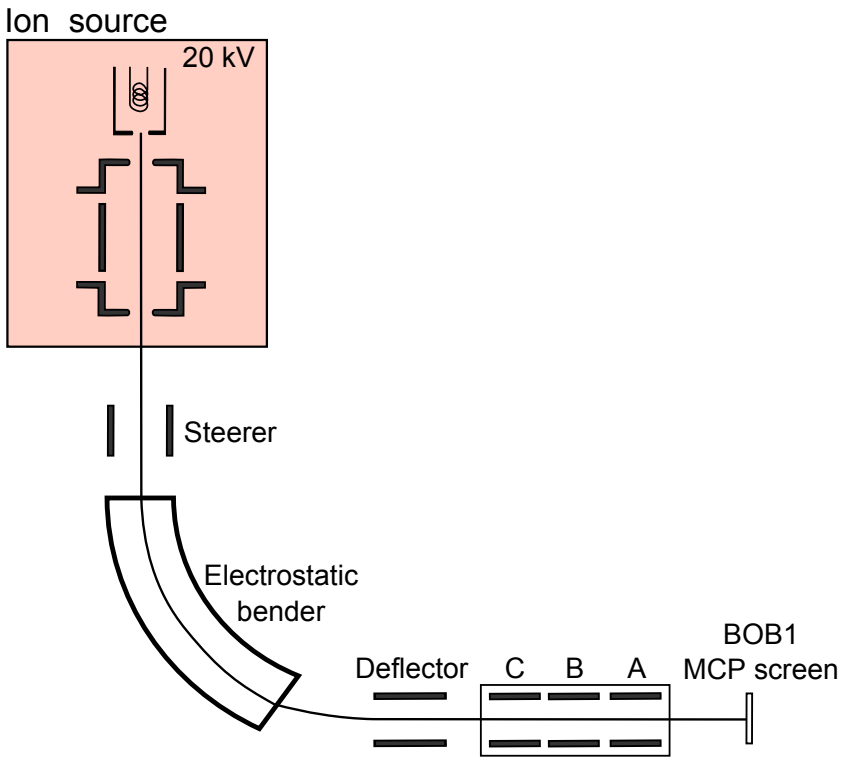

Figure 6.1 Schematic showing the experimental setup for the emittance measurement.

The transfer matrix of the triplet is needed for the quadrupole scan method and the details in Appendix shows how to extract the transfer matrix of the triplet. Fitting the square of the r.m.s. beam size as a function of applied voltage with Eq. 3.8 provides the beam emittance. By repeating the same steps with all three quadrupoles, three values of the emittance are given.

6.1.2 Emittance of the K^+ ion beam

Figure 6.3 illustrates the fitting results from quadrupole A(a), B(b), and C(c). The emittance extracted from quadrupole A and C are $\epsilon_x = 1.41 \pm 0.02$, $\epsilon_y = 4.53 \pm 0.35$ π mm·mrad and $\epsilon_x = 5.54 \pm 0.13$, $\epsilon_y = 3.71 \pm 0.38$ π mm·mrad, respectively. The error bars are calculated from the fitting process.

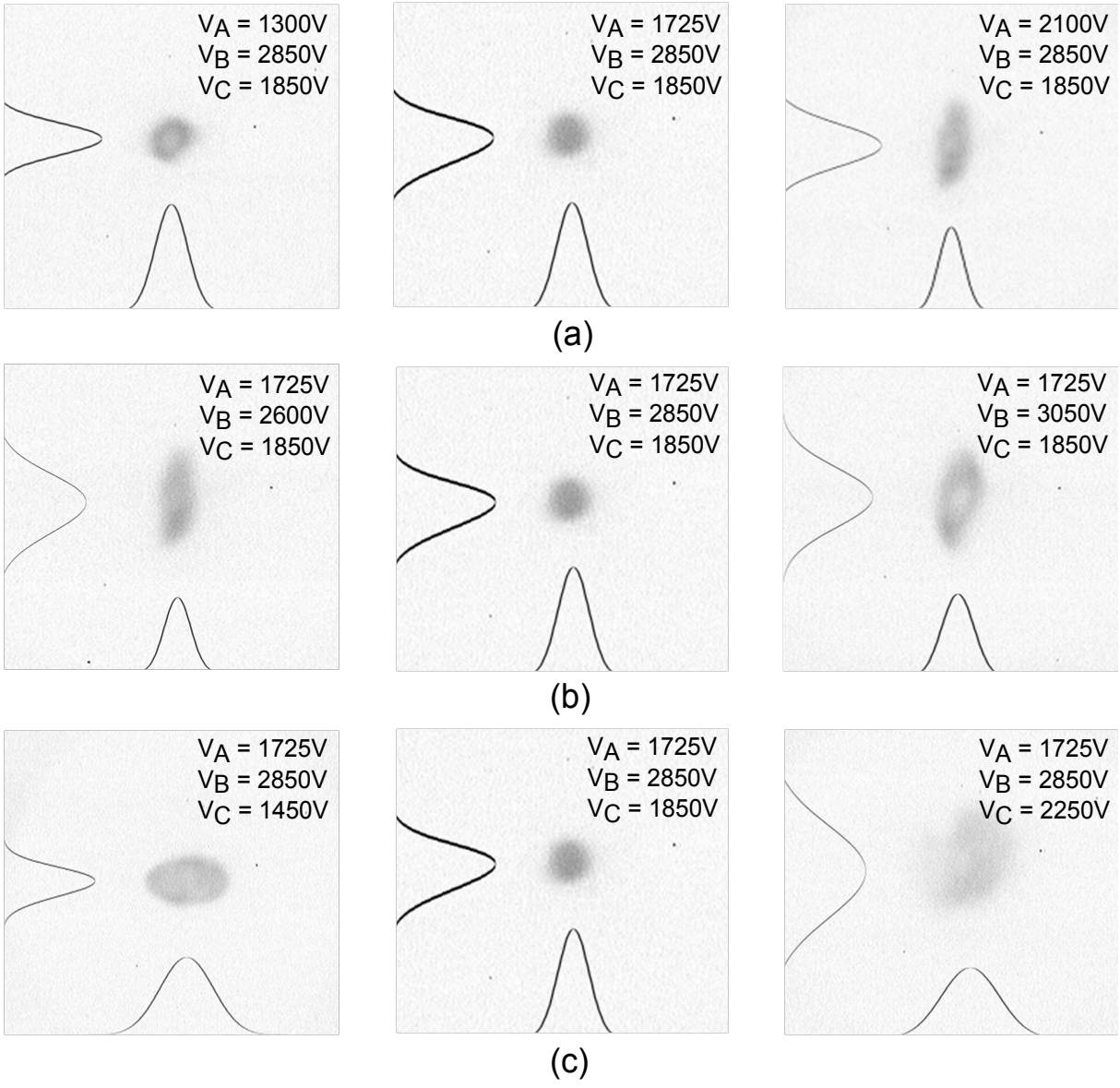

Figure 6.2 Examples of beam images captured by the MCP viewer with different voltages applied to quadrupole A(a), B(b), C(c).

The data set of the beam size from varying the voltages applied to the quadrupole B cannot reasonably be fitted with the quadratic function to provide the emittance. The plot in Figure 6.3b shows a small peak at the center of the curve. Even though there is not a solid conclusion for this small peak, a possible reason is the beam size may be so large that the ions experience higher order effects of the electric field generated by the quadrupole B. An independent emittance measurement was performed with the same triplet and the result from the quadrupole B also showed a small peak. From two unrelated emittance measurements, the triplet was similarly applied with positive, negative, and positive voltages. For this voltage pattern, the horizontal beam size is always large at the quadrupole B location. This may confirm that the small peak resulted from the large beam size.

A SIMION simulation was performed to calculate the expected emittance of the ion beam from the test ion source. The filament coil was constructed with toroidal electrodes. Potassium ions were generated at the surface of the electrode with 0.01 eV of kinetic energy. The ions were driven to the anode pinhole by the potential difference between the filament and the anode. Other ion optics, such as the Einzel lens, an electrostatic bender, etc., were added along the beamlime. The K^+ beam was transported toward BOB 1 where its properties were recorded. The simulated r.m.s. emittance is 0.77 π mm·mrad for a 20 keV ion beam.

After the measurement was finished, the test ion source was disassembled and it was found that the anode was not firmly installed in the quartz chamber. The center of the anode was off-center of the filament by 1 - 2 mm. This confirmed that the source was not properly aligned to the beamline axis. Since the anode was also deformed from a flat

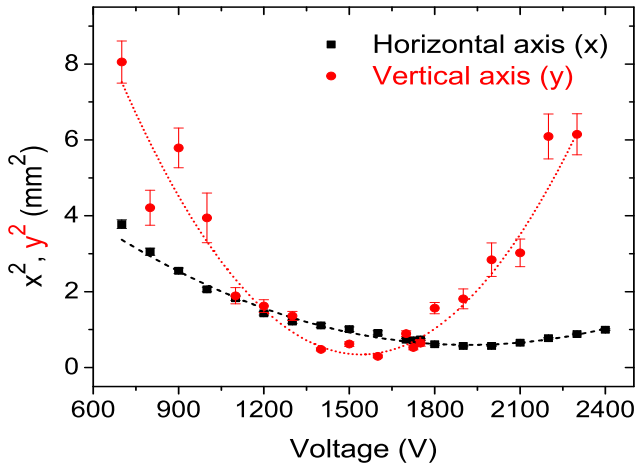

(a)

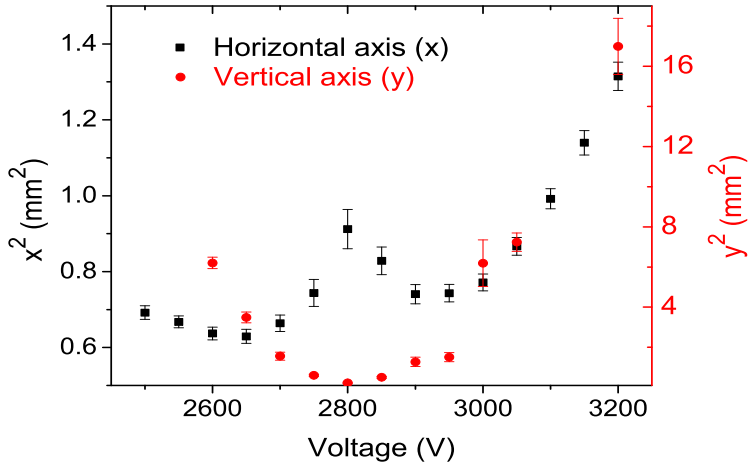

(b)

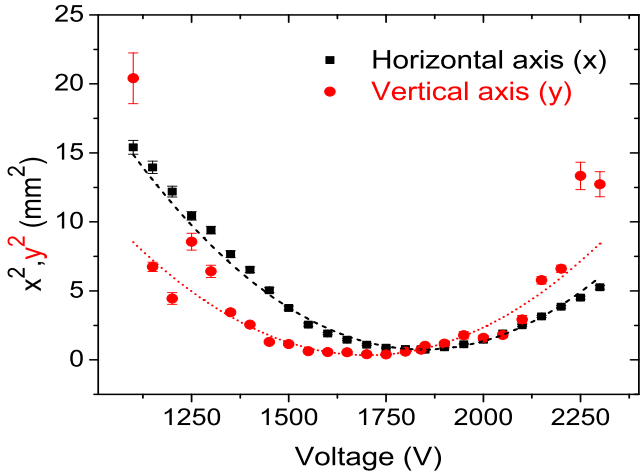

(c)

Figure 6.3 Quadratic fits of beam size squares at different voltages applied to the quadrupole A(a), B(b), and C(c).

to a convex shape, this could distort the electric field at the pinhole area and cause the difference between the calculated and measured emittance. In addition, the K^+ beam was possibly generated from the anode as the pinhole on the anode was slightly covered by substances produced from the filament. During the past commissioning of the EBIT, there was evidence that the K^+ beam was not only generated from the filament but also partly from the anode. This was confirmed by applying a high enough voltage to the anode to block the K^+ beam from the filament yet still detecting the K^+ beam. These reasons may explain why the measured emittance is larger than the expected value.

By taking into account that the beam is large inside the triplet and the data from the quadrupole B cannot be fitted with the quadratic function, the emittance of the ion beam are $\epsilon_x = 1.4 - 5.5\ \pi$ mm·mrad and $\epsilon_y = 3.7 - 4.5\ \pi$ mm·mrad. The average emittance is $3.8\ \pi$ mm·mrad.

6.2 Optimization of ion injection

The NSCL EBIT charge breeder aims to achieve a high total efficiency taking into account injection, extraction, capture, and charge breeding efficiencies. The voltage settings of the beam transport optics have to be optimized in order to ensure maximum overlap of the ion and the electron beams in the trapping region.

6.2.1 Experimental setup for ion injection and capture process

Figure 6.4 depicts the schematic of the experimental setup of the ion injection. A 20 keV K^+ beam from the test ion source was injected into the EBIT. The beam alignment was adjusted by using the same optical elements as in the emittance measurement, described

in Section 6.1. While entering the high voltage region, the beam was first retarded by an acceleration/deceleration column consisting of an acceleration/deceleration electrode and an Einzel lens. The column and the EBIT were biased to 17 kV, and the potential in the trapping region was set to be 15 V lower than the ion beam energy.

During the extraction process, the ions were ejected through the collector. The acceleration/deceleration electrode, the deflector, and the triplet between the test ion source and BOB 1 were switched from the optimal injection to the optimal extraction voltage. Along the beamline toward detectors at BOB 4 , the quadrupole triplet, a quadrupole singlet, and two quadrupole doublets were used to focus the beam before entering the Q/A separator, between the electrostatic magnet, before entering the dipole magnet, and before the detectors, respectively.

For the alignment of the ion beam and the energy spread measurement, another MCP and Faraday cup were installed next to the last trap electrode where the electrode gun head was inserted. These diagnostic devices were used to capture images and currents of the ion beam that passed through the trapping region. The transport efficiency was obtained and used to identify the alignment between the trap and the injected beam. After finishing the transport efficiency measurement, the detectors were retracted and the electron gun head was moved to the detector location.

The electrostatic benders at the Q/A section were utilized to select ions with a certain energy. Located between the dipole magnet and the electrostatic benders, a Faraday cup monitored the current of all the HCIs having the same range of axial energy. After the bending magnet, the MCP in combination with an oscilloscope was used to observe the TOF signal, and the current of the selected ions was recorded by a Faraday cup.

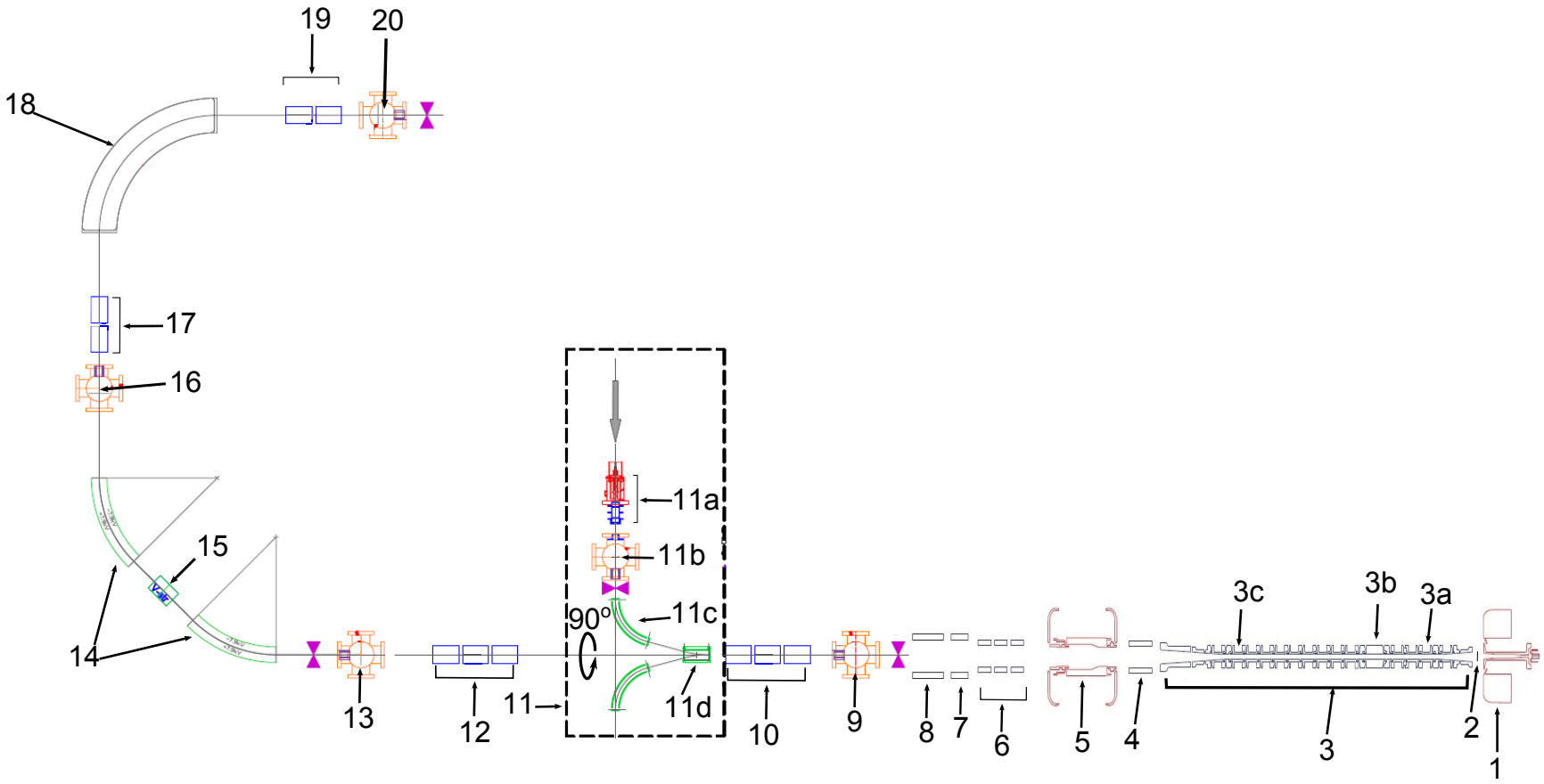

Figure 6.4 The NSCL EBIT experimental setup: (1) electron gun, (2) electron gun Faraday cup, (3) trap electrodes and primary components including inner barrier (3a), main trap (3b), and outer barrier (3c), (4) transfer lens, (5) electron collector, (6) Einzel lens, (7) acceleration/deceleration column, (8) ground electrode, (9) beam observation box 1 (BOB 1), (10) quadrupole triplet lens, (11) LA source consisting of ion source (11a), deflector (11b), electrostatic bender (11c), deflector (11d), (12) quadrupole triplet lens, (13) BOB 2, (14) electrostatic bender, (15) quadrupole lens, (16) BOB 3, (17) quadrupole doublet, (18) bending magnet, (19) quadrupole doublet, and (20) BOB 4.

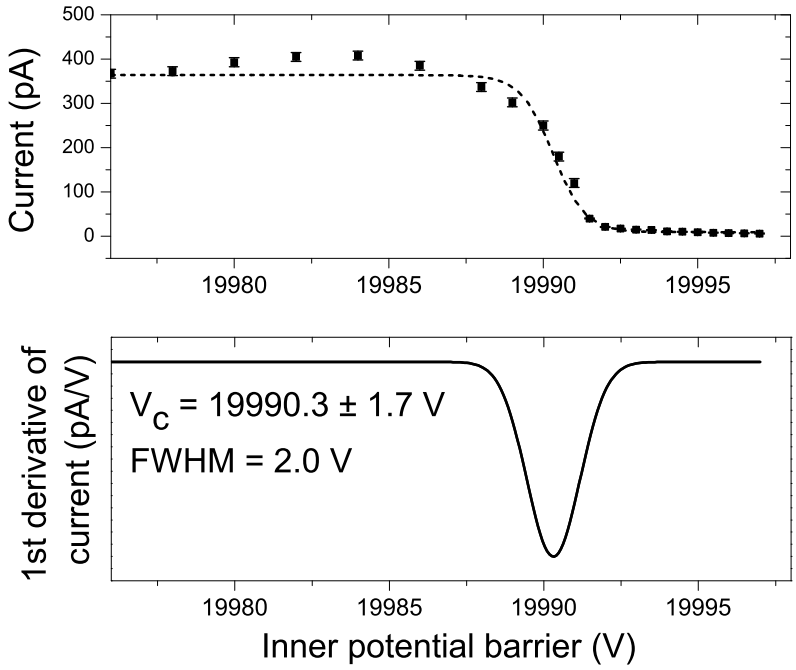

Figure 6.5 A plot of the ion beam current as a function of the inner potential barrier (Top) and a Gaussian fit of the first derivative of the ion beam current with respect to the inner potential barrier (bottom).

6.2.2 Axial energy spread measurement

To minimize beam losses during the beam transport, a technique of radial energy pickup minimization was employed. While crossing the magnetic field, an ion converts a part of its axial to radial kinetic energy. Due to the large overlap between the electron and the ion beam, ions with small radial energy are more likely to be captured in the EBIT than those having large radial energy. The ions with large radial energy can also be reflected at the trap entrance or hit an electrode while returning at the inner barrier location. The optimal voltage setting provides the maximum reduction in the radial energy pickup.

While injecting the ion beam into the EBIT, the inner potential barrier was scanned between 2,980 and 3,000 V on top of 17 kV high voltage. The current of the ion beam passing through the trapping region was measured by the electron gun Faraday cup. The

optimized setting was obtained by varying the voltages applied to the acceleration column lens, the transfer lens, the first few trap electrodes at the trap entrance, and other transport optics. Figure 6.5 shows the ion currents measured by the electron gun Faraday cup, a fitted curve, and the first derivative as a function of the inner potential barrier. The data are fitted with a sigmoid function and its first derivative is fitted with a Gaussian function. A FWHM of 2.0 V from the fit having a $\chi^2_\nu = 1.56$ is obtained. To investigate the energy spread, a simulation was performed to study the ion production in the ion source. It was found that ions created from the filament, where the potential is 6 - 9 eV higher than the potential platform, were extracted. The simulation results in Appendix show the trajectories of ions that can be transported to the beam line. These ions are created from the filament at location 4, 5, and 6 which are applied with 6, 7.5, and 9 V higher than the ion source platform, respectively.

In conclusion, the axial energy spread of the ion beam was measured by transporting the ion beam into the trap and the optimal voltage setting was obtained by minimizing the ion radial energy. Having a small axial energy spread of 2 eV is important to provide a good measurement of capture efficiency.

6.2.3 Ion reflection in the EBIT

The behavior of the injected beam in the EBIT was studied by measuring the TOF signal of reflected ions. While traveling into the trap, incoming ions could reflect at any position where the ion axial energy was insufficient to overcome the potential. By setting the inner potential barrier to be significantly higher than the ion beam energy, the beam will not be able to traverse the inner barrier. In order to reach the highest capture efficiency, the TOF

signal must be dominated by ions reflected off the inner barrier. This guarantees that the ions enter the trapping region where the capture and the charge breeding process occur.

The ion beam from the test ion source was injected into the EBIT. Since there was not a trapping process, the outer potential barrier was set to be equal to the trap potential. The voltage applied to the deflector electrode was varied between the optimal values for injection and extraction. The ion beam from the reflection was transported to the Q/A separator, where the electrostatic benders and the bending magnet were set for the 20 keV ion beam and K^+ ions (Q/A = 1/39), respectively. An oscilloscope was connected to the MCP at BOB 4 to record the TOF signal and a trigger to the TOF signal was generated by a function generator. Figure 6.6 depicts the time sequence for varying voltages applied to the deflector and the outer barrier between injection and extraction. For the study of ion reflection, only the time sequence of the deflector is applied while both sequences of deflector and the outer barrier are used when charge breeding process exists. The data acquisition of ion TOF starts when the deflector voltage is switched from the injection to the extraction voltage. The extraction time is always kept at 5 ms while the injection and the breeding time varies according to the cycle period. The breeding process begins and stops at 0.4 ms after the deflector voltage changes between the extraction and the injection voltage. The outer barrier is also lowered for 5 ms to eject HCIs out of the trap.

The TOF spectra in Figure 6.7 displays peaks of TOF signals for different locations where the ion beam returns. By individually adjusting the potential on each electrode, we could identify which electrode reflected the beam. Figure 6.7a shows the spectrum which was formed by ions reflected inside the EBIT when the LTE4 electrode (see Figure B.1) was set as the inner barrier. In Figure 6.7b, after decreasing the LTE4 potential, the ion

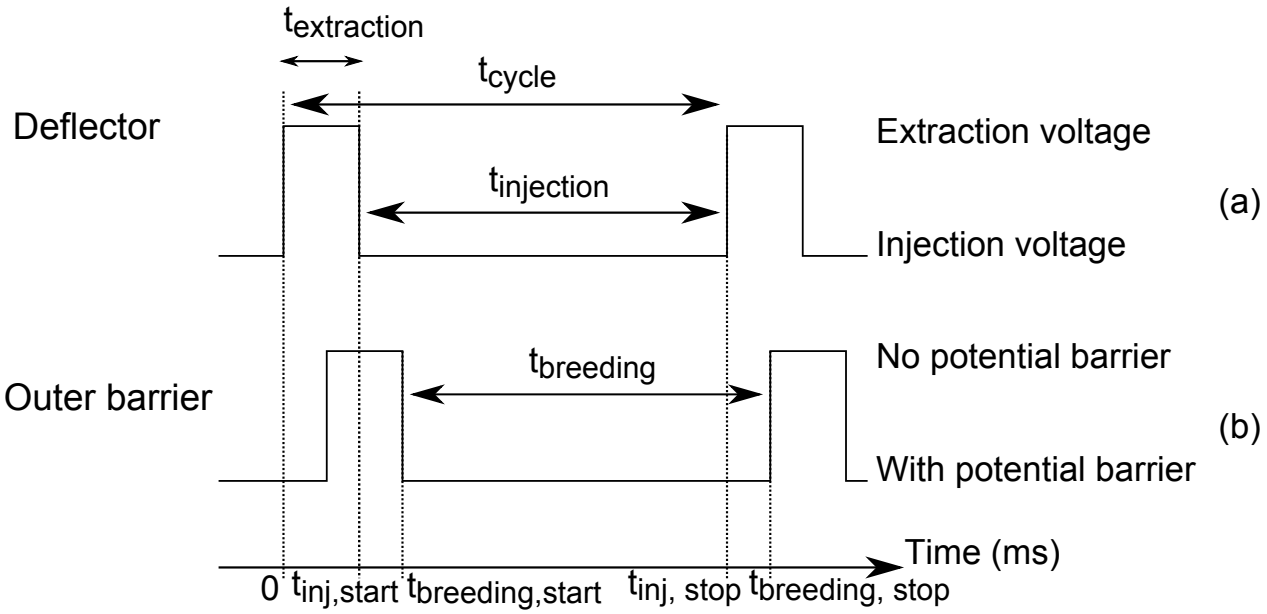

Figure 6.6 Time sequences for the injection and the extraction processes for the deflector (a) and the outer barrier (b). The time sequence for the outer barrier is used for charge breeding process.

beam passed through the trapping region toward the electron gun and the part of the TOF signal corresponding to the ion reflection at the LTE4 disappeared. By lowering LTE1, its contribution to the TOF signal was measured. The peaks of the TOF signal in Figure 6.7c and Figure 6.7d are almost identical. The peak in Figure 6.7d disappeared after lowering the voltage applied the LTC11 electrode. From a sequence of lowering the voltages applied to LTE4, LTE1, LTRAP, and LTC11, we can conclude that most of the injected ions reflect off the potential created by LTE4 and a small number of ions reflect at the location of LTE1 and LTC11, while there is no ion reflection at LTRAP.

Ions reflected at the LTC11 location cannot enter the trapping region and get charge bred to higher charge states. If this number of ions is large, it will reduce the injection efficiency. Optimization was performed to increase the fraction of the beam entering the trapping region and to diminish the portion reflected from the outer barrier. In addition to

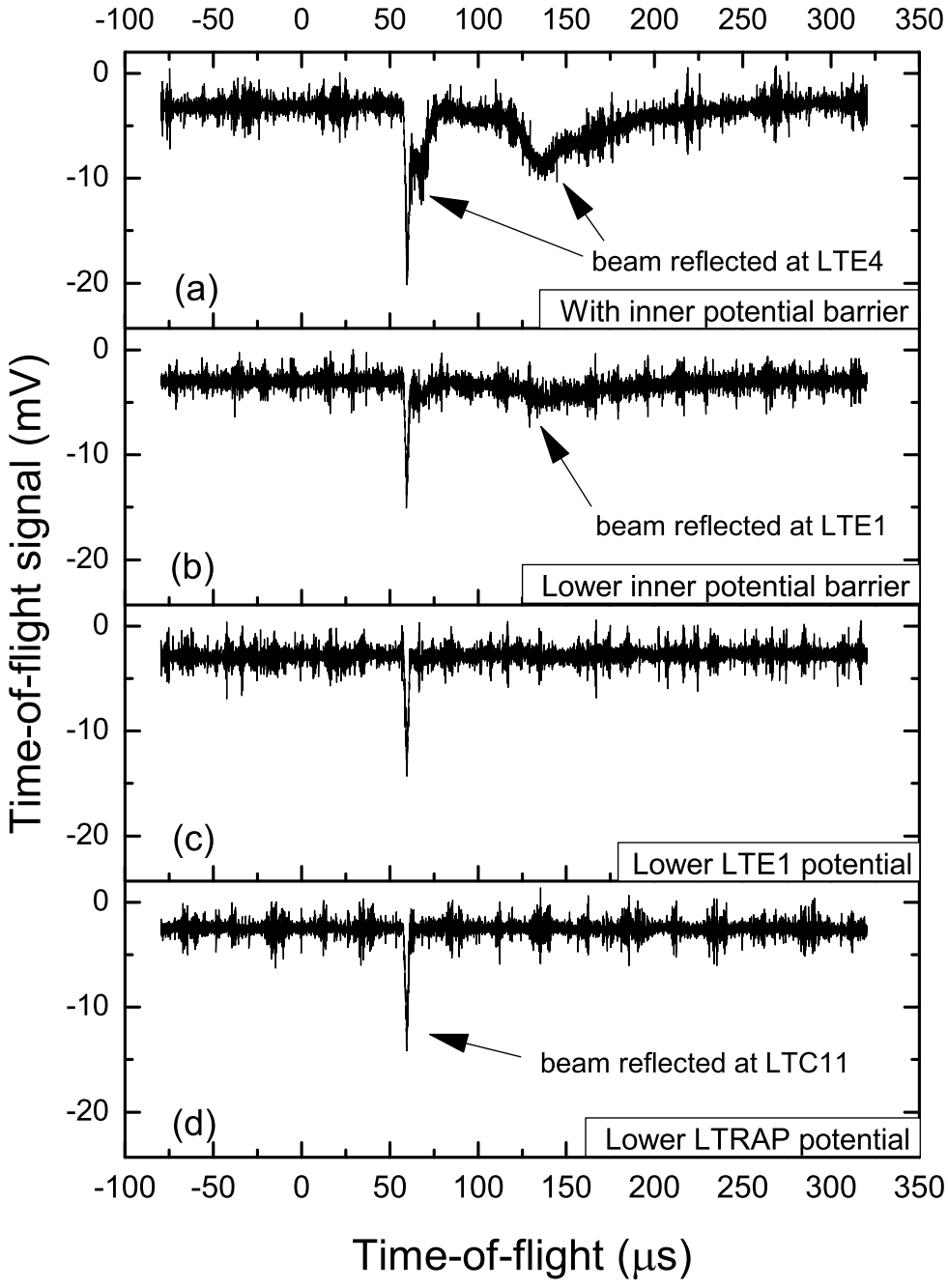

Figure 6.7 TOF spectra of the ion beam measured after lowering the potential applied to each electrode: (a) no lowering, (b) after lowering LTE4, (c) after lowering LTE1, and (d) after lowering LTRAP.

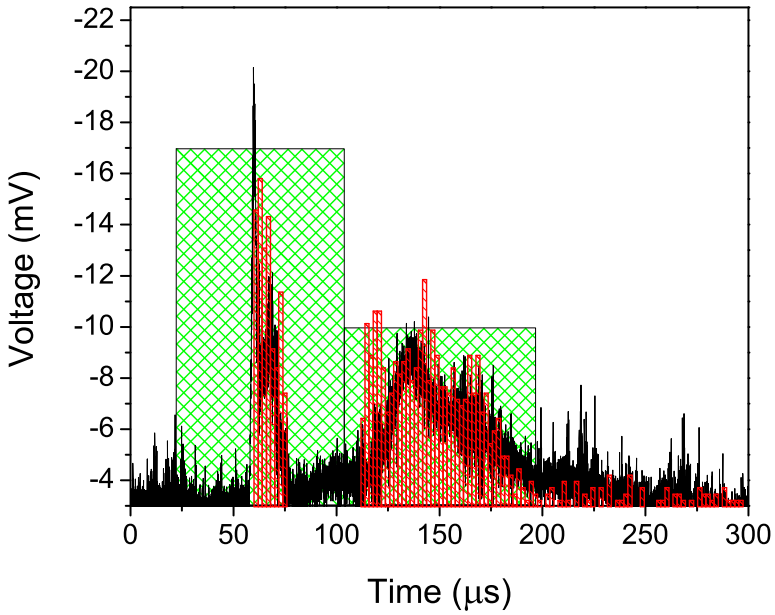

Figure 6.8 TOF spectrum of the ion beam reflected at different locations in the EBIT and simulated histogram that includes voltage delay, overshoot, and undershoot. The pattern area shows expected signal from the ion beam reflected off the trap entrance and the inner barrier.

measuring the TOF signal of ion reflection with the MCP, the Faraday cup at BOB 4 was also used to measure currents of ions reflected at different locations. The total current of ion reflection in Figure 6.7a was 5.8 pA for 50 Hz repetition rate and 5.6 pA reached the center of the trap. With this voltage setting, 95% of the ion beam detected at BOB4 was transported to the trap center.

To better understand the reflection process, a simulation with SIMION was carried out to reproduce the experimental result. The simulation started with the voltage setting that was used to obtain results in Figure 6.7a. Based on the axial energy spread measurement, an ion beam with an energy of 19990 $\pm$ 2 eV at BOB 1 was used. The ion beam was Gaussian distributed with a standard deviation of 0.6 mm corresponding to a beam with FWHM of 1.4 mm. The voltage setting was adjusted to match to the experimental TOF signal, Figure

6.7a. The first TOF signal is expected around 24 μs, equivalent to the time K^+ needed to travel from the deflector electrode to the MCP at BOB 4. The last ion reflected off the trap entrance takes approximately 100 μs to reach BOB 4 and most ions that reflected off the inner barrier should spend less than 200 μs to reach BOB 4. If the injected beam mainly comprises ions reflected off the trap entrance and the inner barrier, the TOF signal is expected to be large at the beginning and then small. The large contribution of the TOF signal is from ions reflected off both the trap entrance and the inner barrier, while the small contribution is only from the ions reflected from the inner barrier (green pattern in Figure 6.8). However, the experimental results show that the first signal reached the MCP later than that in the simulation and the TOF signal disappears between 75 - 112 μs.

The lost signal can be explained by the performance of a power supply for the deflector. A high voltage probe was directly connected to measure the output voltage from the power supply. During switching between the injection and extraction voltages, there was a time delay caused by the power supply and an overshoot and an undershoot of the high voltages, as depicted in Figure 6.9. Changing between two set voltages takes approximately 36 μs. The time delay caused the first signal to arrive at the detector about 62 μs after the trigger signal. The overshoot and the undershoot at around 49 μs blocked the extracted beam and caused the discontinuity of the TOF signal. By taking the time delay into account, the histogram in Figure 6.8 illustrates the simulated result that matches the TOF spectrum from the experiment.

Furthermore, matching the simulation result with the TOF signal of the ion reflection provides information of the beam emittance and potential distribution. The calculated r.m.s. emittance of 5.7 π mm·mrad where $x_{\mathrm{rms}} = 0.8$ mm and $x'_{\mathrm{rms}} = 7.7$ mrad is close

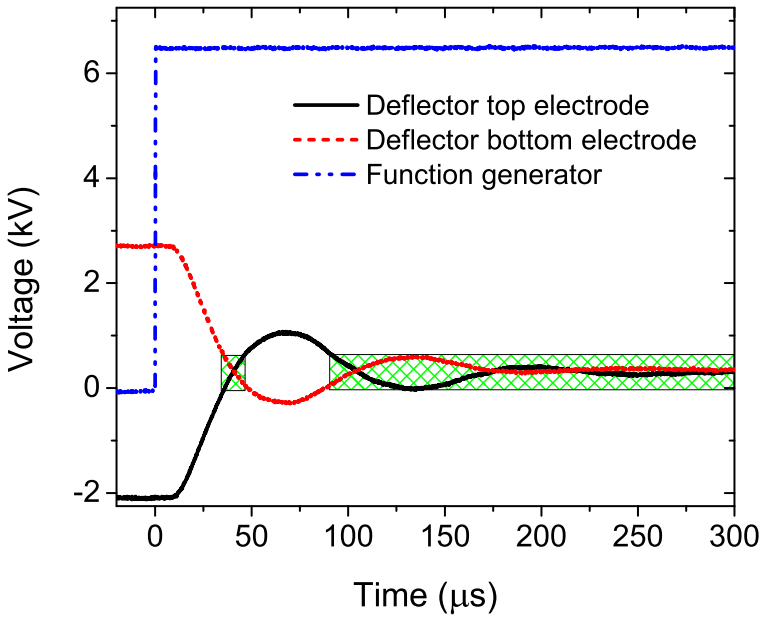

Figure 6.9 Time delay for changing between injection and extraction voltages of the deflector top (black) and deflector bottom (red) electrodes and signal from the function generator (blue). The pattern area indicates a range of voltage that allows the ion beam transport based on the experiment.

to the upper bound of the emittance measured in Section 6.1 where the r.m.s. of the beam size is 1.6 mm wide.

To determine the effective space-charge potential created by the electron beam, the experiment was setup similar to the study of the ion reflection. The TOF signals of K^+ were recorded both when the electron beam was off and on.

Figure 6.10a shows the TOF signal of K^+ when the electron beam was off and the simulation results that match to the TOF signal. The TOF signal starts around 57 μs and the shape of the signal may result from the combination of the inhomogeneous magnetic field and the potential distribution in the trap. In this measurement, an effect from the undershoot and the overshoot after switching high voltage for the extraction and the injection was not observed. The possible reason was that, with this setting, the beam spot detected by the MCP at BOB 4 moved on the MCP screen when the voltage changed from the undershoot and the overshoot. Therefore the MCP could still detect the ions even though the voltages were in the undershoot and overshoot ranges.

In Figure 6.10b, the TOF signal was experimentally recorded when the 19.5 keV and 90 mA electron beam was on and the histogram showed the result simulated with the same electron beam current and energy. It is obvious that the histogram does not match to the experiment. The ions in the simulation travel faster than the real ions in the trapping region.

To obtain consistent results between the experiment and the simulation, displayed in Figure 6.10c, the electron beam current used in the simulation was reduced to 25 mA providing approximately 25 V on the electron beam axis. Since the ions that mostly travel inside the electron beam are further ionized to 2+ charge state, the TOF signal of K^+

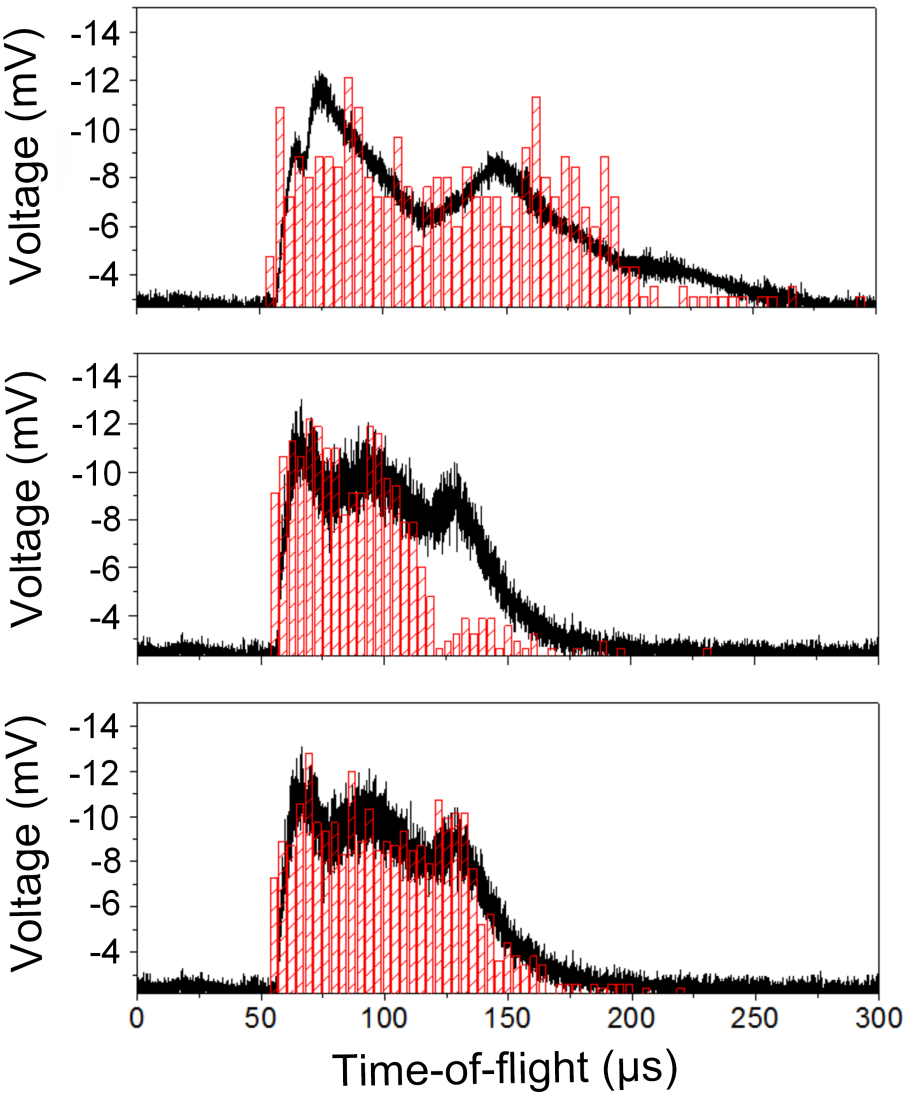

Figure 6.10 TOF spectra of ion reflection and simulated histograms without the electron beam (a), with the 19.5 keV and 90 mA electron beam for both simulation and experiment (b), and with the 19.5 keV and 90 mA electron beam for experiment and the 19.5 keV and 25 mA for the simulation (c).

detected at BOB 4 is mainly from K^+ that travel around the electron beam. The effective space-charge potential that these ions see from the 90 mA electron beam is equivalent to the space-charge potential created by a uniformly distributed electron beam of 25 mA.

6.3 Dependency of the total efficiency on ion and electron beam currents, trap size, and trap depth

As mentioned in Chapter , the capture efficiency contributes to the total efficiency. There are several parameters involved in the capture efficiency, for example, electron beam current, electron beam energy, trap size, trap potential depth, magnetic field configuration, barrier location, etc. However, only three dominant parameters: electron beam current, trap size, and trap potential depth, were investigated.

The capture efficiency can be obtained from the total efficiency using Eq. **??**. The results from the ion reflection study support that the injection and transport efficiencies of K^+ are almost 100%. For ions with higher charge states which are more confined to the electron beam axis, 100% of the extraction efficiency can be expected. The breeding efficiency is also 100% since the total current is calculated from currents of all charge states. Therefore, the capture efficiency is equal to the total efficiency.

The EBIT total efficiency is computed from the current of HCIs recorded after the Q/A separator and divided by the injected beam current from the test ion source recorded at BOB 1 (see Figure 6.4);

$$\epsilon_{\mathrm{tot}} = \frac{\sum_{\mathrm{i}} I_{\mathrm{i}}/\mathrm{i}}{I_{\mathrm{inj}}}, \tag{6.1}$$

where I_i is the electric current of a charge state i and I_{inj} is the injected current. The

measurement to determine the capture efficiency has been performed by following steps:

1. Inject the K^+ beam from the test ion source and measure the beam current at BOB 1 (see Figure 6.4).

2. Remove the Faraday cup, let the beam travel to the EBIT and be charge bred for a desired period of time, normally between 20 - 500 ms.

3. Extract the HCIs through the collector by lowering the outer potential barrier and adjust the Q/A separator to accept highly charged potassium.

4. Start a Q/A scan to record a current of HCIs ejected from the EBIT.

5. Repeat the same process but vary the following parameters:

   (a) Injected ion beam current.

   (b) Electron beam current.

   (c) Trap size defined by the length between LTC11 or the outer barrier and the inner barrier which varies from LTRAP, LTE1, and LTE4, see Appendix B.1.

   (d) Ion energy in trapping region defined by the total trap depth.

For the study of the efficiency on the electron beam current, re-optimization of voltage setting for each measurement was required since the total potential changed with electron beam current. The focusing of the injected ion beam changed as well. For mapping out other interested parameters, the optimizations were not necessary for each step.

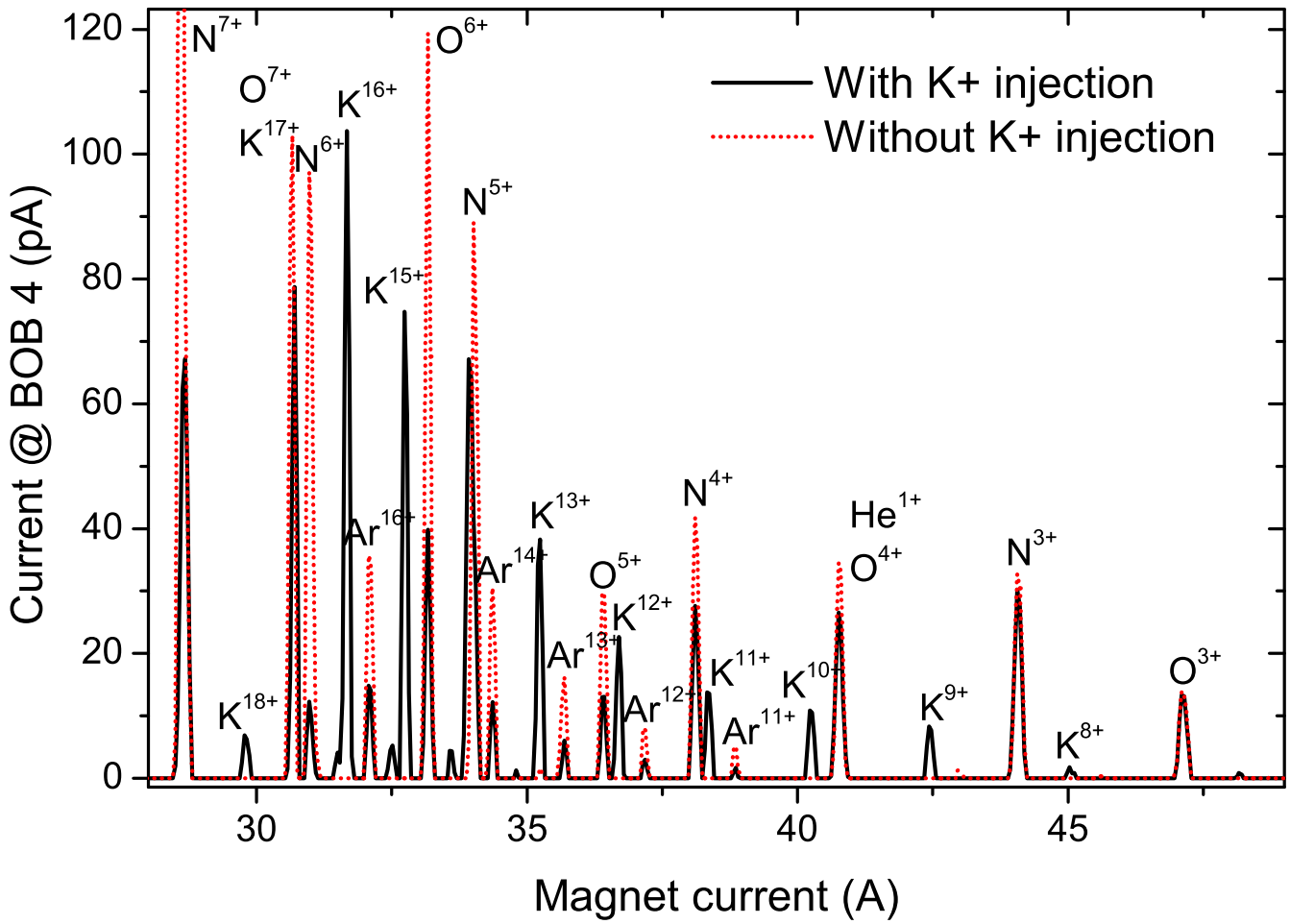

Figure 6.11 Q/A spectra of the ion beam extracted from the EBIT with a 5 Hz repetition rate, an electron beam current of 126 mA, and a 19.5 keV electron beam energy. The spectra with and without the external injection of K^+ are shown in black and red dotted curves, respectively.

Figure 6.11 displays typical Q/A spectra recorded at the BOB 4 Faraday cup. Not only do the spectra contain elements from the injected beam, but they also provide information about beam contamination from residual gases inside the trapping region, mainly C, N, O, Ar, and Ne. Ba ions from the electron cathode sometimes were seen in the Q/A spectrum. By comparing the spectra with and without external injection, we can distinguish the peaks of highly charged potassium ions.

6.3.1 Capture efficiency vs injected ion beam current

The capture efficiency was investigated for different injected beam currents. Since the peak of K^{16+} in Figure 6.11 is well isolated from peaks of highly charged background ions, K^{16+} is a good choice for studying the capture efficiency. Figure 6.12 displays the particle current of K^{16+} as a function of injected beam current. By using an attenuator, the injected beam current was reduced by factors of 10 and 100. The detected beam current rose linearly at small injected beam current. The efficiency to charge breed into K^{16+}, illustrated in Fig 6.13, is calculated from the ratio of the particle current of K^{16+} to the injected current. We see that the efficiency is constant at small incoming beam current and drops at high incoming current. The reason is that the trap was saturated by highly charged ions of the injected beam.

For an electron beam of 135 mA and 19.5 keV and the 0.64 m trap, the charge capacity is about 1 nC, equivalent to an extracted beam current of 1 nA at 1 Hz repetition rate. Due to the injected beam of 1.4 nA, a large portion of the beam was not captured and charge bred, so the capture efficiency was reduced.

The trap capacity was investigated through the extracted beam currents. The total

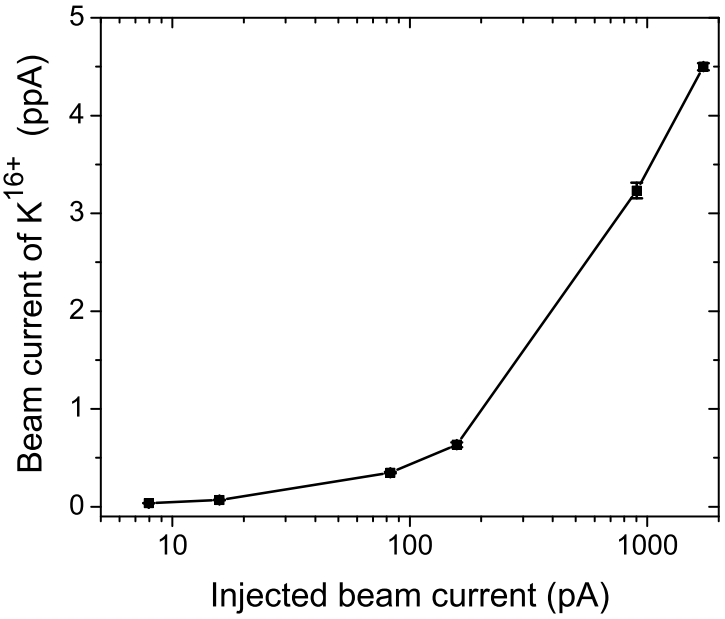

Figure 6.12 Beam current of K^{16+} detected at BOB 4 with different injected beam currents.

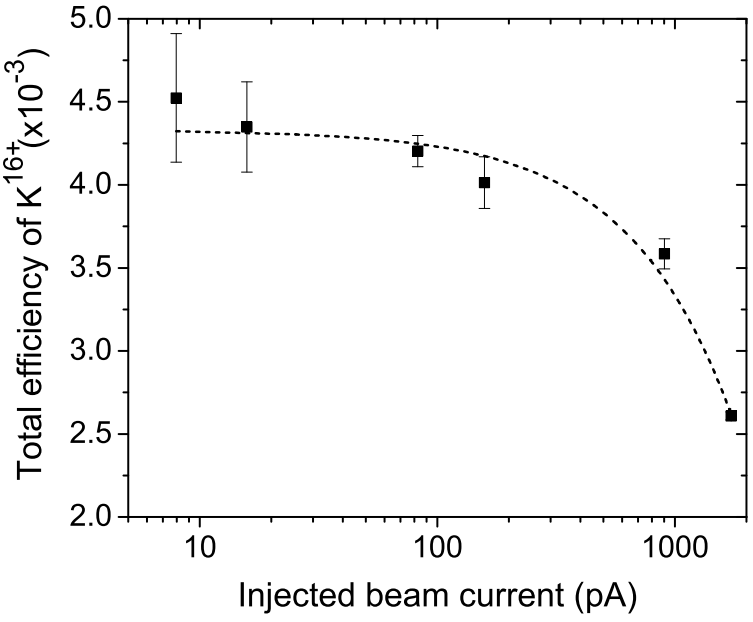

Figure 6.13 Total efficiency of charge breeding into K^{16+} charge state with different injected beam currents.

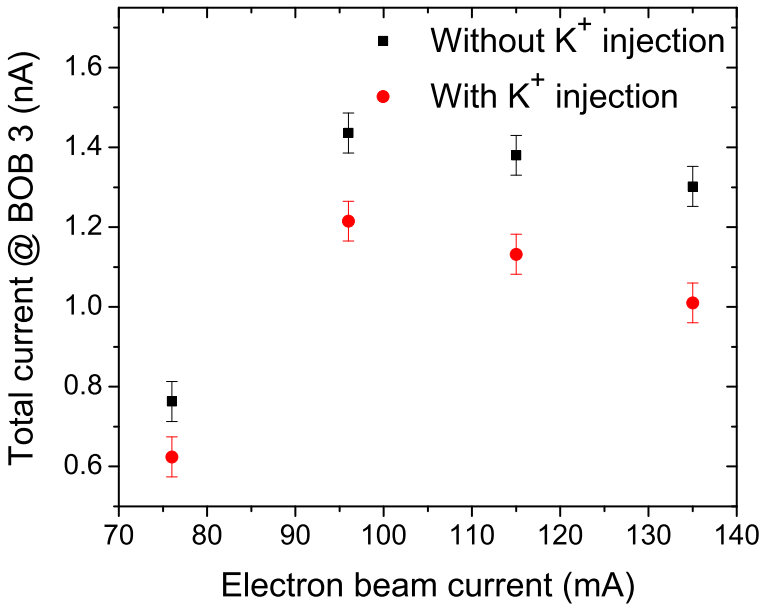

Figure 6.14 Comparison of total beam currents extracted from EBIT with (red) and without injection of potassium beam (black) at different electron beam currents.

beam current was measured at BOB 3 (see Figure 6.4) before the bending magnet. Figure 6.14 illustrates the total ion beam current as a function of electron beam current with and without external beam injection from the test ion source. The extracted ion current measured with external injection is smaller than that without external injection. Since a potassium ion is heavier than the background ions, the lighter ions gain momentum from ion-ion collisions and, at a certain point, have high enough energy to escape the trap. This explanation is supported by the spectra shown in Figure 6.11 where the peaks of highly charged residual ions are smaller than those without external injection. Therefore, less beam current is extracted after external injection than that without external injection.

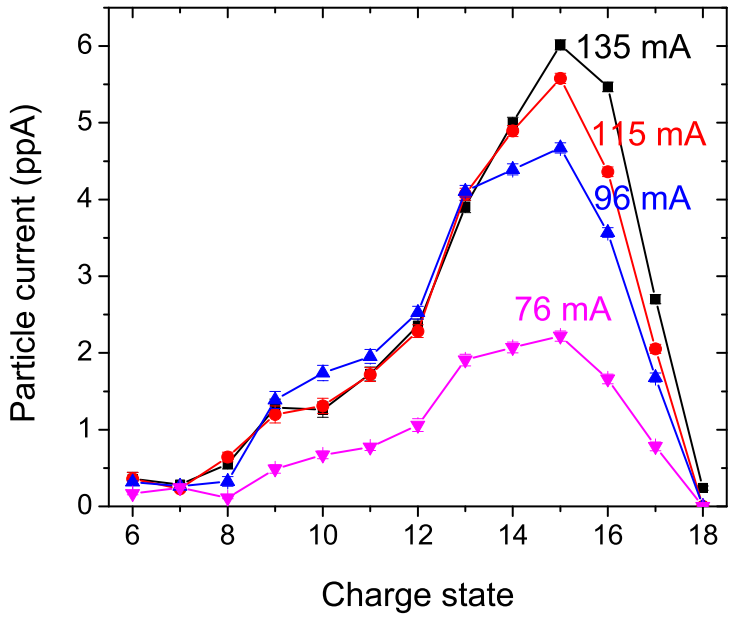

Figure 6.15 A plot showing particle currents at different charge states from electron beam currents of 135 mA (black), 115 mA (red), 96 mA (blue), and 76 mA (magenta). The ion beam was extracted from the EBIT with a 5 Hz repetition rate.

6.3.2 Capture efficiency vs electron beam current

As seen in Chapter 2.4, the ionization time strongly depends on the electron beam current: the higher the electron beam current, the larger the electron beam current density and the shorter the breeding time. With the short breeding time, injected ions have a higher probability of being charge bred to 2+ or 3+ charge states within a round-trip flight and trapped in the trapping region. The trap capacity is also dependent on the electron beam current, see Eq. 3.1. Figure 6.15 shows particle currents of each charge state at electron beam currents of 135 mA, 115 mA, 96 mA, and 78 mA. For an accumulation time of 200 ms, K^{15+} dominated in the trap and the ejected currents increased with electron beam currents.

A comparison between simulation and experimental capture efficiencies is depicted in

Figure 6.16. The simulated capture efficiencies are taken from Section 5.5.3 with emittance ranging between 1.4 - 5.5 πmm·mrad. The maximum total experimental efficiency of 2.3 $\pm$ 0.1 % was obtained at the electron beam current of 135 mA. The error bar was mainly from the fluctuation of the read current. However, considering the range of the injected beam emittance, the error bar can be larger than 0.1%. At 76 mA, the experimental efficiency is smaller than the trend of capture efficiency of higher electron beam currents because the voltage setting was not well optimized while recording currents of HCIs. From the simulation, the highest efficiency was reached for a 135 mA electron beam current. The comparison between simulated and experimental efficiencies shows an overprediction by a factor of seven even though they illustrate the same trend. The difference between the experimental and the simulated values can possibly be explained by following reasons; the large range of the measured emittance, the saturation of the trap, the ion beam alignment, and incorrect assumption for the electron beam density. Assuming the beam emittance of 5.5 πmm·mrad, the capture efficiency is still different by a factor of three. Because of injecting too much ion beam, the trap was saturated with highly charged potassium ions as shown in Figure 6.11 and this limitation was not implemented in the simulation. Including this factor to the capture efficiency, the overprediction decreases by a factor of 1.5.

A further simulation was performed to study the effect of misalignment of the injected ion beam to the electron beam axis, as illustrated in Figure 6.17. An electron beam current of 135 mA was used. For an ion beam with an emittance of 3.8 π mm·mrad, the capture efficiency drops by factors of 1.2 and 2.0 if the ion beam is misaligned by 0.5 and 1.0 mm, respectively. Due to the setup of beamline alignment, the misalignment can be at most 0.5 mm. By combining all three reasons, it is not enough to explain the overprediction factor

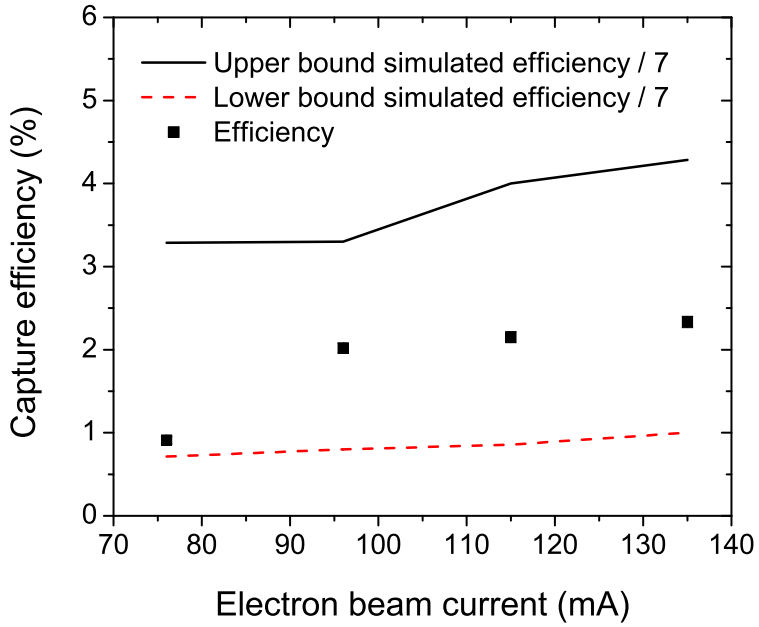

Figure 6.16 Comparison between the simulated capture efficiency ranges (between red-dash and black-solid line) and the experimental (black) capture efficiencies as a function of electron beam currents.

of seven. Therefore the investigation of the electron beam current density is required to reveal the missing overprediction factor and this will be more clarified in Section 6.4.2.

6.3.3 Total efficiency vs trap size

Not only does trap size contribute to the trapping capacity, but it also influences the time ions spend inside the trap. If the ion trajectory overlaps with the electron beam, the ion spends a longer time inside the trapping region and therefore the probability for ionization to K^{2+} or K^{3+} is higher. The schematic of three trap sizes is shown in Figure 6.18. The full trap size (0.64 m) started from the outer barrier (LTC11, see Figure B.1) to the inner barrier (LTE4). The potentials produced by LTE1 and LTRAP were raised to be equal to the potential from LTE4 in order to have 0.51 m and 0.43 m trap sizes, respectively. Figure

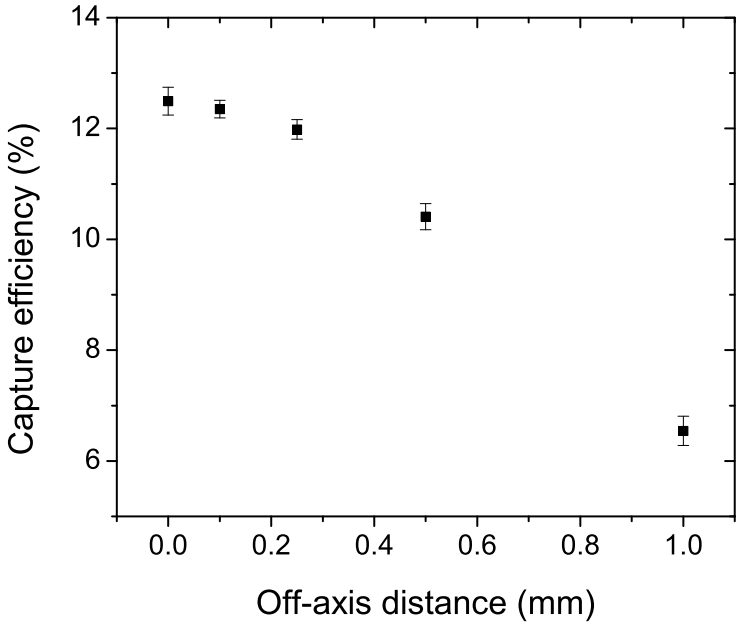

Figure 6.17 Calculated capture efficiency of a beam with an emittance of 3.8 π mm·mrad at 20 keV as a function of distance between an injected beam and an electron beam axis. The electron beam current of 135 mA was used.

6.19 shows experimental particle currents for each charge state for different trap sizes. The total current of highly charged potassium ions rises as the trap size increases.

Figure 6.20 illustrates the comparison between the simulation and experimental capture efficiencies. The simulated capture efficiencies are taken from Section 5.5.3 with the emittance range between 1.4 - 5.5 πmm·mrad. A maximum efficiency of 2.1 $\pm$ 0.1% was obtained from the largest trapping size where an electron beam current of 100 mA was set. Again, the error can be larger based on the range of the measured emittance. Although the simulation and the experimental results evolve in a similar trend, they are still different by a factor of seven. The low capture efficiency can be explained by reasons similar to those mentioned in Section 6.3.2.

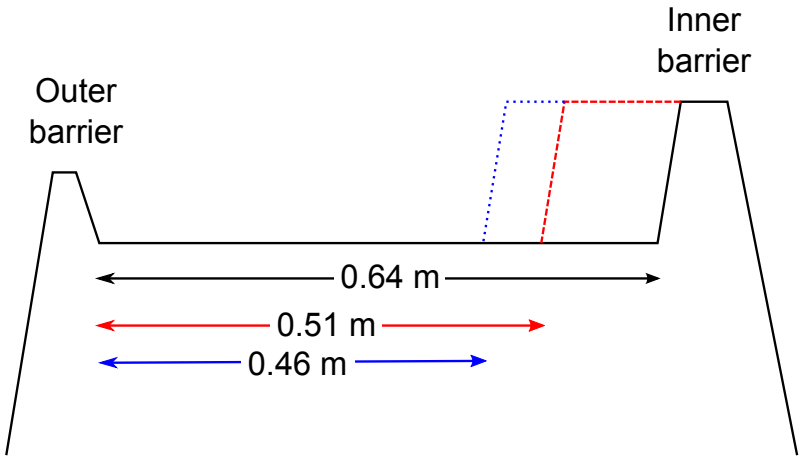

Figure 6.18 Schematic of the trap with different trap sizes.

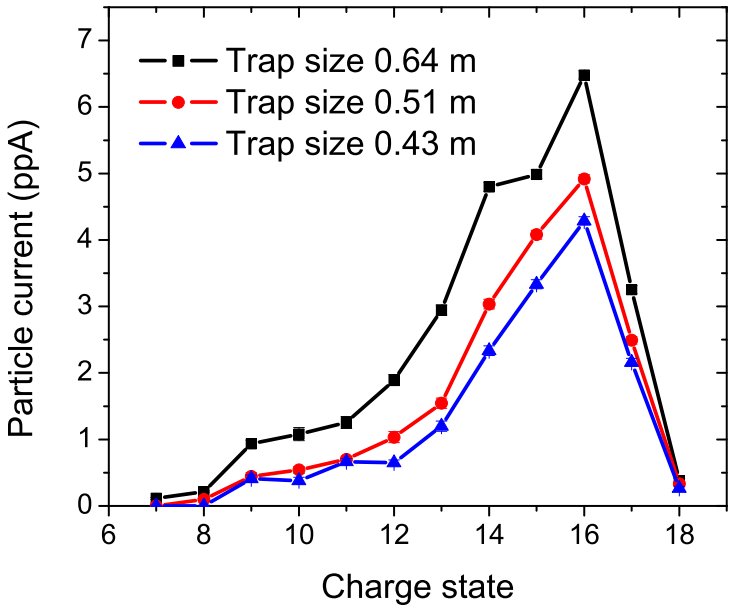

Figure 6.19 A plot showing particle current of each charge state for different trap sizes. The ion beam was extracted from the EBIT with a 5 Hz repetition rate.

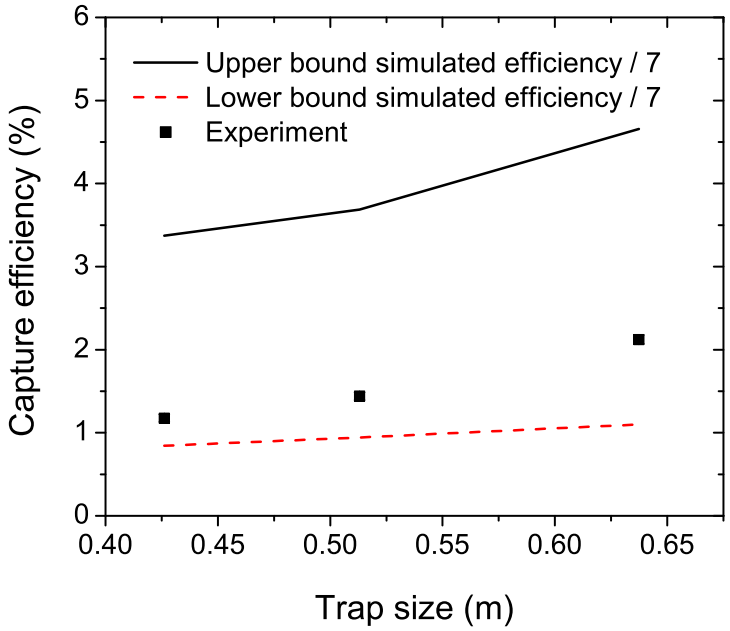

Figure 6.20 Comparison between the simulated capture efficiency ranges (between red-dash and black-solid line) and the experimental capture efficiencies (black) as a function of trapping size.

6.3.4 Total efficiency vs trap depth

The trap depth determines the ion beam's axial energy inside the trap and a deeper potential well leads to higher ion energies. Since high energy ions spend less time in the trap, the probability to be charge bred into K^{2+} or K^{3+} charge state becomes smaller. On the other hand, if the potential is too shallow, K^{2+} ions may be able to leave the trap within a round-trip. In addition, trapped ions may be heated through electron-ion collisions and gain enough momentum to escape the trap [66, 19]. Therefore, the trap potential needs to be optimized. A schematic of different trap depth is shown in Figure 6.21. The negative sign indicates that the trap potential is smaller than the outer barrier.

In this measurement, the electron beam current was set to 120 mA. Figure 6.22 depicts particle currents for several charge states. The experimental results provided the highest

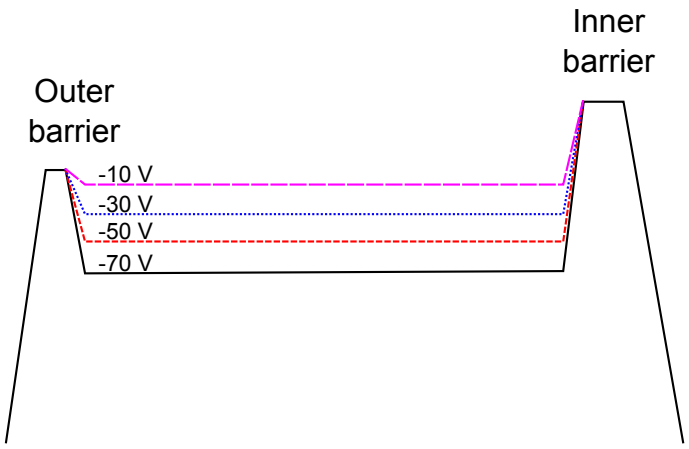

Figure 6.21 Schematic of the trap with different trap potential.

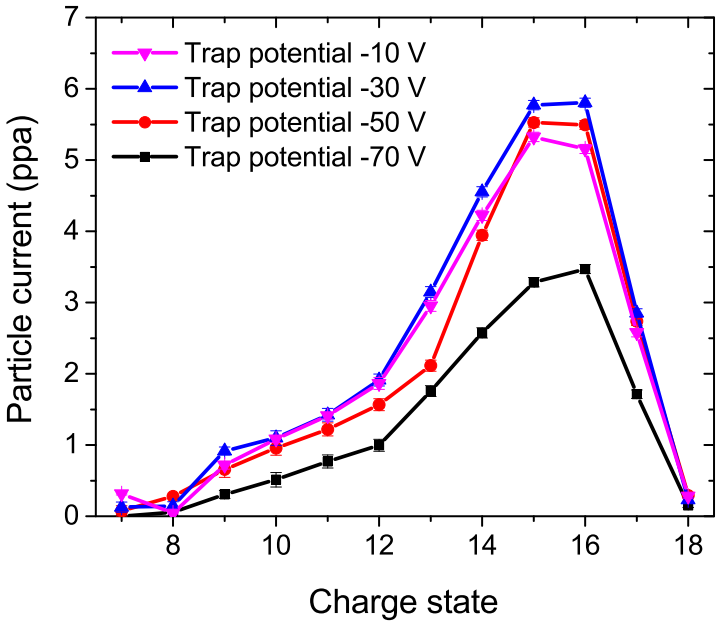

Figure 6.22 A plot showing particle current at different charge states with trap potential of -10 V (magenta), -30 V (blue), -50 V (red), -70 V (black) compared to the outer barrier. The ion beam was extracted from EBIT with 5 Hz repetition rate.

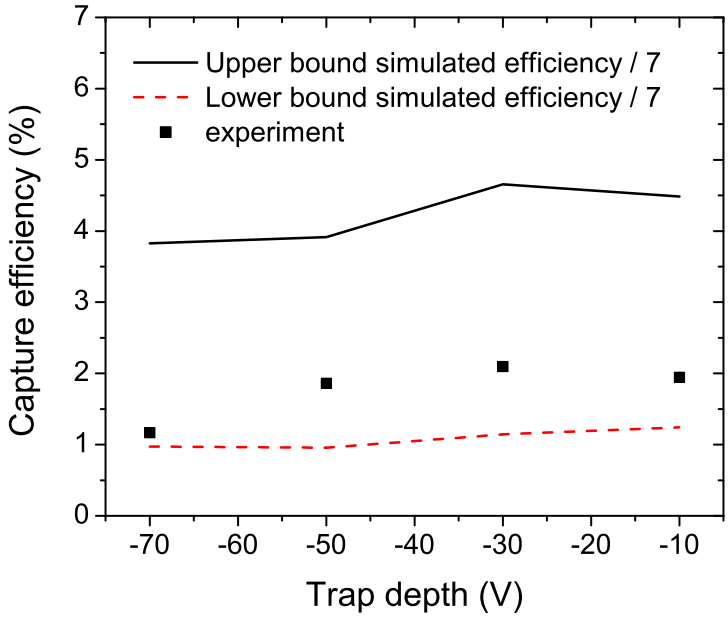

Figure 6.23 Comparison between the simulated capture efficiency ranges (between red-dash and black-solid line) and the experimental (black) capture efficiencies as a function of trap depth. The simulated values are calculated based on the 20 keV ion beam.

and the lowest ion yields when the trap depth was set to -30 V and -70 V, respectively. Figure 6.23 displays a comparison between simulation and experimental capture efficiencies. The simulated capture efficiencies are taken from Section 5.5.3 with the emittance range between 1.4 - 5.5 πmm·mrad. The experimental efficiency increased when the trap depth changed from -70 V to -30 V and dropped down when the trap depth was -10 V. The maximum efficiency of 2.1 $\pm$ 0.1 % was acquired when the trap depth was -30 V. At -10 V, the experimental efficiency was lower than that of -30 V while the calculated efficiency at -10 V was larger than that of -30 V. The reason is, in the experiment, the trapped ions may be heated up by the electron-ion collisions and have enough kinetic energy to escape the shallow trap while this collision is excluded in the simulation. Therefore, the trap depth has to be optimized to avoid losing ions via this process.

6.4 Study of the charge breeding process

Understanding the charge breeding process is very important for the operation of the EBIT. The highest abundance of the specific charge state can be obtained by charge breeding ions within a proper time interval. The comparison between the calculated and the experimental charge breeding times also provides information about the effective electron beam current density, which indirectly helps determine how well the ion beam overlaps with the electron beam.

6.4.1 Charge state evolution and charge breeding time

Figure 6.24 depicts mass-over-charge spectra for different accumulation times of highly charged potassium. By scanning the dipole magnet current, ions with different A/Q ratios extracted from the EBIT were detected. The abundance of each ion and charge state is dependent on the accumulation time. For several accumulation times, the evolution of the abundances can be observed. As the accumulation time increases, the highest abundance of a certain A/Q ratio changes from the higher to the lower ratio.

Without considering the radiative recombination and charge exchange processes, the calculated charge state evolution of potassium based only on the EI process is plotted in Figure 6.25. The rate equation, see Eq. 2.17, is numerically solved with the following initial conditions: an electron beam current density of 500 A/cm^2 and the EI cross section calculated for the 19.5 keV electron beam energy. The calculation assumes that the ion beam trajectory entirely overlaps with the electron beam. When compared between experimental and calculated results, the optimum time giving the highest abundance is significantly

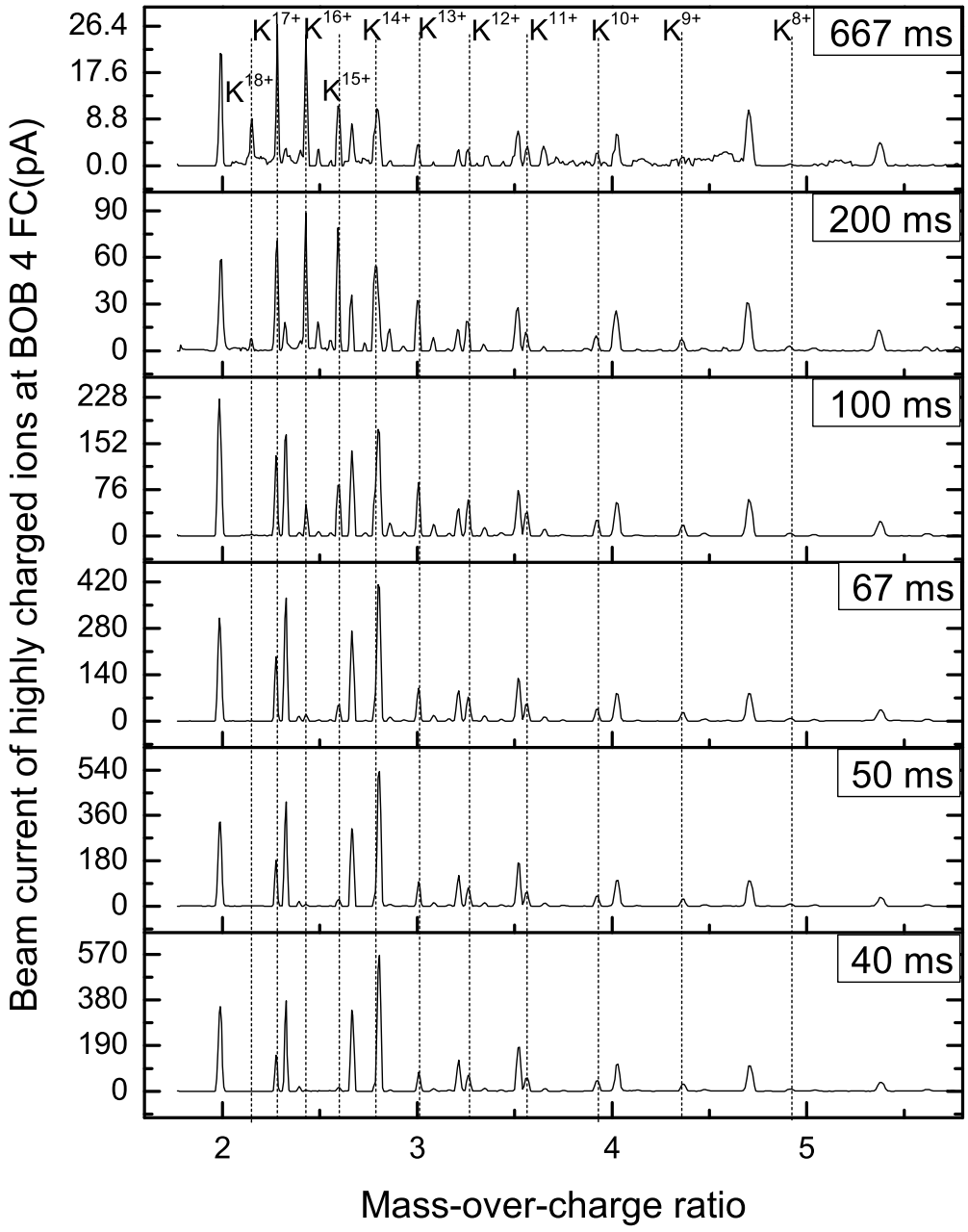

Figure 6.24 Mass-over-charge spectra of highly charged potassium obtained by scanning the bending magnet current for different accumulation times. The electron beam current and energy were 125 mA and 19.5 keV.

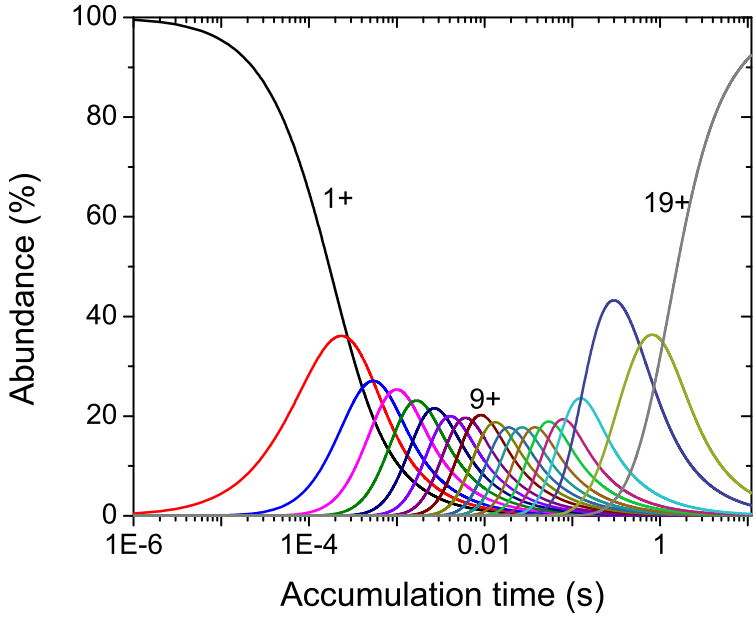

Figure 6.25 Calculated charge state evolution of potassium ions with the continuous injection. The electron beam current density is 500 A/cm^2.

different. The reason is that the ion beam trajectory in the experiment partially overlaps with the electron beam and the ions then need to be charge bred over a longer time into higher charge states. The helium-like potassium, K^{17+}, abundance dominates over the nearby charge states as a result of closed-shell charge breeding where the 17$^{\text{th}}$ and 18$^{\text{th}}$ ionization energies of potassium are 1.03 and 4.61 keV.

6.4.2 Determination of effective current density

An effective electron current density is used to analyze how well the injected ion beam overlaps with the electron beam in the EBIT. If the ion beam completely overlaps with the electron beam, the effective current density is expected to be maximum and identical to the current density of the electron beam. The effective current density is obtained from a comparison between calculated and experimental charge state evolutions. Figure

6.26 illustrates the evolutions of K^{12+} and K^{16+} acquired from the experiment and the calculation mentioned in section 6.4.1. K^{12+} and K^{16+} were selected for the study of effective current density because they show clear peaks in the range of 0.01 to 0.5 ms of accumulation times. The evolution of K^{12+} and K^{16+} were obtained by changing the accumulation time from 16 - 500 ms and setting the magnet currents to allow only K^{12+} and K^{16+} to the detector. The experimental abundances are normalized by the number of particles per pulse. At 16 ms, K^{12+} started to be produced in the trap while there was not significant amount of K^{16+}. K^{16+} appeared when the accumulation time was approximately 40 ms. The optimum accumulation times for charge breeding K^{12+} and K^{16+} are 83 and 251 ms, respectively.

From the rate equation (Eq. 2.17) for an electron beam current density of 500 A/cm^2, the optimum accumulation times providing the maximum abundance of K^{12+} and K^{16+} are 26 and 122 ms, respectively. Since the charge breeding time is inversely proportional to the electron beam current density, the effective electron beam current densities of K^{12+} and K^{16+} are 157 and 243 mA/cm^2. The effective current density is not close to the calculated value of 500 mA/cm^2 where I_e = 125 mA, B = 2 T, and the electron beam density is uniform. The difference can be explained by two possible reasons. Firstly, the ion trajectory does not well overlap with the electron beam. In this situation, K^{16+} ion is more confined and its trajectory better overlaps with the electron beam than that of K^{12+} ion. Secondly, the electron beam may not be uniformly distributed over the its cross section. Due to these arguments, the electron beam at the trap center was further investigated via a simulation by Tricomp [67]. The result of the simulation in Figure 6.27 supports the second argument that the electron beam is not uniformly distributed over its cross section.

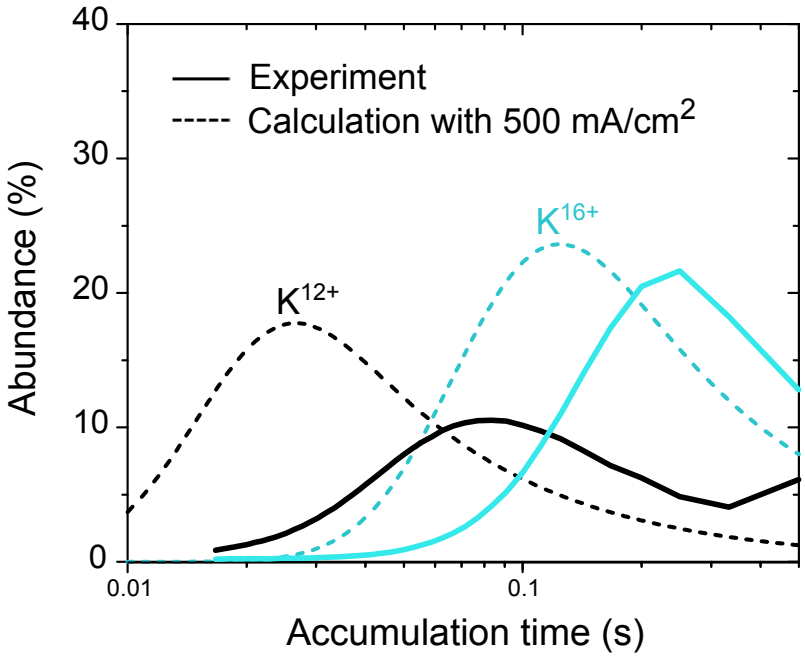

Figure 6.26 Comparison between calculated (dash line) and experimental (solid line) charge state evolutions of K^{12+} (black) and K^{16+} (light blue). The electron beam current and energy were 100 mA and 19.5 keV.

Using this information the small capture efficiency in Section 6.3 can be explained if the K^+ ions travel in the region of low electron beam current density. Assuming that the K^+ ions are mostly in the region where the electron beam current density is about 100 A/cm^2 or less, the value from the NEBIT calculation for this assumption can be significantly decreased and the overprediction may be reduced by a factor of up to five.

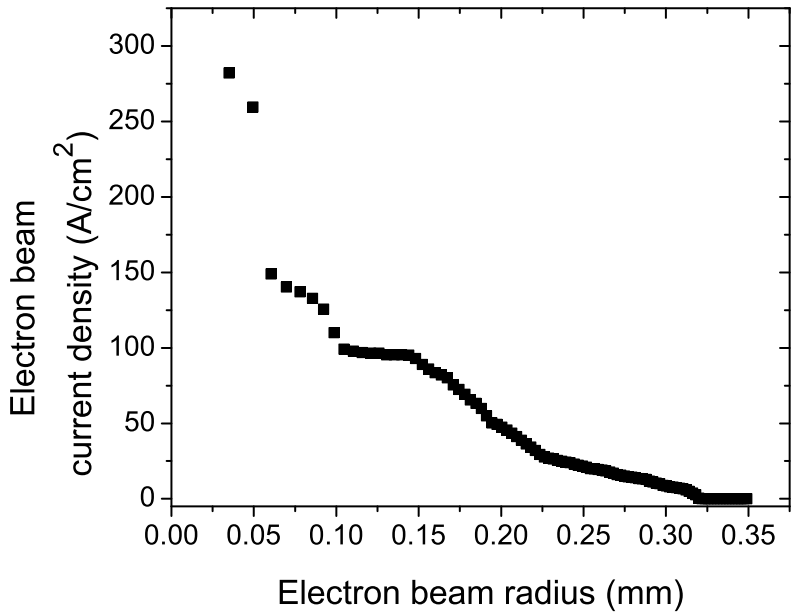

Figure 6.27 Electron beam current density as a function of the electron beam radius simulated by Tricomp.

Chapter 7

Conclusion and Outlook

7.1 Conclusion

The ion capture process inside the EBIT charge breeder was investigated via simulations and experiments in order to understand how the EBIT functions and to maximize the capture efficiency. The NEBIT code was used to calculate the EBIT acceptance and predict the capture efficiency. The current version of NEBIT was upgraded from an earlier version [61] by using the real design of the NSCL EBIT, improving the space charge potential with the electron beam energy correction, using the Monte-Carlo method for ion selection, and importing more realistic electric fields from SIMION. The NEBIT code was validated to provide the reasonable results after being tested with the concept of conservation of energy and compared to the analytical formula, CBSIM program, and the previous version of NEBIT. With the design parameters of the 2.5 A electron beam current and the 1T-6T magnetic field configuration, NEBIT demonstrated that it is possible to attain capture efficiency of more than 80% for an injected ion beam with an emittance of less than 10 π mm·mrad. NEBIT was also used and will help optimizing the voltage setting. It can predict the capture efficiency based on the setup used in the experiment.

The EBIT was experimentally setup with the 2T-2T magnetic field configuration and an electron beam of 19.5 keV. A K^+ beam of 20 keV from the test ion source was used to

study the EBIT capture efficiency. The emittance of the K^+ beam was measured by the quadrupole scan method. The voltage setting to efficiently transport the ion beam into the trap was optimized by minimizing the radial energy pickup and observing the TOF signal of ion reflection. The behavior of the electron beam in the trap was deduced from the TOF signal of ion reflection when the electron beam existed. The capture efficiency was studied through variations of the injected ion beam current, electron beam current, trap size, and trap potential depth. From the evolution of highly charged potassium, the effective current density of the electron beam was experimentally extracted for K^{12+} and K^{16+}.

From the comparison of simulations and experiments, the capture efficiencies were found to be overpredicted by a factor of seven. The overprediction is mostly due to the electron beam current density which is assumed to be uniformly distributed in the simulation while it is actually not in the real experiment.

7.2 Outlook

As the NEBIT code can be used to calculate the capture efficiency for the EBIT, there is still room for improvement, for example, importing the self-electric field generated by the charged particles from a separate code. This modification will make the calculation much faster. Besides the EI process, the other processes such as radiative recombination, charge exchange, electron heating, etc. can be added. For a simple calculation of the capture efficiency, it is enough to include only the EI process but in the experiment, the cycle period is in the scale of tens to hundreds of milliseconds in which the HCIs can be influenced by other processes. With the addition of these processes, the NEBIT code will be able to provide more realistic prediction of the capture efficiency.

The experiment can also be improved by running the EBIT with a higher electron beam current than 135 mA. During the time these measurements were performed, the electron gun could only provide the electron beam current of up to 150 mA. After being modified, the electron gun could produce up to 800 mA electron beam current. At this electron beam current, the EBIT acceptance was significantly larger than the emittance of the injected ion beam. The capture efficiency, which was not limited by the emittance of the injected ion beam, achieved 30% closed to the predicted value. With this capture efficiency, it strongly confirms that the NSCL EBIT is a good charge breeder for rare isotope beams. In addition to high electron beam current, the electron beam current density must be maximized and made uniform within the a certain radius in order to succeed in fast charge breeding.

Finally, this thesis provides useful information from both simulation and experimental aspects for the EBIT and EBIS charge breeder community. The NEBIT code can be used to predict the capture efficiency and understand the detailed behavior of ions in the EBIT. The experimental results can help guide and be a good lesson for the EBIT charge breeder operation to reach the highest total efficiency.

APPENDICES

Appendix A

Transfer matrix for a triplet

The transfer matrices as a function of the quadrupole voltage can be extracted from SIMION by the following steps;

1. Create an instance in SIMION containing a quadrupole triplet and an MCP screen and fly two particles in vertical and horizontal axis with a small radius and angle.

2. Record initial and final positions and velocities then calculate the transfer matrix components.

3. Plot the transfer matrix entries as a function of voltage applied to quadrupole A, B, or C and linearly fit to extract the transfer matrix as a function of voltage.

To simplify the calculation, only the first order transfer matrix is considered. Therefore, trajectories of test ions are chosen to be close to the axis in order to avoid an effect of higher order terms. Furthermore, the determinant of the transfer matrix has to be unity. Two 20 keV test ions were injected into the quadrupole triplet with the following initial conditions: $x_1, y_1 = 0$ mm, $x_1', y_1' = 3.3$ mrad, $x_2, y_2 = 1.8$ mm, and $x_2', y_2' = 0$. The example of the transfer matrix elements, see Eq. A.2, of the quadrupole triplet and the drift space to the MCP screen in vertical and horizontal axes are displayed in Figure A.1. The transfer matrices were linearly fitted as a function of voltages applied to the quadrupole A. The transfer matrix elements were also calculated when altering voltages applied to the

quadrupole B and C. The emittance can finally be extracted from the quadratic equation, containing the transfer matrix elements,

$$\begin{aligned}\sigma'_{11} = &(VA_1 + A_2)((VA_1 + A_2) \cdot \sigma_{11} + (VB_1 + B_2) \cdot \sigma 12) \\ &+ (VB_1 + B_2)((VA_1 + A_2) \cdot \sigma_{12} + (VB_1 + B_2) \cdot \frac{\epsilon^2 + \pi^2 \sigma_{12}^2}{\pi^2 \sigma_{11}})\end{aligned} \tag{A.1}$$

with A_1, A_2, B_1, and B_2 being constants in the following transfer matrix,

$$\mathcal{M} = \begin{pmatrix} VA_1 + A_2 & VB_1 + B_2 \\ VC_1 + C_2 & VD_1 + D_2 \end{pmatrix}. \tag{A.2}$$

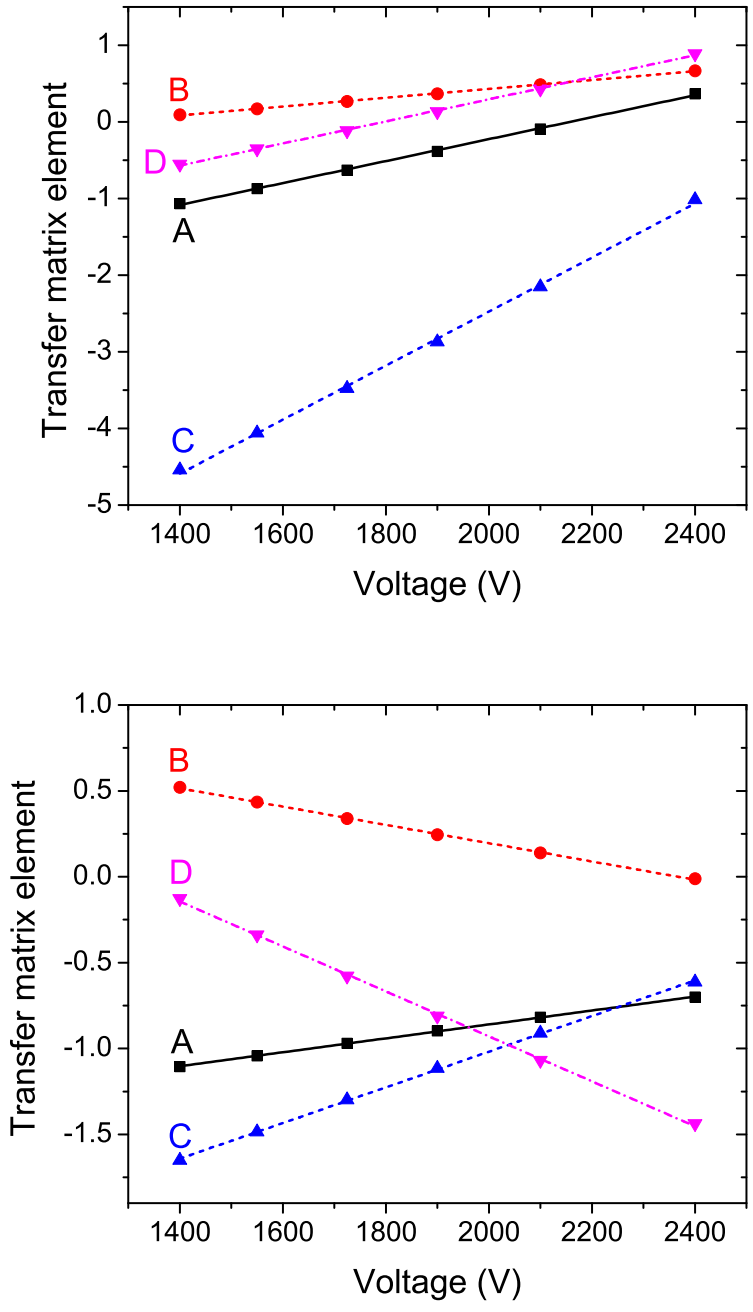

Figure A.1 Transfer matrix elements; A (black), B (red), C (blue), and D (magenta), in horizontal (left) and vertical (right) axes as a function of applied voltage to the quadrupole A.

Appendix B

Voltage distribution

Electrode	Voltage (kV)
Injection tube	0
Acceleration electrode	45.8
Outer lens	45.8
Inner lens	45.8
Extraction endcap	50
Collector	52
Suppressor	51.5
Trap endcap	53
Transfer lens	53.8
Trumpet	56.2
TC13	57.5
TC12	59.5
Outer barrier (TC11)	59.9
TC10-TC1	59.9
Main trap	59.9
TE1	59.9
TE2-TE4	59.9
Inner barrier (TE5)	0
TE6-TE7	0

Table B.1 List of voltages used in SIMION and the NEBIT code to test the conservation of energy along the ion trajectory described in section 5.4.1.

Electrode	Voltage (kV)	
	100 mA	6T6T-1A
Injection tube	0	0
Acceleration electrode	45.8	45.8
Outer lens	45.8	45.8
Inner lens	45.8	45.8
Extraction end cap	50	50
Collector	52	52
Suppressor	50.5	51.5
Trap endcap	53	53
Transfer lens	54	54
Trumpet	56	56.5
TC13	58	58
TC12	58.5	59.2, 58.5
1st barrier (TC11)	59.8	60
TC10-TC1	59.5	59.5
Main trap	59.5	59.5
TE1-TE4	59.5	59.5
2nd barrier (TE5)	65.4	65.4
TE6-TE7	65.4	65.4

Table B.2 The voltage setting for a test of geometrical acceptance with the NSCL EBIT system described in section 5.4.2. For the electron beam current of 100 mA, the settings for 1T-6T and 6T-6T configurations are the same. For the electron beam current of 1 A, the TC12 element is set to be 59.2 and 58.5 kV for the 1T-6T and 6T-6T configurations.

Electrode	Voltage (kV)
Outer barrier (TC11)	62.5
TC10-TC1	60.5
Main trap	60.5
TE1-TE4	60.5
Inner barrier (TE5)	62.5

Table B.3 List of voltages used in NEBIT to calculate the charge state evolution.

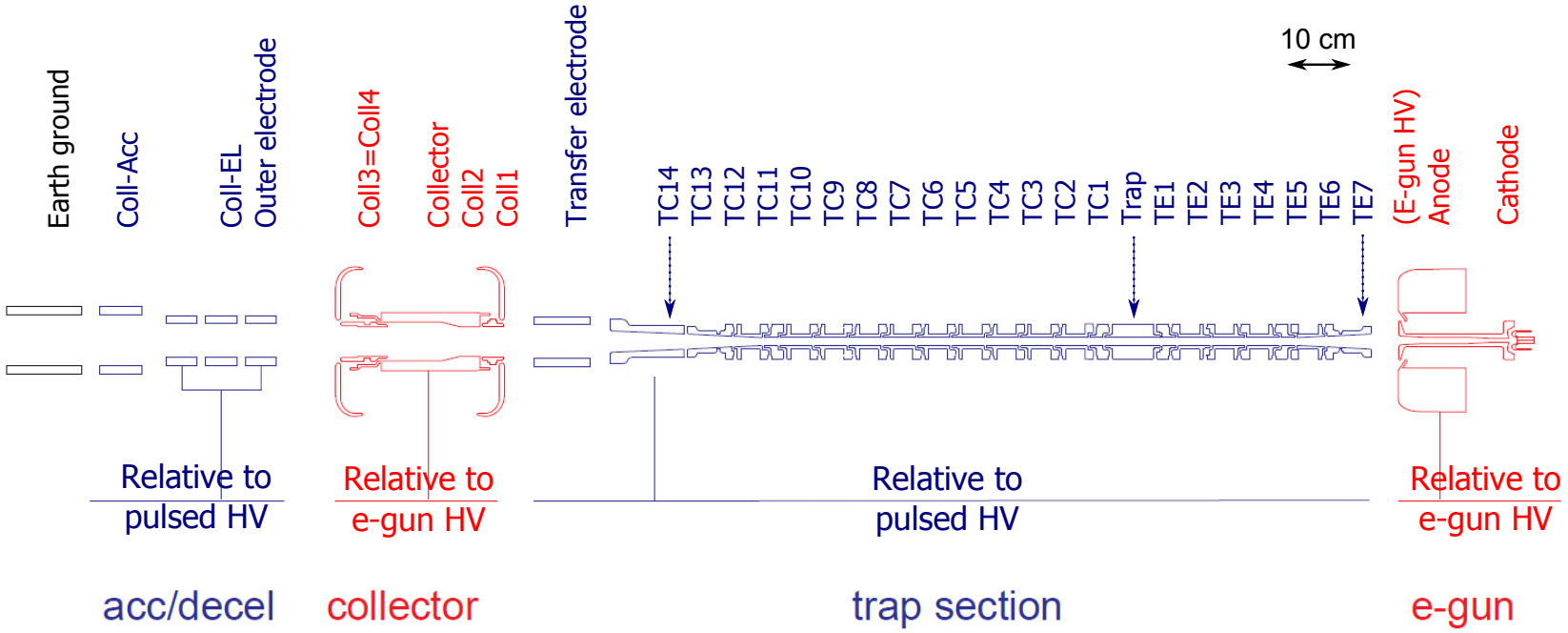

Figure B.1 Power supply schematic for the EBIT. Except an earthground, all elements are floating on an EBIT high voltage platform. To control the electron beam, the electron gun and the collector are biased up to 20 kV on top of the EBIT high voltage platform.

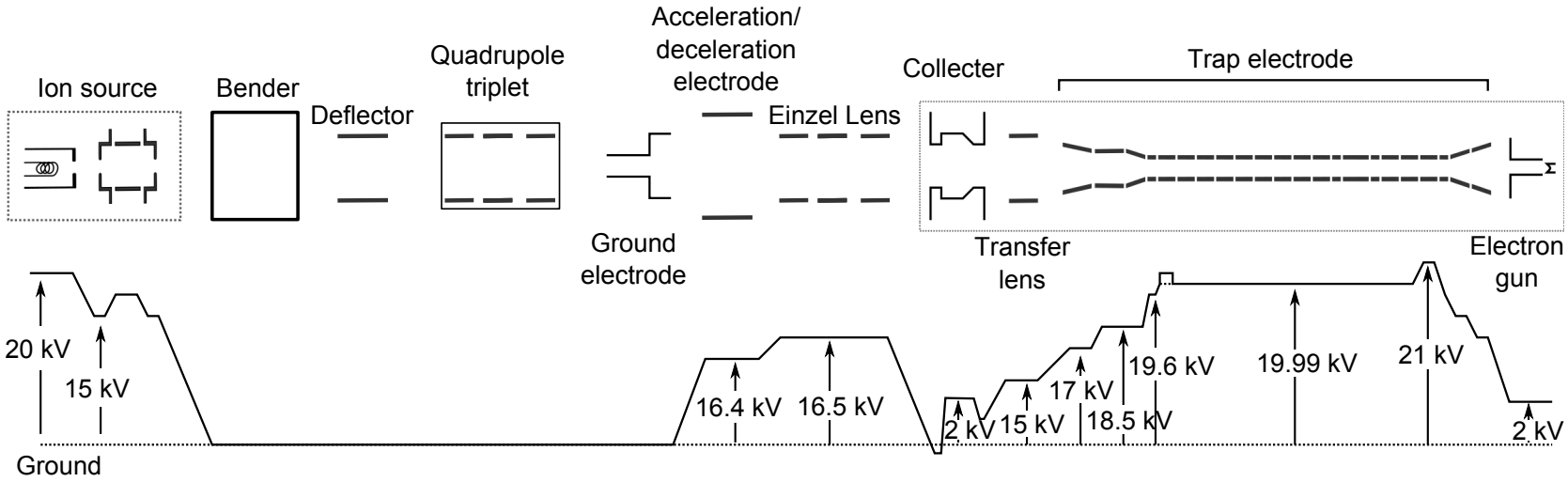

Figure B.2 Schematic of voltages applied to each element.

Appendix C

Ion source simulation

The simulation of the test ion source was performed to investigate the production of K^+ in the ion source chamber. Figure C.1 shows a series of locations where the K^+ are produced from the filament. The top figure illustrates the geometry of the filament and six figures at the bottom display the trajectories of ions created at different locations of the filament. The filament is modeled with small rings and ions are generated around the ring with initial energy of 0.01 eV. The ions are driven by the electric field between the filament and the anode. Voltages applied to the filaments varies from 2 - 9 V based on the valued read from the power supply during the experiment. The anode voltage was set to zero compared to the filament. The extraction electrode and the focusing lens were set to -1.57 kV and -4.80 kV, respectively.

From the simulation, K^+ ions extracted from the ion source were generated from the filaments at location 4 - 6 where they were supplied by 6, 7.5, and 9 V, respectively.

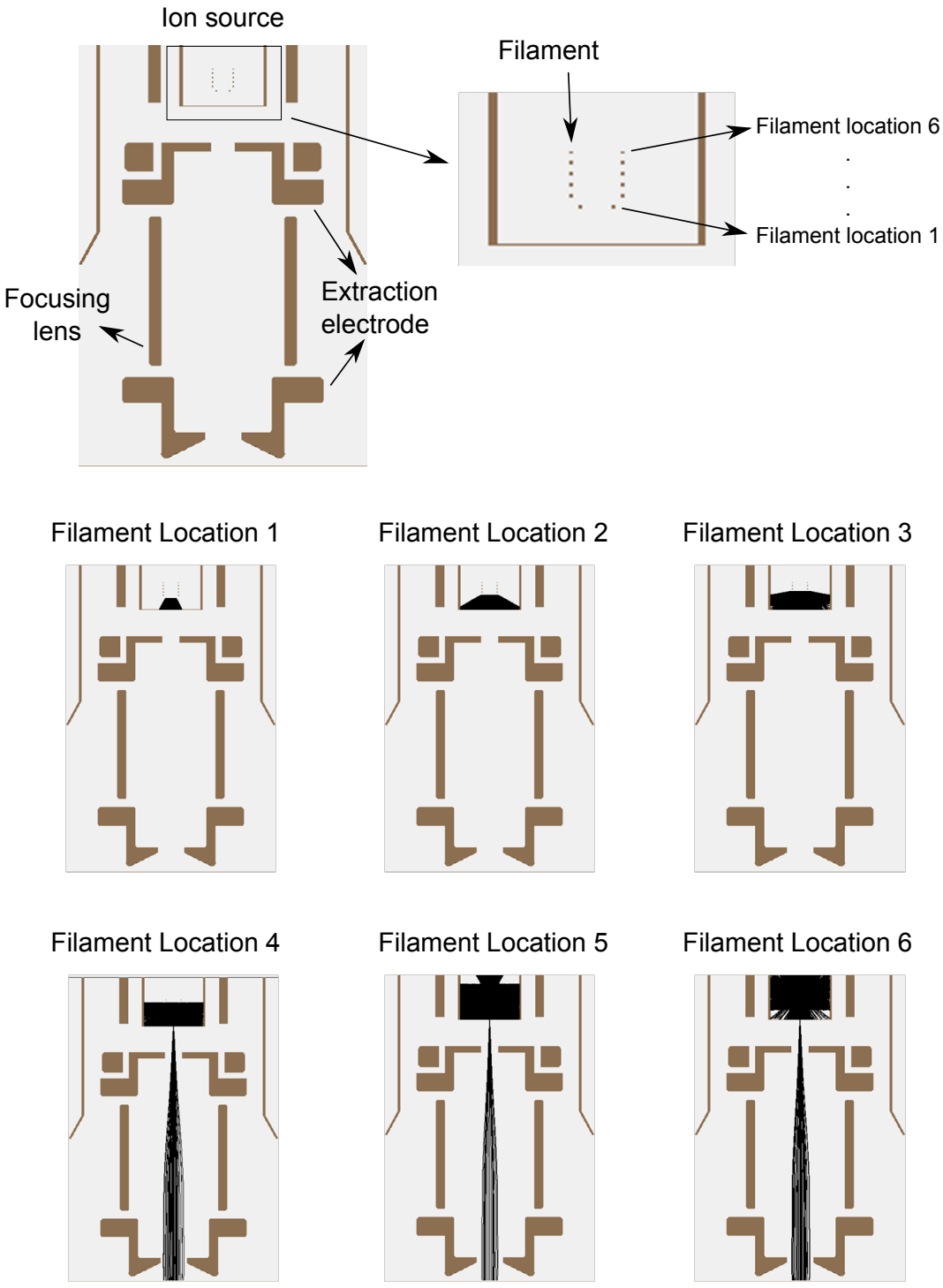

Figure C.1 Simulation of ion production inside the test ion source.

BIBLIOGRAPHY

BIBLIOGRAPHY

[1] S. Schwarz, G. Bollen, D. Lawton, P. Lofy, D. J. Morrissey, J. Ottarson, R. Ringle, P. Schury, T. Sun, V. Varentsov, and L. Weissman. The low-energy-beam and ion-trap facility at NSCL/MSU. *Nucl. Instrum. Meth. B*, 204:507, 2003.

[2] R. Ringle, P. Schury, T. Sun, G. Bollen, D. Davies, J. Huikari, E. Kwan, D.J. Morrissey, A. Prinke, J. Savory, S. Schwarz, and C. Sumithrarachchi. Precision mass measurements with LEBIT at MSU. *Int. J. Mass Spectrom.*, 251(23):300, 2006.

[3] K. Minamisono, P.F. Mantica, A. Klose, S. Vinnikova, A. Schneider, B. Johnson, and B.R. Barquest. Commissioning of the collinear laser spectroscopy system in the BECOLA facility at NSCL. *Nucl. Instrum. Meth. A*, 709:85, 2013.

[4] F. Wenander. Charge breeding techniques. *CERN-AB-2004-035.*

[5] A. Bracco and A. Pisent. SPES technical design for an advanced exotic ion beam facility at LNL. *SPES Technical Design Report, LNL-INFN*, 181/02, 2002.

[6] T. Thuillier, T. Lamy, P. Sortais, P. Suominen, O. Tarvainen, and H. Koivisto. A-PHOENIX, an electron cyclotron resonance ion source for the SPIRAL2 facility. *Nucl. Instrum. Meth. A*, 77(3):03A323, 2006.

[7] F. Ames, R. Baartman, P. Bricault, K. Jayamanna, M. McDonald, M. Olivo, P. Schmor, D. H. L. Yuan, and T. Lamy. Charge state breeding of radioactive ions with an electron cyclotron resonance ion source at TRIUMF. *Rev. Sci. Instrum.*, 77(3):03B103, 2006.

[8] P. Delahaye, C. J. Barton, K. Connell, T. Fritioff, O. Kester, T. Lamy, M. Lindroos, P. Sortais, G. Transtromer, and F. Wenander. Recent results with the Phoenix booster at ISOLDE. *Rev. Sci. Instrum.*, 77(3):03B105, 2006.

[9] S. C. Jeong, M. Oyaizu, E. Tojyo, H. Kawakami, H. Ishiyama, H. Miyatake, K. Enomoto, Y. Watanabe, I. Katayama, T. Nomura, M. Matsuda, A. Osa, and S. Ichikawa. Test results of 18 GHz ECR charge breeder for KEK-JAERI RNB facility. *Rev. Sci. Instrum.*, 75(5):1631, 2004.

[10] R. Vondrasek, A. Kolomiets, A. Levand, R. Pardo, G. Savard, and R. Scott. Performance of the Argonne National Laboratory electron cyclotron resonance charge breeder. *Rev. Sci. Instrum.*, 82(5):053301, 2011.

[11] T. Lamy, J. C. Curdy, R. Geller, C. Peaucelle, P. Sol, P. Sortais, T. Thuillier, D. Voulot, K. Jayamanna, M. Olivo, P. W. Schmor, and D. Yuan. Charge breeding method results with the PHOENIX booster ECR ion source. *EPAC proceeding*, page 1724, 2002.

[12] F Wenander. Charge breeding of radioactive ions with EBIS and EBIT. *J. Instrum.*, 5(10):C10004, 2010.

[13] S. Schwarz, G. Bollen, J.R. Crespo López-Urrutia, J. Dilling, M. Johnson, O. Kester, M. Kostin, F. Marti, C. Wilson, and P. Zavodszky. An electron beam ion trap for the NSCL reaccelerator. *Nucl. Instr. and Meth. B*, 266(19-20):4466, 2008.

[14] O. Kester. Charge breeding application of EBIS/T devices. *AIP Conf. Proc.*, 1099:7, 2009.

[15] W. Bleakney. A new method of positive ray analysis and its application to the measurement of ionization potentials in mercury vapor. *Phys. Rev.*, 34:157, 1929.

[16] P. A. Redhead and S. Feser. Multiple ionization of mercury by successive electron impacts. *Can. J. Phys.*, 46:1905, 1968.

[17] E. D. Donets and V. P. Ovsyannikov. Investigation of ionization of positive ions by electron impact. *Sov. Phys. JETP*, 53(3):466, 1981.

[18] R. W. Schmieder, C. L. Bisson, S. Haney, N. Toly, A. R. Van Hook, and J. Weeks. Sandia super-EBIS. *Rev Sci. Instrum.*, 61(1):259, 1990.

[19] M. A Levine, R E Marrs, J R Henderson, D A Knapp, and Marilyn B Schneider. The electron beam ion trap: A new instrument for atomic physics measurements. *Physica Scripta*, 1988(T22):157, 1988.

[20] R. Becker and O. Kester. Electron beam ion source and electron beam ion trap. *Rev. Sci. Instrum.*, 81:02A513, 2010.

[21] P. Beiersdorfer, A. L. Osterheld, V. Decaux, , and K. Widmann. Observation of lifetime-limited x-ray linewidths in cold highly charged ions. *Phys. Rev. Lett.*, 77:5353, 1996.

[22] J. D. Gillaspy. Overview of recent atomic spectroscopy at the NIST electron beam ion trap (EBIT) facility. *AIP Conf. Proc.*, 1438(1):97, 2012.

[23] José R. Crespo López-Urrutia. http://www.mpi-hd.mpg.de/ullrich/ebit/.

[24] G. Zschornack, St. Landgraf, F. Grossmann, U. Kentsch, V.P. Ovsyannikov, M. Schmidt, and F. Ullmann. Dresden EBIT: The next generation. *Nucl. Instrum. Meth. B*, 235(1-7):514, 2005.

[25] A.S. El-Said, R. Heller, and S. Facsko. Nanostructuring of BaF2 (1 1 1) surfaces by single slow highly charged ions. *Nucl. Instrum. Meth. B*, 269(9):901, 2011.

[26] S. Peggs M. Harrison and T. Roser. The RHIC accelerator. *Ann. Rev. Nucl. Part. Sci.*, 52:425, 2002.

[27] A. Pikin. RHIC EBIS: Basics of design and status of commissioning. *J. Instrum.*, 5(9):C09003, 2010.

[28] F. Wenander. Charge state breeders: On-line results. *Nucl. Instrum. Meth. B*, 266:4346, 2008.

[29] S. Schwarz, G. Bollen, M. Kostin, F. Marti, P. Zavodszky, J. R. Crespo López-Urrutia, J. Dilling, and O. Kester. A high-current electron beam ion trap as a charge breeder for the reacceleration of rare isotopes at the NSCL. *Rev. Sci. Instrum.*, 79(02A706), 2008.

[30] A. Lapierre, S. Schwarz, K. Kittimanapun, J. Fogleman, S. Krause, S. Nash, R. Rencsok, L. Tobos, G. Perdikakis, M. Portillo, J. A. Rodriguez, W. Wittmer, X. Wu, G. Bollen, D. Leitner, M. Syphers, and ReA team. The ReA electron-beam ion trap charge breeder for reacceleration of rare isotopes. *AIP Conf. Proc.*, 1525(1):497, 2013.

[31] C. Dickerson, B. Mustapha, A. Pikin, S. Kondrashev, P. Ostroumov, A. Levand, and R. Fischer. Simulation and design of an electron beam ion source charge breeder for the californium rare isotope breeder upgrade. *Phys. Rev. ST. - Accel. Beams*, 16:024201, 2013.

[32] S. Kondrashev, C. Dickerson, A. Levand, P. N. Ostroumov, R. C. Pardo, G. Savard, R. Vondrasek, J. Alessi, E. Beebe, A. Pikin, G. I. Kuznetsov, and M. A. Batazova. Development of electron beam ion source charge breeder for rare isotopes at californium rare isotope breeder upgrade. *Rev. Sci. Instrum.*, 83(2):02A902, 2012.

[33] A. Lapierre, M. Brodeur, T. Brunner, S. Ettenauer, A.T. Gallant, V. Simon, M. Good, M.W. Froese, J.R. Crespo Lpez-Urrutia, P. Delheij, S. Epp, R. Ringle, S. Schwarz, J. Ullrich, and J. Dilling. The TITAN EBIT charge breeder for mass measurements on highly charged short-lived isotopes-first online operation. *Nucl. Instrum. Meth. A*, 624(1):54, 2010.

[34] D. Rodríguez, K. Blaum, W. Nörtershäuser, M. Ahammed, A. Algora, G. Audi, J. Äystö, D. Beck, M. Bender, J. Billowes, M. Block, C. Bhm, G. Bollen, M. Brodeur, T. Brunner, B.A. Bushaw, R.B. Cakirli, P. Campbell, D. Cano-Ott, et al. MATS and LaSpec: High-precision experiments using ion traps and lasers at FAIR. *Eur. Phys. J. Special Topics*, 183(1):1, 2010.

[35] R. E. Marrs and D. R. Slaughter. A high intensity electron beam ion trap for charge state boosting of radioactive ion beams. *AIP Conf. Proc.*, 475(1):322, 1999.

[36] G. Herrmann. Optical theory of thermal velocity effects in cylindrical electron beams. *J. Applied Phys.*, 29:127, 1958.

[37] J. Gillaspy. *Trapping highly charged ions: fundamentals and applications.* NOVA Science Publisher Inc, 1999.

[38] G. Fußmann, C. Biedermann, and R. Radtke. EBIT:An electron beam ion source for the production and confinement of highly ionized atoms. *NATO ASI Series (proceedings summer school)*, page 429, 1998.

[39] R. Butt. *Introduction to Numerical Analysis Using MATLAB*, chapter 5. Jones and Bartlett Publishers, 2009.

[40] Y. S. Kim and R. H. Pratt. Direct radiative recombination of electrons with atomic ions:cross sections and rate coefficients. *Phys. Rev. A*, 27(6):2913, 1983.

[41] A. Müller and E. Salzborn. Scaling of cross sections for multiple electron transfer to highly charged ions colliding with atoms and molecules. *Phys. Lett. A*, 62:391, 1977.

[42] F. Wenander, B. Jonson, L. Liljeby, and G. H. Nyman. REXEBIS the electron beam ion source for the REX-ISOLDE project. *CERN-OPEN-2000-320.*

[43] W. Lotz. An empirical formula for the electron-impact ionization cross-section. *Z. Phys*, 206:205, 1967.

[44] R. Becker, O. Kester, and Th. Stoehlker. Simulation of charge breeding for trapped ions. *J. Phys.: Conf. Ser.*, 58:443, 2007.

[45] R. Becker, M. Kleinod, E. D. Donets, and A. I. Pikin. ACCU-EBIS: Collection and ionisation of reaction products. *in Proc. of EPAC92, Edition Frontiéeres*, page 981, 1992.

[46] A. T. Gallant, M. Brodeur, T. Brunner, S. Ettenauer, M. Good, A. Lapierre, R. Ringle, V. V. Simon, P. Delheij, and J. Dilling. TITAN-EBIT charge breeding of radioactive isotopes for high precision mass measurements. *J. Instrum.*, 5(08):C08009, 2010.

[47] O. Kester, G. Vorobjev, A. Sokolov, S. Geyer, F. Wenander, P. Delahaye, and R. Becker. Report on charge breeding investigations of task T-J03-1 and T-J03-3. *EURONS deliverables*, D-J03-1.1 and 1.3.

[48] S. Humphries. *Charged particle beams*, chapter 3. John Wiley and Sons, 1990.

[49] J. Buon. Beam phase space and emittance. Laboratoire d l'Accélérateur Linéaire, Orsay, France:89.

[50] M. P. Stockli. Measuring and analyzing the transverse emittance of charged particle beams. *AIP Conf. Proc.*, 868:25, 2006.

[51] M. W. Froese. The TITAN electron beam ion trap: Assembly, characterization, and first tests. Master thesis, University of Manitoba, Department of Physics and Astronomy, 2006.

[52] S. Schwarz, G. Bollen, O. Kester, K. Kittimanapun, A. Lapierre, J. R. Crespo Lpez-Urrutia, J. Dilling, F. Ames, L. E. Ahle, P. Beiersdorfer, R. E. Marrs, J. R. Beene, A. J. Mendez, D. W. Stracener, M. Lindroos, and F. Wenander. EBIS/T charge breeding for intense rare isotope beams at MSU. *J. Instrum.*, 5(10):C10002, 2010.

[53] G.K. Pang., G. Bollen, S. Chouhan, C. Guénaut, F. Marti, D.J. Morrissey, D. Lawton, J. Ottarson, S. Schwarz, and A.F. Zeller. The cyclotron gas stopper project at the NSCL. *Proceeding of PAC07, Albuquerque, New Mexico, USA*, (THPAS040):3588, 2007.

[54] F. Wenander. Charge breeding techniques. 746:40, 2004.

[55] Colutron Research Corporation. http://www.colutron.com. 2000.

[56] H. Zhang. *Ion sources*, section 2.3. Springer, 1999.

[57] M. Portillo, G. Bollen, S. Chouhan, O. Kester, G. Machicoane, J. Ottarson, S. Schwarz, and A. Zeller. An achromatic mass separator design for ions from the EBIT charge breeder at the NSCL. *Proceeding of PAC09, Vancouver, BC, Canada*, (FR5PFP015):4341, 2009.

[58] Keithley Instruments Inc. http://www.keithley.com/. 2013.

[59] Inc. Scientific Instrument Services. http://simion.com. 2003-2006.

[60] O. Kester, S. Schwarz, G. Bollen, M. Johnson, M. Kostin, M. Portillo, J. Ottarson, and C. Wilson. The EBIT charge state booster for exotic beam reacceleration at MSU. *Proceeding of PAC09, Vancouver, BC, Canada*, (MO6RFP034):429, 2009.

[61] E. Gavartin. Acceptance calculations for a charge breeder based on an electron beam ion trap. Master thesis, Michigan State University, Department of Physics and Astronomy, 2008.

[62] S. Schwarz. IonCool -A versatile code to characterize gas-filled ion bunchers and coolers (not only) for nuclear physics applications. *Nucl. Instrum. Meth. A*, 566(2):233, 2006.

[63] W. H.Press, S. A. Teukolsky, W. T. Vetterling, and B. P. Flannery. *Numerical Recipes in C: The Art of Scientific Computing*, chapter 16. Cambridge University Press, New York, NY, USA, 2 edition, 1992.

[64] A Lapierre, G Bollen, J R Crespo López-Urrutia, M Doleans, S Geyer, O Kester, K Kittimanapun, M Portillo, and S Schwarz. The MSU EBIT at NSCL. *J. Instrum.*, 5(07):c07001, 2010.

[65] K.T. McDonald and D.P. Russell. Methods of emittance measurement. In *Frontiers of Particle Beams; Observation, Diagnosis and Correction*, volume 343 of *Lecture Notes in Physics*, pages 122–132. Springer Berlin Heidelberg, 1989.

[66] R. E. Marrs. Self-cooling of highly charged ions during extraction from electron beam ion sources and traps. *Nucl. Instrum. Meth. B*, 149(1):182, 1999.

[67] Field Precision LLC. http://www.fieldp.com/. 1998-2013.